Fall 12-18-2015

Development of Manganese-Enhanced Magnetic Resonance Imaging (MEMRI) Methods to Study Pathophysiology Underlying Neurodegenerative Diseases in Murine Models

Aditya N. Bade
University of Nebraska Medical Center

Development of Manganese-Enhanced Magnetic Resonance Imaging

(MEMRI) Methods to Study Pathophysiology Underlying

Neurodegenerative Diseases in Murine Models

by

Aditya N. Bade

A DISSERTATION

Presented to the Faculty of

The Graduate College in the University of Nebraska

In Partial Fulfillment of the Requirements

For the Degree of Doctor of Philosophy

Pharmacology and Experimental Neuroscience

Under the Supervision of Professor Yutong Liu

University of Nebraska Medical Center

Omaha, Nebraska

December, 2014

TABLE OF CONTENTS

CHAPTER - 4: Generation of a MEMRI-based NOD/scid-IL-2Rγ_c^{null} Mouse Brain Atlas

LIST OF FIGURES

LIST OF TABLES

ACKNOWLEDGEMENTS

I like to start my acknowledgements by saying that I had best 5 years of my life during my Ph.D. training at UNMC, Omaha. I will treasure every moment I spent here and it was possible because of each and every person I came to know during last 5 years. It is hard to acknowledge every person in couple of pages and also, I am wordless to express my sincere gratitude towards them. Therefore, I like to thank god for bringing these people in my life.

First of all, I like to express my sincere and utmost gratitude to my parents (Navnath and Chandraprabha Bade), my brother and sister-in-law (Mahesh and Asha Bade), my nephew (Vedant), and my all family members for their support, encouragement and endless love. They have been great inspiration throughout my life. Without them, I wouldn't be who I am today.

Next to my parents, I would like to express my gratitude to my advisor Dr. Yutong Liu. I would like to thank him for giving me the opportunity to work in his laboratory. He always considered and valued my opinion, encouraging me to think and bring new research ideas to discuss with him. He was always available and easy to approach whenever I needed his help or advice. Being from non-radiology background, I needed lot of help and time to learn things related to MRI, but Dr. Liu was very patient, supportive and encourager during those times. Dr. Liu's qualities such as hard work, positive attitude, generosity and always smile on his face, influenced me most as a scientist. Dr. Liu has been a well-rounded advisor. I always received the best advice from him not only for research, but also for personal life and career. I am very thankful to

his support, encouragement, patience, availability, guidance, and appreciation throughout my training.

I am sincerely thankful to Dr. Howard E. Gendelman, who introduced me to Dr. Liu. Dr. Howard E. Gendelman played instrumental and significant role in influencing my research career. He has been a huge inspiration not only in my but also in many students personal as well as professional life. I feel very fortunate that I had opportunity to work in his laboratory. I am very thankful to his support, encouragement, availability, guidance and extensive training.

I would like extend my gratitude to the members of my advisory committee, which includes Dr. Michael D. Boska, Dr. Santhi Gorantla, Dr. Larisa Y. Poluektova and Dr. Shilpa Buch, for their valuable inputs, suggestion and constructive criticism during my graduate training. I especially like to thank Dr. Boska, Dr. Gorantla and Dr. Poluektova for their help, encouragement, support and guidance. I am also greatly appreciative to Dr. Gorantla for her support, encouragement, advice and lively valuable discussions about my research and career.

I would also like to thank my lab mates, who made me feel like home, helped me to learn different techniques, science, social behavior and many more things, and became my good friends. I shared many pleasant moments with these guys. For those reasons, I like to express my gratitude to current and previous lab members, including Dr. Prasanta Dash, Edward Makarov, Jaclyn Hollinger, Weizhe Li, Dr. Raghubendra Dagur, Dr. Divya Prakash Gnanadhas, Hang Su, Amanda Branch, Yan Cheng, Dr. Adrian Epstein, Dr. Tanuja Gutti, Dr. Zhang Gang, Sidra Akhter, Natasha Fields, Marnee Roundtree, Dr. Shantanu Balkundi, Dr. Pavan Puligijja, James Hilaire, and Brady Sillman.

I would like to thank bioimaging core facility and all the members associated with it, including Dr. Balasrinivasa R. Sajja, Dr. Mariano Uberti, Melissa Mellon, Ahmad Tanwir, Chris Woldstad, Dr. Dong J, Lirong Xu, and previous members, Biyun Zhou, Bruce Berrigan, for their the help, support, and friendship. I like to thank Dr. Uberti for his help with imaging softwares. I also like to extend my gratitude to Dr. Sajja for his valuable advice for research, lively discussions about career and all the coffees he bought for me during those discussions.

Many thanks to our department administrative staff, Leticia Tran, Theresa Grutel, Lana Reichardt, Robin Taylor, Kim Morrison, Julie Ditter, Johna Belling, Sandy Mahoney, Myhanh Che, Na Ly, and Reed Felderman for their enormous administrative help and support throughout my Ph.D. I would also like to thank to member of bioimaging core facility, Marie Witthoft, for her administrative help and support.

It will be incomplete without thanking my friends, who were there in my good and bad times. Without them, it would be hard to get through the graduate training, especially when my family is thousands of miles away. I will cherish every moment that I spent with them. I especially like to thank Dr. Swapnil Desale, Dr. Nilesh Wagh, Dr. Pavan Puligujja, Dr. Ariel Burns, Shrey Kanvinde, Prathamesh Patil, Vijay Yajjala, Vamsi Karuturi, and Shailendra Tallapaka. I also like to thank our daily lunch group, which made me laugh every day and forget about any stressful moment I had. I learned so many new things during our lunch conversations, not only about science but also about social/general life which helps me in day to day life. I had opportunity to serve in several student groups and committees, through these committees I was able to meet official people, make new friends and learn from their professional experience. I especially like

to thank UNMC Graduate Student Association and The International - Global Health Faculty and Student Advisory Committee.

Development of Manganese-Enhanced Magnetic Resonance Imaging (MEMRI) Methods to Study Pathophysiology Underlying Neurodegenerative Diseases in Murine Models

Aditya N. Bade, Ph.D.

University of Nebraska Medical Center, 2015

Supervisor: Yutong Liu, Ph.D.

Manganese-enhanced magnetic resonance imaging (MEMRI) opens the great opportunity to study complex paradigms of central nervous system (CNS) in freely behaving animals and reveals new pathophysiological information that might be otherwise difficult to gain. Due to advantageous chemical and biological properties of manganese (Mn^{2+}), MEMRI has been successfully applied in the studies of several neurological diseases using translational animal models to assess comprehensive information about neuronal activity, morphology, neuronal tracts, and rate of axonal transport. Although previous studies highlight the potential of MEMRI for brain imaging, the limitations concerning the use of Mn^{2+} in living animals and applications of MEMRI in neuroscience research are in their infancy. Therefore, development of MEMRI methods for experimental studies remains essential for diagnostic findings, development of therapeutic as well as pharmacological intervention strategies.

Our lab has been dedicating to develop novel MEMRI methods to study the pathophysiology underlying neurodegenerative diseases in murine models. In the first study, we investigated the cellular mechanism of MEMRI signal change during neuroinflammation in mice. The roles of neural cells (glia and neurons) in MEMRI signal enhancement were delineated, and ability of MEMRI to detect glial (astrocyte and

microglia) and neuronal activation was demonstrated in mice treated with inflammatory inducing agents. *In vitro* work demonstrated that cytokine-induced glial activation facilitates neuronal uptake of Mn^{2+}, and that glial Mn^{2+} content was not associated with glial activation. The *in vivo* work confirmed that MEMRI signal enhancement in the CNS is induced by astrocytic activation by stimulating neuronal Mn^{2+} uptake. In conclusion, our results supported the notion that MEMRI reflects neuronal excitotoxicity and impairment that can occur through a range of insults that include neuroinflammation.

In the second study, we evaluated the efficacy of MEMRI in diagnosing the complexities of neuropathology in an ananimal model of a neurodegenerative disease, neuroAIDS. This study demonstrated that MEMRI reflects brain region specific HIV-1-induced neuropathology in virus-infected NOD/scid-IL-2Rγc^{null} humanized mice. Altered MEMRI signal intensity was observed in affected brain regions. These included, but were not limited to, the hippocampus, amygdala, thalamus, globus pallidus, caudoputamen, substantia nigra and cerebellum. MEMRI signal was coordinated with levels of HIV-1 infection, neuroinflammation (astro- and micro- gliosis), and neuronal injury.

Following the application of MEMRI to assess HIV-1 induced neuropathology in immune deficient mice humanized with lymphoid progenitor cells, our successful collaboration with Dr. Sajja BR (Department of Radiology, UNMC, Omaha, NE) led to the generation of a MEMRI-based NOD/scid-IL-2R$_{\gamma c}$^{null} (NSG) mouse brain atlas. Mouse brain MRI atlases allow longitudinal quantitative analyses of neuroanatomical volumes and imaging metrics. As NSG mice allow human cell transplantation to study human disease, these animals are used to assess brain morphology. MEMRI provided sufficient contrast permitting 41 brain structures to be manually labeled on average brain of 19

mice using alignment algorithm. The developed atlas is now made available to researchers through Neuroimaging Informatics Tools and Resources Clearinghouse (NITRC) website (https://www.nitrc.org/projects/memribrainatlas/).

Finally, we evaluated the efficacy of N-acetylated-para-aminosalicylic acid (AcPAS) to accelerate Mn^{2+} elimination from rodent brain, enabling repeated use of MEMRI to follow the CNS longitudinally in weeks or months as well as inhibiting the confounding effects of residual Mn^{2+} from preceding administrations on imaging results. Two-week treatment with AcPAS (200 mg/kg/dose $\times$ 3 daily) accelerated the decline of Mn^{2+} induced enhancement in MRI. This study demonstrated that AcPAS could enhance MEMRI utility in evaluating brain biology in small animals.

LIST OF ABBREVIATIONS

MRI	Magnetic resonance imaging
MEMRI	Manganese-enhanced magnetic resonance imaging
Mn^{2+}	Manganese
Ca^{2+}	Calcium
Gd	Gadolinium
CNS	Central nervous system
MOBgl	Main olfactory bulb, glomerular layer
MOBgr	Main olfactory bulb, granule layer
AOB	Accessory olfactory bulb
AON	Anterior olfactory nucleus
PIR	Piriform area
DG-mo	Dentate gyrus_molecular layer
DG-(po+sg)	Dentate gyrus_(polymorph layer + granular layer)
CP	Caudoputamen
LSX	Lateral septal complex
STRv	Striatum ventral region
PALc	Pallidium, caudal region
GP	Globus pallidus
MS	Medial septal nucleus
AMY	Amygdala
cc	Corpus callosum
opt	Optic tract

ac	Anterior commissure
RFB	Rest of fiber tracts
TH	Thalamus
EPI	Epithalamus
HY	Hypothalamus
IC	Inferior colliculus
PAG	Periaqueductal gray
PRT	Pretectal region
SN	Substantia nigra
RMB	Rest of midbrain
P	Pons
MY	Medulla
CBXmo	Cerebellar cortex, molecular layer
CBXgr	Cerebellar cortex, granular layer
CBwm	Cerebellar white matter
FN	Fastigial nucleus
IP	Interpose nucleus
DN	Dentate nucleus
VL	Lateral ventricles
V3	Third ventricle
AQ	Cerebral aqueduct
V4	Fourth ventricle
HIP	Hippocampus

NITRC	Neuroimaging Informatics Tools and Resources Clearinghouse
LPS	Lipopolysaccharide
PBS	Phosphate-buffered saline
Dox	Doxycycline
IFN-γ	Interferon gamma
TNF-α	Tumor necrosis factor alpha
ICP/MS	Inductively coupled plasma mass spectrometry
GFAP	Glial fibrillary acidic protein
Iba-1	Ionized calcium binding adaptor molecule 1
DAB	3,3'-diaminbenzidine
SYN	Synaptophysin
MAP2	Microtubule-associated protein 2
NF	Neurofilament
DAPI	4,6-diamidino-2-phenylindole
HAND	HIV-1-associated neurocognitive disorders
ANI	Asymptomatic neurocognitive impairment
MND	Mild neurocognitive disorder
HAD	HIV-associated dementia
^{1}H MRS	Proton magnetic resonance spectroscopy
DTI	Diffusion tensor imaging
FACS	Fluorescence-activated cell sorting
VL	Viral load
T_1-wt	T_1-weighted

AcPAS   N-acetylated-para-aminosalicylic acid

PAS   Para-aminosalicylic acid

HPLC   High-performance liquid chromatography

CHAPTER – 1

Manganese (Mn^{2+}) -Enhanced Magnetic Resonance Imaging

(MEMRI)

1.1. Introduction

As being an excellent non-invasive tool with high spatial resolution and outstanding capacity for differentiating soft tissues to provide anatomical information of biological systems, magnetic resonance imaging (MRI) has become a pillar of radiological techniques in diagnostic imaging and has emerged as the major mode for assessing central nervous system (CNS) disorders [1]. MRI was introduced three decades ago into the clinical medicine [1]. Due to its properties, a variety of controls over image contrast, great flexibility and specificity in the detection of different pathophysiological mechanisms, metabolism assessment and anatomical as well as functional mapping, MRI has achieved widespread success not only in clinical, but also in research field [1-3]. Over the last 10 years, MRI utilization in experimental science has augmented [2][4,5]. Specially designed MRI units for experimental animals are now commercially available. Pictures of MRI units available for rodents at University of Nebraska Medical Center (UNMC) bio-imaging core facility are shown in figure 1.1. MRI acquisition softwares as well as post-processing tools are widely accessible [2]. Public and private financial sources have reinforced the expansion of MRI based brain atlases and databases [2].

In neuroscience research, innovations in diagnostic and therapeutic fields employing experimental animals rely on MRI. Availability of MRI in clinical as well as preclinical settings permits direct linking of findings between humans and experimental animals [3]. This non-invasive imaging tool has been used in the studies involving animal models of several neurological diseases, such as stroke, Parkinson's disease, Alzheimer's disease, and NeuroAIDS, epilepsy, brain tumors, multiple sclerosis, and other brain disorders [1-3,6-8].

Advances in MRI applications provide remarkable information about brain morphology, metabolism, physiology and function. The desire of obtaining more detailed information from brain, during normal and diseased conditions, with the help of MRI to improve our understanding is becoming more prominent. Thus, the interest in the use of contrast agents is increasing.

1.2. MRI contrast agents [1,9-13]

MRI uses hydrogen atoms of water molecules to generate images. The primary contrast in MRI image mainly results from regional differences in intrinsic factors, T_1 and T_2, spin-lattice and spin-spin, relaxation times. Proton density (PD), which is also termed as spin density (SD) is another factor affecting image contrast. These factors are independently chosen to generate the tissue image contrast. The differentiation between healthy and diseased tissue depends upon their distinctive signal intensity that relies on tissue PD, T_1 and T_2 relaxation times. However, the signal intensity generated by these intrinsic contrast factors of healthy and diseased tissue frequently too limited to enable sensitive and specific diagnosis. Intrinsic relaxation times of healthy and diseased tissues frequently overlap, leading to compromised detection of abnormal tissue or function. This limitation can be overcome by using MRI contrast agents.

Agents that affect the MRI signal contrast are paramagnetic (e.g. Mn^{2+}, Gd), and superparamagnetic (e.g. iron oxide particles, such as Fe_2O_3, Fe_3O_4) and ferromagnetic (e.g. albumin coated magnetite). These agents help to increase sensitivity and specificity of MRI signal acquisition and provide substantial diagnostic information by reducing T_1 and T_2 relaxation times of surrounding water protons in targeted tissue, leading to

generation of signal enhancement in shorter period of time and better signal-to-noise ratio.

In biomedical research, most widely used contrast agents are paramagnetic and superparamagnetic. Depending upon the characteristics, such as chemical composition, molecular size, *in vivo* distribution, pharmacokinetic properties, and individual's research question, agents are chosen for different studies. In our lab, we have used paramagnetic agent, Mn^{2+}, to study neurodegenerative diseases that are modeled using rodents, due to its advantageous chemical and biological properties.

1.3. Paramagnetic contrast agents

Lauterbur *et al.* first suggested the use of paramagnetic ions as contrast agent for MRI in 1978 [14]. Paramagnetic agents possess a permanent magnetic moment, which are randomly aligned in the absence of an externally applied magnetic field. When paramagnetic material senses externally applied magnetic field, the respective magnetic moments align parallel to the applied field. Furthermore, aligned magnetic moments generate a local magnetic field, leading to an effective reduction in T_1 (spin-lattice) and T_2 (spin-spin), relaxation times of surrounding water protons of the targeted organ systems. Reduction in the relaxation times results in MRI signal changes [1,9,10,12].

Paramagnetic property of the material is based on the presence of number of unpaired electrons in atom. Most known subgroups of paramagnetic compounds are metal ions (e.g. Mn^{2+}) and lanthanide elements (e.g. gadolinium (Gd)). The magnetic moment of unpaired electrons is greater than that of unpaired neutrons or protons. Therefore, agents with unpaired electrons are exclusively apt as MRI contrast agent

[9,10,12]. Even though, paramagnetic agents affect both T_1 and T_2 relaxation times, the shortening of T_1 mainly causes an increase in signal intensity. The result of increase in signal intensity remains until the concentration of agent is reached to optimal level. Thus, use of paramagnetic material as a MRI contrast agent is advantageous, as it exhibits greater effects on T_1 than on T_2 relaxation time.

1.4. Mn^{2+} – a paramagnetic contrast agent

Mn^{2+}, divalent ion, has paramagnetic properties. It has 5 unpaired electrons and causes strong reduction of both T_1 and T_2 relaxation times of surrounding water protons of targeted tissue [6,13,15,16]. The magnitude of T_1 or T_2 relaxation time reduction depends on the local Mn^{2+} concentration. It can be described by following equation [13]:

$$Ri_o = Rt(0) + Ri \, [Mn^{2+}]$$

Where,

$Ri_o = 1/Ti$ (i=1,2) is the observed relaxation rate

$[Mn^{2+}]$ = the concentration of the Mn^{2+} ion

Ri = the relaxivity constant, and

$Rt(0)$ = the relaxation rate of the solvent without manganese ($[Mn^{2+}] = 0$)

The use of Mn^{2+}, a divalent ion, and its unique properties as a MRI contrast agent is known as Mn^{2+}-enhanced magnetic resonance imaging (MEMRI).

1.5. MEMRI

The investigation of Mn^{2+} as contrast agent coincides with early days of nuclear magnetic resonance (NMR) [4,6,17]. Initial findings with the help of Mn^{2+} played important role in

understanding of water-exchange effects, which was a crucial step in the development of T_1 shortening contrast agents [4,6,18,19], and quantitative structural information of biological systems, which helped to develop techniques to confirm three-dimensional protein structure using NMR [4,20]. Mn^{2+} has been present since the beginning of MRI. Lauterbur *et al.* with the help of Mn^{2+} showed that relaxation times could affect signal intensity. Over 25 years ago, the use of Mn^{2+} as a MRI contrast agent was initialized. London *et al.* studied toxic effects of Mn^{2+} on anesthetized rats [21]. Since then, the use of MEMRI in experimental neuroscience for imaging the rodent brain has significantly evolved [4]. Our observation about MEMRI use in neuroscience research over the last 10 years is showed in figure 1.2.a and 1.2.b. Paramagnetic property of Mn^{2+} causes an effective reduction of the T_1 (spin-lattice) relaxation times of the surrounding water protons of the targeted organs, leading to signal enhancement. Positive contrast signal enhancement is detected on T_1-weighted images of tissues in which Mn^{2+} accumulates [4,6,9,12,15,16,22]. The difference between 3-D MRI image of brain of a mouse which was injected with $MnCl_2$ and 3-D MRI image of a brain of a mouse injected with saline showed in figure 1.3. Mn^{2+}-based contrast enhancement and neuroarchitecture details are clearly visible in these mice. Yet, one major weakness of Mn^{2+} is associated cellular toxicity upon overexposure [4-6,12,15,16,23]. However, Mn^{2+} is considered as least toxic among the essential trace elements. This divalent ion is also an essential trace element, as the lack of it leads to severe disorders in humans [5,6,16,24].

Interpretation of MEMRI findings requires profound knowledge of Mn^{2+} behavior in biological systems under healthy and diseased conditions as well as of experimental considerations. Therefore, following sections will introduce the properties of Mn^{2+} and its

entrance in the CNS, main applications of MEMRI in biological systems, methodological considerations of Mn^{2+} administration in animals, Mn^{2+} toxicity, MEMRI in humans, and objective and related study aims of my Ph.D. thesis.

1.6. Properties of Mn^{2+} in the CNS

Mn^{2+} is recognized by biological systems as a chemical analogue of calcium (Ca^{2+}), same charge and similar ionic radii (Mn^{2+} = 89 pm and Ca^{2+} = 114 pm) [6]. Therefore, Mn^{2+} can enter into the neurons and other excitable cells through voltage-gated calcium channels (L-type voltage-gated Ca^{2+} channels), NMDA receptors, Na^{2+}/ Ca^{2+} exchanger, and Na^{2+}/ Mg^{2+} antiporter [4-6,12,15,25-30]. Once inside the cells, it binds with high affinity to proteins and nucleic acids. Inside the neuronal cells, Mn^{2+} accumulates in the endoplasmic reticulum (ER), is packaged into the vesicles and is transported along the axons anterogradely [5,6,25,27,31]. Upon reaching the pre-synaptic membranes it is released at the synaptic cleft and taken up by the adjacent neurons [4-6,15,25,27]. Scheme of Mn^{2+} transport mechanism between neurons in CNS is depicted in figure 1.4.

Systemic administration of Mn^{2+} leads to its accumulation in all tissues, significantly detected in liver, kidney, heart and brain [6,16,32,33]. As major route of entry for Mn^{2+} into the CNS is through CSF-Blood barrier, the time course, uptake and distribution of Mn^{2+} varies across the brain regions [6,15,16]. Initial Mn^{2+} accumulation occurs in the brain regions near to ventricles and then gets distributed throughout the entire brain. Contrast enhancement in CNS reaches to its equilibrium 24 hours after $MnCl_2$ administration (Figure 1.5) [6,15,16,32,34,35]. It has been shown that Mn^{2+} has very slow clearance rate from the brain. It can take up to 300 days to clear from the brain

tissue [16]. Mn^{2+} has long half-life in the brain, 51–74 days in rodents [16,36] and more than 100 days [6,37] in monkeys, whereas short half-life in visceral organs like liver and heart, which might indicate that Mn^{2+} is carrier-transported into the brain, but not out of it [6,16,36]. Efflux of Mn^{2+} from brain is not well studied but is believed that the efflux mechanism is diffusion mediated [6,38].

1.7. Entry of Mn^{2+} into the CNS

Mn^{2+} enters into the brain via the following three major routes [4-6,12,15,16].

After systemic administration of $MnCl_2$, Mn^{2+} enters the brain through two different routes as follows:

    1) Through choroid plexus via CSF (major and rapid entry route)

    2) Through BBB by diffusion or active transport processes (minor entry route)

At physiological plasma Mn^{2+} concentration, it is mainly transported across the endothelial cells of brain capillaries, and after bolus systemic injection of Mn^{2+} (at high concentration), the major route of entry is via choroid plexus.

    Application of Mn^{2+} via the olfactory system provides the easiest route for Mn^{2+} entrance into the brain, as olfactory tract is not protected by the BBB or other barriers. It has been shown in rodents that upon exposure to air containing Mn^{2+}, it is able to enter into the olfactory bulb via the olfactory epithelium.

    3) Through olfactory nerve via olfactory epithelium

1.8. Mn^{2+} - an intracellular contrast agent

Two essential factors have been derived from the results obtained with the help of Mn^{2+} [16,22].

1) Signal received after $MnCl_2$ administration comes from the intracellular Mn^{2+}, whereas another popular paramagnetic MRI contrast agent, chelated gadolinium, remains extracellular. Therefore, MEMRI has been useful to map signal intensities according to cellular density of the targeted tissue, and thus to visualize brain cytoarchitecture.

2) Rate of Mn^{2+} uptake is useful to detect normal and affected tissue functions. Normal uptake defines the normal function of the tissue. Therefore, disruption of Mn^{2+} uptake serves as a biomarker to detect the pathological conditions such as stroke, neuroAIDS, epilepsy, etc.

1.9. Applications of MEMRI in experimental neuroscience

Depending upon above mentioned properties of Mn^{2+}, literature has divided the applications of MEMRI as a research tool in three major groups [5,6,15,16,22]. But, here, I have divided the applications in four major groups.

1) Measurement of neuronal activity (functional assessment); this application of MEMRI is termed as activation-induced MEMRI (AIM-MRI) [29]; figure 1.6

2) Assessment of anatomical/morphological details [6]; figure 1.3

3) Assessment of neuronal tracts and assessment of axonal connectivities [6]; figure 1.7

4) Assessment of rate of axonal transport [5]

Taking advantage of these applications, researchers have been using MEMRI in neurosciences to address problems using translational models of brain diseases.

1.10. Methodological considerations for Mn^{2+} administration

1.10.1 Preparation of $MnCl_2$ solution:

The most common and easy way to deliver Mn^{2+} to the experimental animals is through the injection of $MnCl_2$ solution [6,15,16]. After administration, $MnCl_2$ dissociates into Mn^{2+} and Cl^-. The salt material ($MnCl_2$) is commercially available in three different grades in major biochemical companies, for example:

1) $MnCl_2$, powder form, anhydrous, purified (> 99%), molecular weight (M.W.)- 125.84 g/mol (Sigma-Aldrich, St Louis, MO)

2) $MnCl_2 \cdot 4H_2O$, flake form, hydrous, highly purified (99.99%), M.W.- 197.91 g/mol (Sigma-Aldrich, St Louis, MO)

3) $MnCl_2$ solution, prepared in 18 megohm water, 1.00 ± 0.001 M (Sigma-Aldrich, St Louis, MO)

All three forms are suitable for experimental purpose. We have used $MnCl_2 \cdot 4H_2O$ for all the studies carried out in our laboratory and for studies mentioned in my dissertation.

Chemical and physical properties, especially osmolarity and pH, of the $MnCl_2$ solution to be used for experimental purpose need to be considered for successful application [6,15,16]. Osmolarity of body fluid is around 300 mOsm/l. One has to make sure that administered amount of $MnCl_2$ will not affect the natural osmolarity by using the isotonic solution of $MnCl_2$, 100 mM. Solutions with significant lower osmolarity (<100mM) are hypotonic, and solutions with significant higher osmorality (>100 mM)

are hypertonic. This parameter has strong impact when $MnCl_2$ solution is injected directly into the brain tissue (stereotaxic injection), but has very minor consequences when injected systemically, including intravenous (IV), intraperitoneal (IP), subcutaneous (SC). For all of our studies, $MnCl_2$ has been administered systemically, especially through intraperitoneal route [25,39,40]. Therefore, we have been successfully using the $MnCl_2$ solution with lower concentration (50 mM).

Another important property to consider while preparing the $MnCl_2$ solution is pH. It is essential to adjust the pH of the solution at 7.4 for effective application. The procedure used to prepare $MnCl_2$ solution for our studies is described in materials and methods section of respective chapters.

1.10.2. Administration of Mn^{2+}

Due to acute and chronic cellular toxicity of Mn^{2+}, one has to take into consideration of experimental methodology, including delivery route, appropriate dose, osmolarity as well as pH of $MnCl_2$ solution to deliver adequate amount of Mn^{2+} to the site of interest in a time efficient manner to receive desired contrast signal while avoiding any toxic effects of Mn^{2+} to experimental animals and its interference with normal physiological properties.

It has been showed that systemic administration of $MnCl_2$ solution in a fractionated manner (i.e. smaller doses, multiple injections) is beneficial to reach sufficient Mn^{2+} accumulation into tissues (especially brain) to obtain high contrast signal while minimizing toxic side effects [23,41]. We used fractionated administration scheme

for all of our studies [25,39,40]. Below, I have summarized commonly used administration routes for $MnCl_2$ solution in the literature.

In order to increase the efficiency of MEMRI, the delivery route is chosen based on the application [4,5,13,15,16]. MEMRI applications are described under the heading applications of MEMRI in experimental neuroscience in the current chapter. In general, $MnCl_2$ can be injected intraperitoneally (IP), intravenously (IV), subcutaneously (SC), intracranially (stereotaxic injection) into the area of interest, and can be delivered by using commercially available osmotic pumps. Among systemic administration routes (IP, SC, IV), there is no strong evidence suggesting that one route is better than others or that one route causes lesser toxicity compared to others.

Kuo *et al.* measured relative T_1 relaxation times in mice (C57Bl/6) brains with different modes of systemic administration (IP, IV, SC). Authors concluded that all the systemic routes of administration showed significant reduction in T_1 values following $MnCl_2$ infusion and both the temporal and regional changes in cerebral T_1 relaxation times are relatively independent of the route of administration [42].

Few studies have used osmotic pumps to deliver Mn^{2+} into the experimental animals [13,43,44]. Osmotic pumps deliver a specific concentration of Mn^{2+} over a specified period of time. It has been proposed that slow release of Mn^{2+} can decrease associated toxicity issues. Currently, ALZET® osmotic pumps company (Durect Corporation, CA) sales pumps in the market. Company describes that ALZET pumps operate on osmotic pressure difference between the tissue environment (in which the pump is implanted) and a compartment within the pump. When water enters into the pump compartment from the surrounding tissue, it compresses the flexible reservoir,

leading to displace $MnCl_2$ solution from the reservoir at a controlled rate to the surrounding body environment of the animal. ALZET provides a variety of delivery rates, SC or IP.

1.11. Mn^{2+} - a trace element and related toxicity

Mn^{2+} is an essential heavy metal for cellular processes and normal development. It plays essential role in the regulation of metabolism, cell energy, immune response, blood sugar homeostasis, blood clotting, reproduction, digestion, skeletal system development, bone growth as well as in synaptic function as an antioxidant and enzymatic cofactor in the brain [5,6,45,46]. It serves as a significant co-factor for enzymes such as glutamine synthetase, pyruvate carboxylase, arginase, phosphoenolpyruvate carboxykinase and mitochondrial superoxide dismutase [5,6,46,47]. In humans, deficiencies in Mn^{2+} are associated with skin lesions, epileptic seizures, bone malformation, increased Ca^{2+} and phosphorous levels, among others [5,16]. Mn^{2+} is generally excreted through the hepatobiliary route [6,47,48]. However, in excess, Mn^{2+} is toxic [4-6,15,16,47]. Acute overexposure to this ion happens when administered systemically to patients, leading to cardiac toxicity, renal failure, liver toxicity, and may be death [6,16]. Moreover, chronic exposure to Mn^{2+} is neurotoxic, a brain disorder characterized by neurological and psychological disorders, a progressive neurodegenerative disorder, called as 'Manganism', accompanied by loss of Dopaminergic neurons [5,16]. In this disorder, Mn^{2+} is highly concentrated in basal ganglia. Symptoms of manganism are similar to symptoms of Parkinson's disease, such as tremors, widespread rigidity, hallucination, bradykinesia, sleep disorder, lack of facial expressions, slurred speech and memory loss

[15,49]. It was observed that excessive exposure of this heavy metal damages the CNS by a number of mechanisms, including inhibition of mitochondrial oxidative phosphorylation, which leads to reduced ATP [49,50], impaired astrocyte-neuronal interactions, indirect effect on excitatory and inhibitory influences [47]. Aberrant Mn^{2+} accumulation in brain has also been linked to Huntington's disease and other neurological disorders [49]. Normal human brain Mn^{2+} concentration is at 5.32-14.03 ng Mn^{2+}/mg protein, which is equivalent to 20-52.8 µM Mn^{2+} (around 1.1-2.9 ppm). General toxic responses occur when Mn^{2+} concentration is elevated to around 3 fold (i.e. 15.96-42.09 ng Mn^{2+}/mg protein or 60.1-158.4 µM Mn^{2+}) [49].

The most common method to administer Mn^{2+} to experimental animals is through the injection of $MnCl_2$ solution. Detailed information about $MnCl_2$ solution and administration routes are discussed under the heading preparation of $MnCl_2$ solution and administration on Mn^{2+} in the current chapter. This paragraph discusses toxicity related to $MnCl_2$. According to the Material Safety Data Sheet (MSDS) [16], $MnCl_2$ is a harmful chemical agent, which causes eye and skin irritation upon contact. Target organs include the CNS and the lungs. As per the MSMDS report, following characteristic signs and symptoms of exposure have been identified: 'Men exposed to manganese dusts showed a decrease in fertility. Chronic exposure primarily affects CNS, and early symptoms are languor, sleepiness and weakness in the legs.' In more advanced cases, emotional disturbances such as uncontrollable laughter and a spastic gait with tendency to fall while walking. Mn^{2+} is also known to be a potential mutagen, and pneumonia is highly observed in the workers exposed to dust of Mn^{2+} compounds. Therefore, one must wear appropriate barriers and take proper precautions while interacting with $MnCl_2$ material

for experimental purposes. LD_{50} toxicity data reports in the MSDS for $MnCl_2$ are shown in Table 1 [16].

Indeed, acute and chronic cellular toxicity of Mn^{2+} repressed its transformation as clinical MRI contrast agent. Regardless of these toxicity issues, to take the advantage of chemical and biological properties of Mn^{2+} as a contrast agent, researchers generated alternative ways to avoid toxicity of Mn^{2+} while delivering sufficient amount of Mn^{2+} to the site of interest in an efficient manner in experimental animals.

For all of our studies, level of Mn^{2+} used is below the neurotoxic levels. Animals were observed daily after each i.p. $MnCl_2$ injection and 24 hours after the injection to detect Mn^{2+} toxicity. If tremor or convulsion (signs of Mn^{2+} overdose) persisted longer than 3 minutes or lethargy (decreased locomotion), and loss in body weight was observed at 24 hours, mice were euthanized [25]. Moreover, it is demonstrated that concentration of $Mn^{2+} > 200$ µM can affect the neuronal activity [51]. We measured the R_1 values to determine absolute Mn^{2+} concentration before and after Mn^{2+} administration in cortex region of mice (n=11). There was ~ Δ 0.15 alteration in R_1 values after Mn^{2+} administration. R_1 values were less than 0.70 after Mn^{2+} administration (Figure 1.8). These R_1 values then were compared with previously reported correlation between R_1 values and relative Mn^{2+} concentration. This comparison corresponded to less than 40 µM Mn^{2+} in the brain parenchyma region of experimental animal used in our studies (Figure 1.8). Thus, with the help of behavioral observation and measured R_1 values, we confirmed that our fractionated administration scheme for $MnCl_2$ is non-toxic to animals and injected Mn^{2+} does not have effect on neuronal activity.

1.12. MEMRI in Humans

Even though the use of Mn^{2+} as a MRI contrast agent in clinical settings has been restricted due to cellular toxicity, properties of Mn^{2+} such as high sensitivity and specificity, and its prominent results in rodent, song birds, and monkeys, encouraged researchers to develop chelates of Mn^{2+} for the clinical use. Several chelates were developed and few of them were introduced into the market by biochemical companies. Manganese dipyridoxaldiphosphate (MnDPDP) was the first Mn^{2+}-based contrast agent approved by FDA. This product was approved for the liver imaging [5,6,9,16,52,53]. Product containing Manganese dipyridoxaldiphosphate (MnDPDP) was introduced into the market by GE healthcare called Teslascan®. MnDPDP is anionic chelate and dissociates quickly after administration to yield free Mn^{2+} ions. Although MnDPDP was mainly considered for liver imaging, some studies demonstrated its usefulness in imaging of pancreas and biliary tract [9]. Another pharma-company, Eagle Vision Pharmaceutical, is testing contrast agent called SeeMore® for cardiac imaging [5]. This product consists free Mn^{2+} ions formulated along with Ca^{2+} ions to outweigh the transient effect of Mn^{2+} as a Ca^{2+} inhibitor. This agent is currently used in dogs and pigs for cardiac and vascular imaging. Few promising chelating agents were invented for clinical use, however, further research needed for successful translation of MEMRI.

MEMRI has been successfully used in previous studies to study brain disorders in experimental animals. Although previous studies highlight the potential of MEMRI for brain imaging, the limitations and boundaries concerning the use of Mn^{2+} in living animals and development of new MEMRI applications in neuroscience are at the beginning level. Therefore, during the course of my Ph.D, we have determined the

cellular source for altered signal intensity during pathological conditions, evaluated the efficacy of chemical compound for washing out the Mn^{2+} from the rodent brain for longitudinal studies, and developed tools such as 3-D mouse brain atlas, which is now available for public use at NIRTC resources.

1.13. Objective and aims of the thesis

1.13.1. Objective

To develop manganese-enhanced magnetic resonance imaging (MEMRI) methods to study pathophysiology underlying neurodegenerative diseases in murine models.

1.13.2. Aims

1) Investigate role of glia and neurons in manganese-enhanced magnetic resonance imaging (MEMRI) signal enhancement during inflammation (Chapter 2).

2) Evaluate the application of MEMRI in diagnosing the brain pathology in animal models of neurodegenerative diseases (Chapter 3).

3) Generate MEMRI-based NOD/scid-IL-2R$_{\gamma c}^{null}$ mouse brain atlas (Chapter 4).

4) Evaluate the efficacy of N-acetylated-para-aminosalicylic acid (AcPAS) to accelerate Mn^{2+} elimination from rodent brain (Chapter 5).
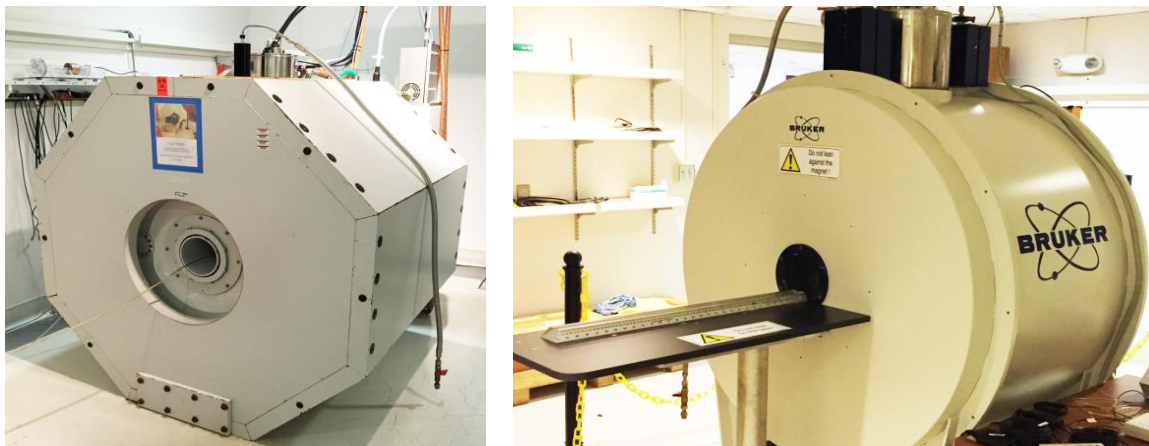
Figure 1.1. MRI units for small animals at UNMC bio-imaging core facility. Both scanners are 7 Tesla/21 cm, Bruker Biospin (Bruker, Billerica, MA)

(a)

(b)
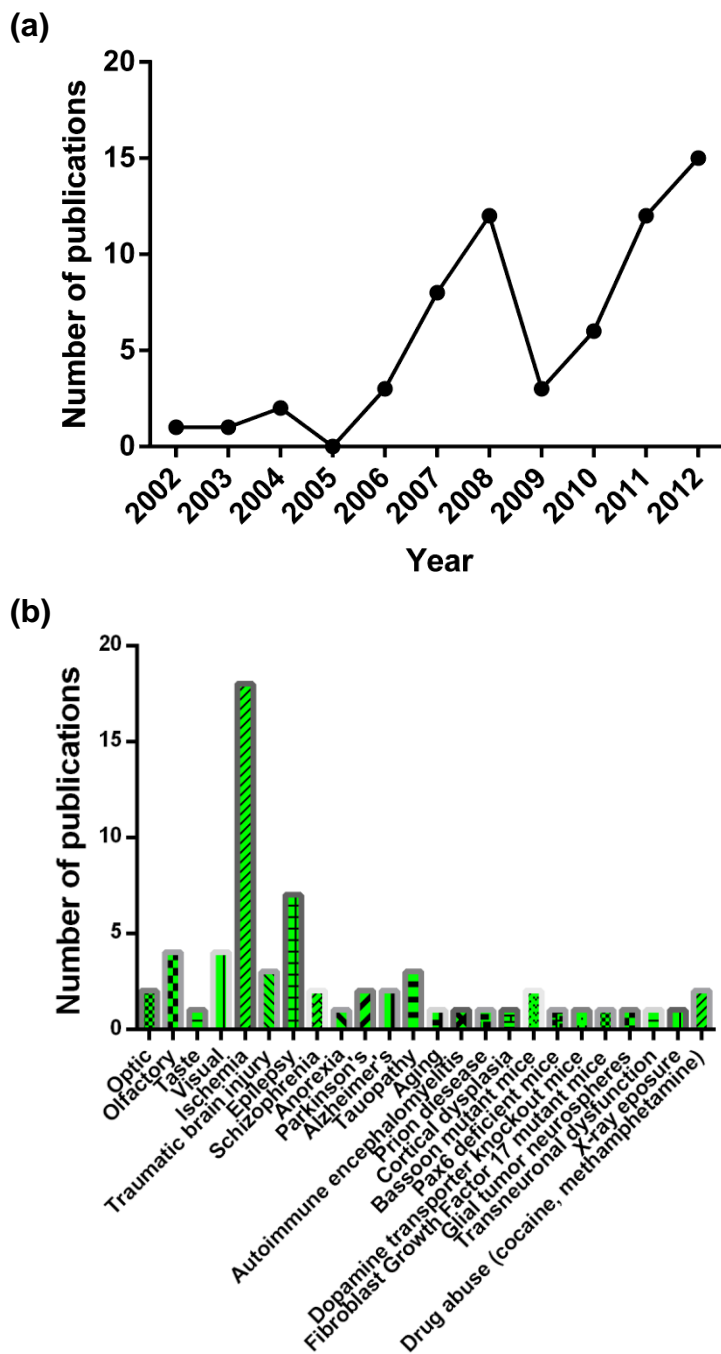
Figure 1.2. MEMRI in experimental neuroscience. Distribution of MEMRI publications

in **(a)** years and **(b)** neuroscience-related topics
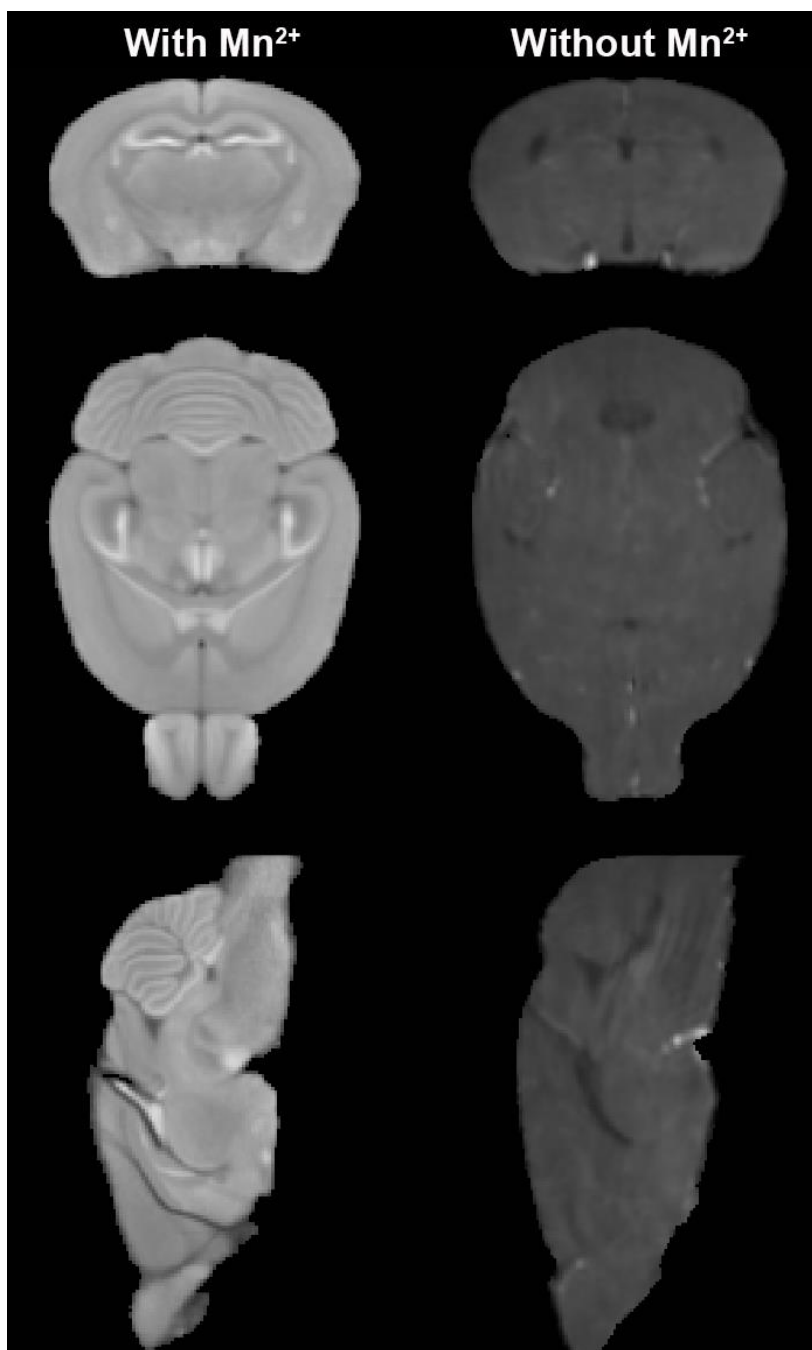
Figure 1.3. Three-dimensional MRI image of mouse brain with and without Mn^{2+}.
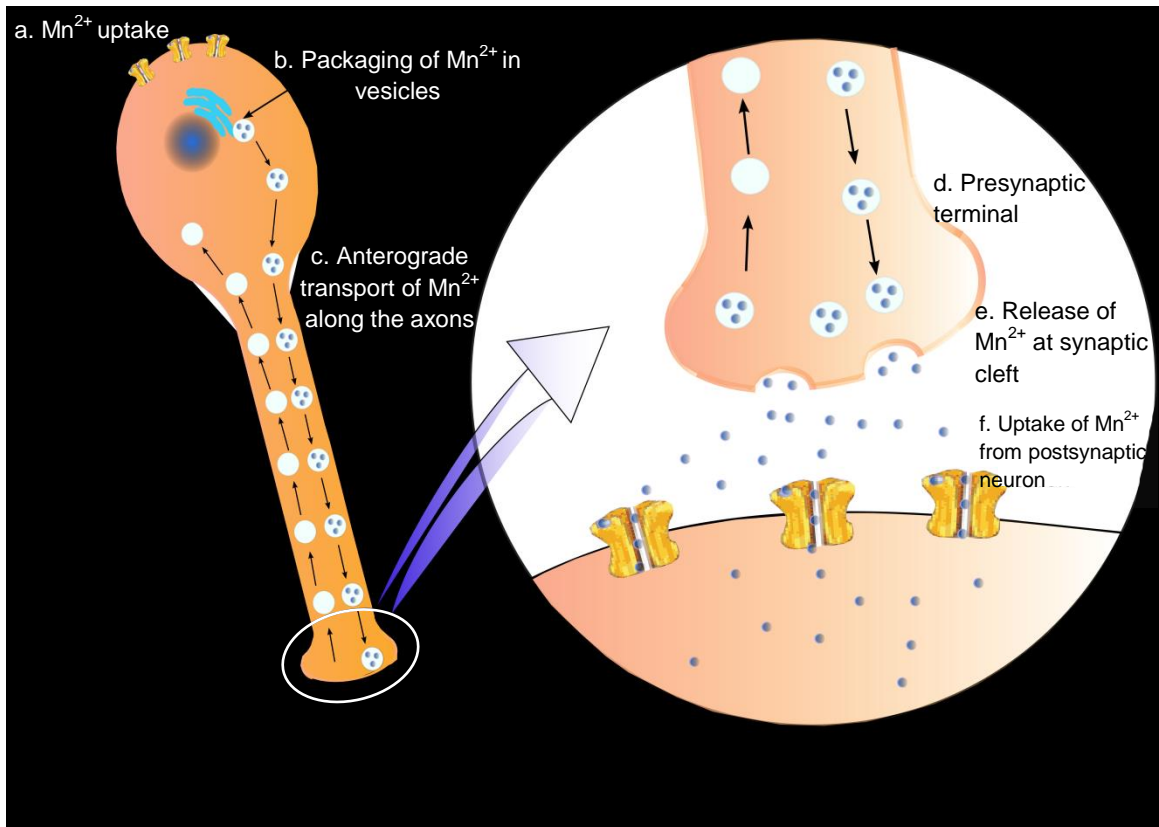
Figure 1.4. Scheme of Mn^{2+} transport mechanism in CNS. **(a)** Once Mn^{2+} entered the CNS, it enters the neurons through voltage gated Ca^{2+} channels. **(b)** Inside neurons, ions are accumulated in the endoplasmic reticulum and packaged into vesicles. **(c)** Mn^{2+} ions are further transported anterogradely along the axons with the help of microtubule assembly. **(d and e)** Upon reaching to the presynaptic terminal, Mn^{2+} ions get released at the synaptic cleft **(f)** and taken up by the adjacent neuron. Figure is modified from [12]
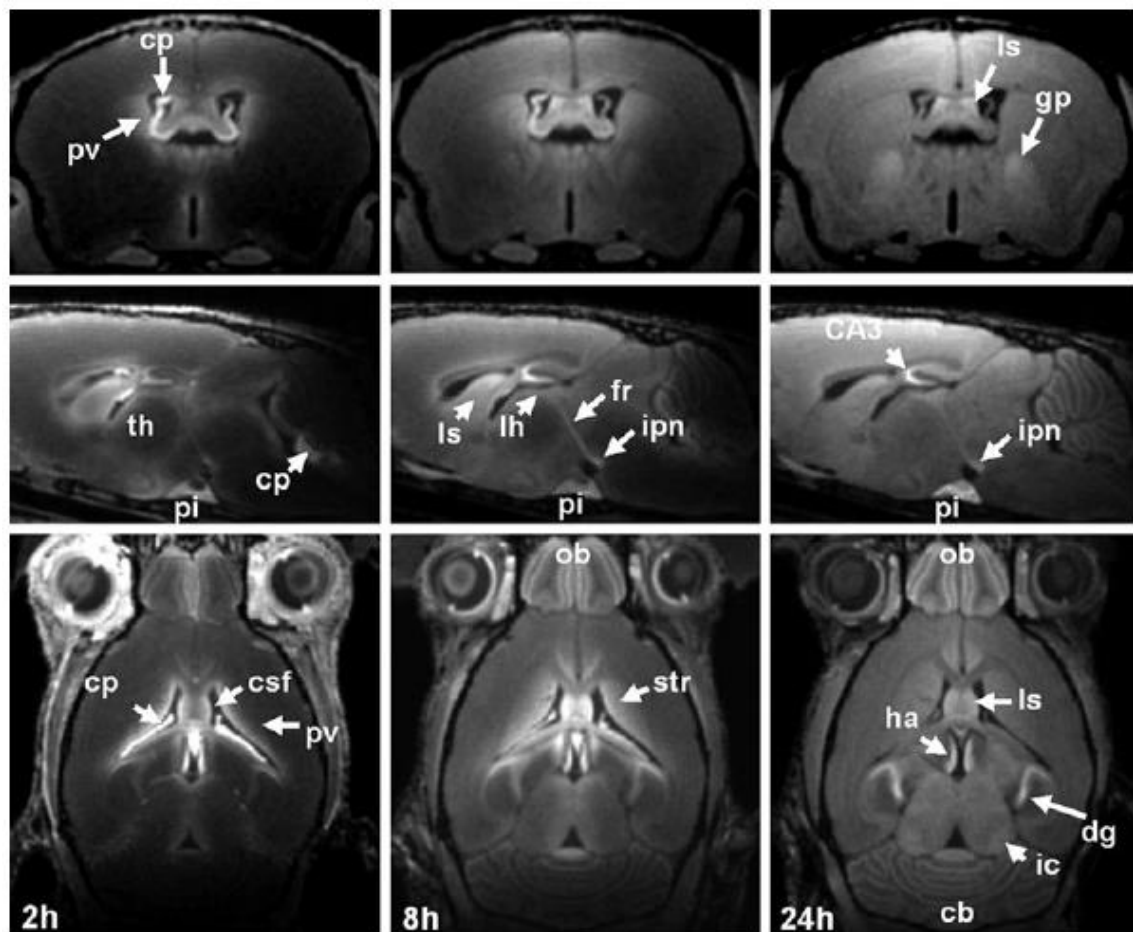
Figure 1.5. Temporal Mn^{2+} distribution across the brain. (Top) Coronal, (middle) sagittal and (bottom) axial MEMRI sections of a mouse brain *in vivo* 2, 8, and 24 h after intraperitoneal injection of 320 μmol/kg MnCl$_2$ (9.4 T, 100 μm isotropic resolution). Cb, cerebellum; cp, choroid plexus; CSF, cerebrospinal fluid; dg, dental gyrus; fr, fasciculus retroflexus; gp, globus pallidus; ha, habenula; ic, inferior colliculus; ipn, interpeduncular nucleus; lh, lateral habenula; ls, lateral septum; ob, olfactory bulb; pi, pituitary gland; pv, periventricular tissue; str, striatum; th, thalamus. Figure is adapted from [6]
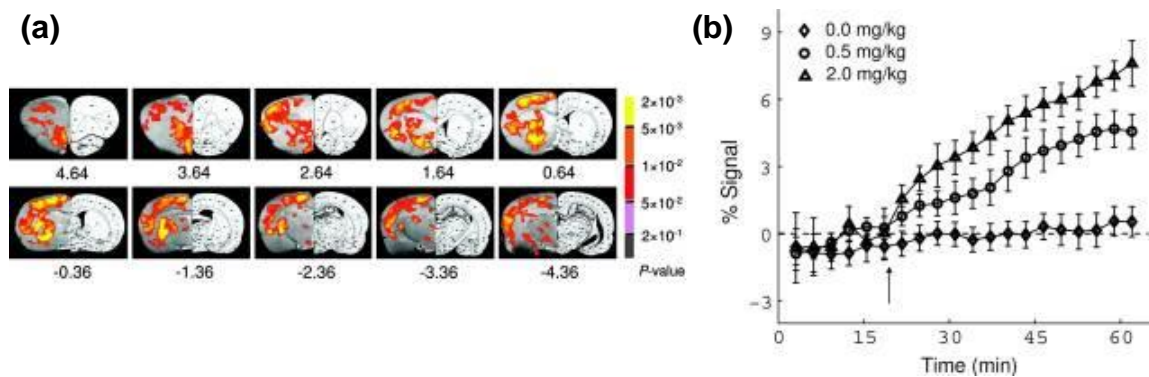
Figure 1.6. MEMRI measures neuronal activity. (a) MEMRI of acute cocaine-induced brain activation. Activation maps are superimposed onto T_2-weighted MRI with corresponding rat brain atlas sections shown on the right. Activated voxels are clustered in the hemisphere with the BBB disrupted by hyperosmolar mannitol. The contralateral hemisphere had an intact BBB and did not show activation. Activated structures include olfactory cortex; medial, ventral, and lateral orbital cortex; pre-limbic cortex; cingulate cortex; nucleus accumbens (NAc), caudate putamen; ventral pallidus; external globus pallidus; agranular insular cortex; thalamus; hypothalamus; retrosplenial dysgranular cortex; hippocampus; and primary and secondary somatosensory and motor cortex. (b) Averaged MEMRI response time course in the NAc from animals receiving saline (n = 6) and 0.5 mg/kg (n = 5) and 2.0 mg/kg (n = 6) cocaine. All time courses were normalized to the baseline signal after bolus injection of mannitol, but before the injection of cocaine or saline. Figure is adapted from [29]
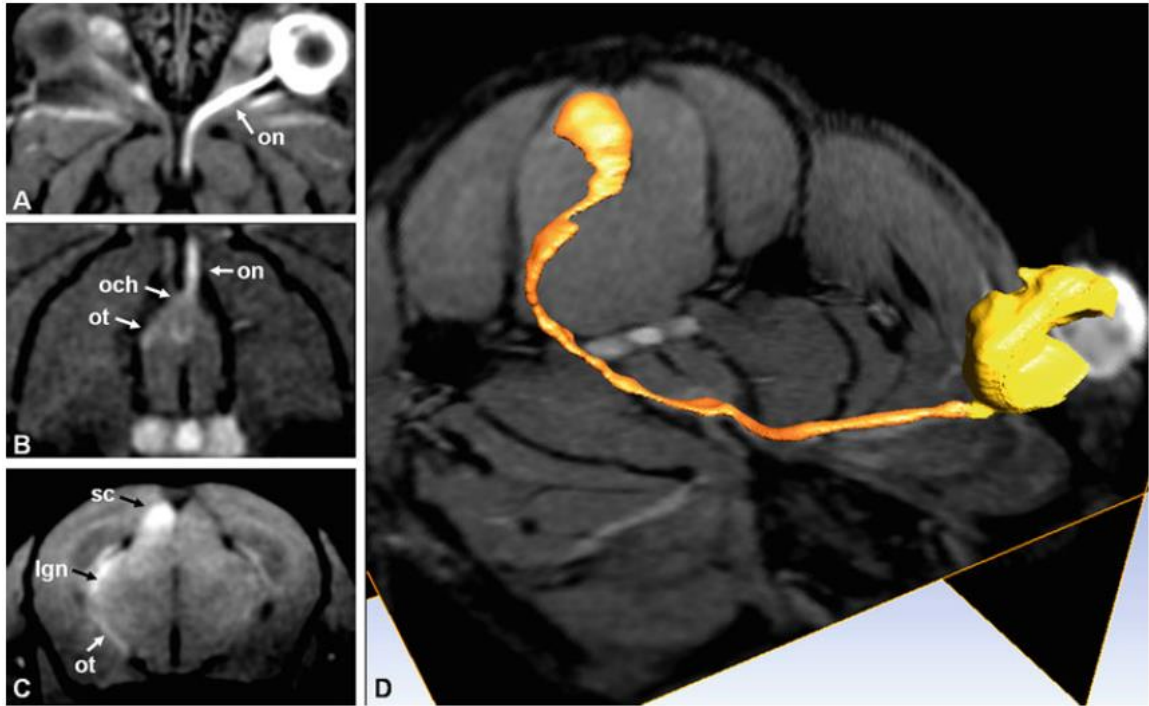
Figure 1.7. MEMRI detects neuronal tracts. (**a**, **b**) Horizontal and (**c**) axial MEMRI sections and (**d**) 3D volume rendering of a mouse optical system in vivo 24 h after intravitrial administration of 0.06 μmol MnCl2 (2.35 T, 117 μm isotropic resolution). lgn, lateral geniculate nucleus; och, optic chiasm; on, optic nerve; ot, optic tract; sc, superior colliculus. Figure is adapted from [6]
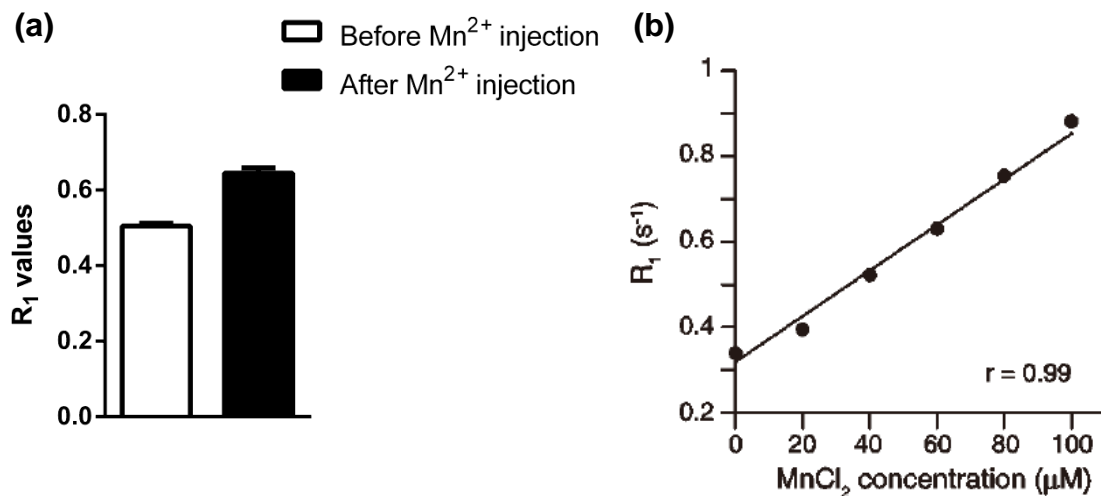
Figure 1.8. Measurement of R_1 values. **(a)** R_1 (1/T_1) values were measured in mice brain cortex before and after Mn^{2+} injections. Mice were injected with our lab optimized fractionated $MnCl_2$ injections. (n=11). **(b)** R_1 values plotted against $MnCl_2$ concentration, significant linear correlation was observed between the two (*n* = 4 MRI acquisitions, *P* < 0.0001, *r*: Pearson's correlation coefficient). Panel b of the figure is adapted from [51]

Table 1.1. LD$_{50}$ (toxicity) data for MnCl$_2$.

Species	Route	Dose	Remarks
Rat	Oral	250 mg/kg	
	Intraperitoneal	147 mg/kg	Behavioral: somnolence (general depressed activity)
			Behavioral: convulsions or effect on seizure threshold
	Intravenous	92.6 mg/kg	Behavioral: somnolence (general depressed activity)
			Behavioral: convulsions or effect on seizure threshold
	Intramuscular	700 mg/kg	
Mouse	Oral	1031 mg/kg	Behavioral: tremor
			Behavioral: convulsions or effect on seizure threshold
			Lungs, thorax or respiration: other changes
	Intraperitoneal	121 mg/kg	
	Intravenous	38 mg/kg	Behavioral: somnolence (general depressed activity)
			Behavioral: ataxia
			Lungs, thorax or respiration: respiratory stimulation
	Intramuscular	255 mg/kg	
Dog	Intravenous	202 mg/kg	
Guinea pig	Oral	916 mg/kg	Behavioral: tremor
			Behavioral: convulsions or effect on seizure threshold
			Lungs, thorax or respiration: other changes

Source: MSDS for MnCl$_2$ (product number 244589, Sigma-Adrich, St Louis, MO, USA).

Table is adapted from [16].

1.14. References

1. Bruggen N. V. and Roberts T. (2003) Biomedical Imaging in Experimental Neuroscience, CRC Press.

2. Liu Y. (2014) Magnetic Resonance Imaging, in Current Laboratory Methods in Neuroscience Research, Xiong H. and Gendelman H. E. eds., Springer,.

3. Dijkhuizen R. M. and Nicolay K., (2003) Magnetic resonance imaging in experimental models of brain disorders. J. Cereb. Blood Flow Metab. 23, 1383-1402.

4. Malheiros J. M., Paiva F. F., Longo B. M., Hamani C. and Covolan L., (2015) Manganese-Enhanced MRI: Biological Applications in Neuroscience. Front. Neurol. 6, 161.

5. Inoue T., Majid T. and Pautler R. G., (2011) Manganese enhanced MRI (MEMRI): neurophysiological applications. Rev. Neurosci. 22, 675-694.

6. Boretius S. and Frahm J. (2011) Manganese-Enhanced Magnetic Resonance Imaging, in *In Vivo* NMR Imaging, Schröder L. and Faber C. eds., Springer, pp. 531-568.

7. Benveniste H. and Blackband S. J., (2006) Translational neuroscience and magnetic-resonance microscopy. Lancet Neurol. 5, 536-544.

8. Benveniste H. and Blackband S., (2002) MR microscopy and high resolution small animal MRI: applications in neuroscience research. Prog. Neurobiol. 67, 393-420.

9. Curvosemedo L. and Caseiroalves F. (2011) MRI Contrast Agents, in Clinical MRI of the Abdomen, Springer, pp. 17-39.

10. Strijkers G. J., Mulder W. J., van Tilborg G. A. and Nicolay K., (2007) MRI contrast agents: current status and future perspectives. Anticancer Agents Med. Chem. 7, 291-305.

11. Berry E. and Bulpitt A. Fundamentals of MRI, CRC Press.

12. Grunecker B., (2011) Manganese-enhanced MRI as an *in vivo* functional imaging tool in mice.

13. McCREARY J. K., (2010) Applications Of Manganese-Enhanced Magnetic Resonance Imaging In Neuroscience   .

14. Lauterbur P. C., Mendonca-Dias M. H. and Rudin A. M. (1978) Augmentation of Tissue Water Proton Spin-Lattice Relaxation Rates by In Vivo Addition of Paramagnetic Ions., in Frontiers of Biological Energetics pp. 752–759.

15. Silva A. C. and Bock N. A., (2008) Manganese-enhanced MRI: an exceptional tool in translational neuroimaging. Schizophr. Bull. 34, 595-604.

16. Silva A. C., Lee J. H., Aoki I. and Koretsky A. P., (2004) Manganese-enhanced magnetic resonance imaging (MEMRI): methodological and practical considerations. NMR Biomed. 17, 532-543.

17. Connick R. E. and Poulson R. E., (1959) Effect of paramagnetic ions on the nuclear magnetic resonance of O-17 in water and the rate of elimination of water molecules from the 1st coordination sphere of cations. J Chem Phys.

18. Sherry A. D. and Wu Y., (2013) The importance of water exchange rates in the design of responsive agents for MRI. Curr. Opin. Chem. Biol. 17, 167-174.

19. Siriwardena-Mahanama B. N. and Allen M. J., (2013) Strategies for optimizing water-exchange rates of lanthanide-based contrast agents for magnetic resonance imaging. Molecules. 18, 9352-9381.

20. Wuthrich K., (2003) NMR studies of structure and function of biological macromolecules (Nobel Lecture). J. Biomol. NMR. 27, 13-39.

21. London R. E., Toney G., Gabel S. A. and Funk A., (1989) Magnetic resonance imaging studies of the brains of anesthetized rats treated with manganese chloride. Brain Res. Bull. 23, 229-235.

22. Silva A. C., (2012) Using manganese-enhanced MRI to understand BOLD. Neuroimage. 62, 1009-1013.

23. Grunecker B., Kaltwasser S. F., Peterse Y., Samann P. G., Schmidt M. V., Wotjak C. T. and Czisch M., (2010) Fractionated manganese injections: effects on MRI contrast enhancement and physiological measures in C57BL/6 mice. NMR Biomed. 23, 913-921.

24. Rucker D., Thadhani R. and Tonelli M., (2010) Trace element status in hemodialysis patients. Semin. Dial. 23, 389-395.

25. Bade A. N., Gorantla S., Dash P. K., Makarov E., Sajja B. R., Poluektova L. Y., Luo J., Gendelman H. E., Boska M. D. and Liu Y., (2015) Manganese-Enhanced Magnetic Resonance Imaging Reflects Brain Pathology During Progressive HIV-1 Infection of Humanized Mice. Mol. Neurobiol.

26. Itoh K., Sakata M., Watanabe M., Aikawa Y. and Fujii H., (2008) The entry of manganese ions into the brain is accelerated by the activation of N-methyl-D-aspartate receptors. Neuroscience. 154, 732-740.

27. Pautler R. G. and Koretsky A. P., (2002) Tracing odor-induced activation in the olfactory bulbs of mice using manganese-enhanced magnetic resonance imaging. Neuroimage. 16, 441-448.

28. Hsu Y. H., Lee W. T. and Chang C., (2007) Multiparametric MRI evaluation of kainic acid-induced neuronal activation in rat hippocampus. Brain. 130, 3124-3134.

29. Lu H., Xi Z. X., Gitajn L., Rea W., Yang Y. and Stein E. A., (2007) Cocaine-induced brain activation detected by dynamic manganese-enhanced magnetic resonance imaging (MEMRI). Proc. Natl. Acad. Sci. U. S. A. 104, 2489-2494.

30. Medina D. C., Kirkland D. M., Tavazoie M. F., Springer C. S.,Jr and Anderson S. E., (2007) Na+/Ca2+-exchanger-mediated Mn2+-enhanced (1)H2O MRI in hypoxic, perfused rat myocardium. Contrast Media Mol. Imaging. 2, 248-257.

31. Pautler R. G., Silva A. C. and Koretsky A. P., (1998) In vivo neuronal tract tracing using manganese-enhanced magnetic resonance imaging. Magn. Reson. Med. 40, 740-748.

32. Takeda A., Sawashita J. and Okada S., (1998) Manganese concentration in rat brain: manganese transport from the peripheral tissues. Neurosci. Lett. 242, 45-48.

33. Spiller M., Brown R. D.,3rd, Koenig S. H. and Wolf G. L., (1988) Longitudinal proton relaxation rates in rabbit tissues after intravenous injection of free and chelated Mn^{2+}. Magn. Reson. Med. 8, 293-313.

34. Bock N. A., Paiva F. F., Nascimento G. C., Newman J. D. and Silva A. C., (2008) Cerebrospinal fluid to brain transport of manganese in a non-human primate revealed by MRI. Brain Res. 1198, 160-170.

35. Aoki I., Wu Y. J., Silva A. C., Lynch R. M. and Koretsky A. P., (2004) In vivo detection of neuroarchitecture in the rodent brain using manganese-enhanced MRI. Neuroimage. 22, 1046-1059.

36. Takeda A., Sawashita J. and Okada S., (1995) Biological half-lives of zinc and manganese in rat brain. Brain Res. 695, 53-58.

37. Crossgrove J. and Zheng W., (2004) Manganese toxicity upon overexposure. NMR Biomed. 17, 544-553.

38. Yokel R. A., Crossgrove J. S. and Bukaveckas B. L., (2003) Manganese distribution across the blood-brain barrier. II. Manganese efflux from the brain does not appear to be carrier mediated. Neurotoxicology. 24, 15-22.

39. Bade A. N., Zhou B., Epstein A. A., Gorantla S., Poluektova L. Y., Luo J., Gendelman H. E., Boska M. D. and Liu Y., (2013) Improved visualization of neuronal injury following glial activation by manganese enhanced MRI. J. Neuroimmune Pharmacol. 8, 1027-1036.

40. Bade A. N., Zhou B., McMillan J., Narayanasamy P., Veerubhotla R., Gendelman H. E., Boska M. D. and Liu Y., (2015) Potential of N-acetylated-para-aminosalicylic acid to accelerate manganese enhancement decline for long-term MEMRI in rodent brain. J. Neurosci. Methods. 251, 92-98.

41. Bock N. A., Paiva F. F. and Silva A. C., (2008) Fractionated manganese-enhanced MRI. NMR Biomed. 21, 473-478.

42. Kuo Y. T., Herlihy A. H., So P. W., Bhakoo K. K. and Bell J. D., (2005) In vivo measurements of T1 relaxation times in mouse brain associated with different modes of systemic administration of manganese chloride. J. Magn. Reson. Imaging. 21, 334-339.

43. Canals S., Beyerlein M., Keller A. L., Murayama Y. and Logothetis N. K., (2008) Magnetic resonance imaging of cortical connectivity in vivo. Neuroimage. 40, 458-472.

44. Eschenko O., Canals S., Simanova I., Beyerlein M., Murayama Y. and Logothetis N. K., (2010) Mapping of functional brain activity in freely behaving rats during voluntary

running using manganese-enhanced MRI: implication for longitudinal studies. Neuroimage. 49, 2544-2555.

45. Aschner J. L. and Aschner M., (2005) Nutritional aspects of manganese homeostasis. Mol. Aspects Med. 26, 353-362.

46. Massaad C. A. and Pautler R. G., (2011) Manganese-enhanced magnetic resonance imaging (MEMRI). Methods Mol. Biol. 711, 145-174.

47. Hazell A. S., (2002) Astrocytes and manganese neurotoxicity. Neurochem. Int. 41, 271-277.

48. Papavasiliou P. S., Miller S. T. and Cotzias G. C., (1966) Role of liver in regulating distribution and excretion of manganese. Am. J. Physiol. 211, 211-216.

49. Bowman A. B. and Aschner M., (2014) Considerations on manganese (Mn) treatments for in vitro studies. Neurotoxicology. 41, 141-142.

50. Chen J. Y., Tsao G. C., Zhao Q. and Zheng W., (2001) Differential cytotoxicity of Mn(II) and Mn(III): special reference to mitochondrial [Fe-S] containing enzymes. Toxicol. Appl. Pharmacol. 175, 160-168.

51. Kikuta S., Nakamura Y., Yamamura Y., Tamura A., Homma N., Yanagawa Y., Tamura H., Kasahara J. and Osanai M., (2015) Quantitative activation-induced manganese-enhanced MRI reveals severity of Parkinson's disease in mice. Sci. Rep. 5, 12800.

52. Diehl S. J., Lehmann K. J., Gaa J., McGill S., Hoffmann V. and Georgi M., (1999) MR imaging of pancreatic lesions. Comparison of manganese-DPDP and gadolinium chelate. Invest. Radiol. 34, 589-595.

53. Wang C., (1998) Mangafodipir trisodium (MnDPDP)-enhanced magnetic resonance imaging of the liver and pancreas. Acta Radiol. Suppl. 415, 1-31.

CHAPTER - 2

Role of Glia and Neurons in Manganese-Enhanced Magnetic Resonance Imaging (MEMRI) Signal Enhancement During Inflammation

2.1. Introduction

Manganese (Mn^{2+}) is a potent magnetic resonance imaging (MRI) contrast agent used to improve anatomical visibility, most notably, neural structures. Unlike other agents, such as gadolinium, iron oxide, iron platinum and protein-based compounds, Mn^{2+} remains at a very early stage in clinical development, based in large measure to its inherent neurotoxicity [1-3]. Nonetheless, a number of recent reports demonstrate that Mn^{2+}-enhanced MRI (MEMRI) in normal animal brains provide novel information relevant to anatomical, integrative, and functional assessments of neuronal connectivity. These findings are linked to the abilities of Mn^{2+} ions to efficiently enter neurons through voltage-gated calcium channels [4-7].

A major drawback for the use of Mn^{2+} as a contrast agent in studies of human disease models rests in understanding its cellular mechanism and profiles [8,9]. Despite such potential limitations, significant attempts have been made, in recent years, to use MEMRI in studies of the pathobiology of neurodegenerative diseases utilizing relevant animal models [9-25]. Nonetheless and paramount to the successful application of MEMRI is not simply the ability to deliver Mn^{2+} to the site of interest or of disease but in determining the cell types and cellular mechanisms that engage the ion and produce the signal enhancement observed. Based on our long standing interest in the links between neuroimmunity and neurodegenerative diseases we reasoned that pathological activation of the immune-competent glial cells could represent an obligatory event for any MEMRI signal enhancements. In support of this idea is a wealth of prior studies demonstrating that MEMRI signal enhancements were co-localized with reactive glia [14,22,26,27].

However, it was never clear if such signal enhancements resulted from Mn^{2+} accumulation in the glial cells directly, or from elevated manganese uptake by neuronal cells stimulated by glial reaction.

Thus, we sought to better elucidate the cellular basis of MEMRI signal in studies of neurodegenerative diseases. We reasoned that if the cell association of the signal enhancement is determined, MEMRI can be developed as a potential imaging tool to monitor real-time glial-neuronal interactions. To this end, we investigated relationships between microglial and astrocytic activation linked to Mn^{2+} uptake. These studies were both *in vitro* as performed in glial and neuronal cells and *in vivo* using MRI following lipopolysaccharide (LPS) treatments in mice. The results showed that astrocytic reactions result in MEMRI signal enhancement by stimulating neuronal Mn^{2+} ion uptake.

2.2. Materials and Methods

2.2.1. PC-12 Differentiation

A rat adrenal pheochromocytoma-derived cell line - PC-12 Tet-Off, was used to study neuronal Mn^{2+} uptake. PC-12 cells were utilized here because they serve as a relevant *in vitro* model system for primary neuronal cells [28,29]. They have been widely used to study voltage-gated Ca^{2+} channels [30,31] and effects of Mn^{2+} exposure on these cells [2,32,33]. Following withdrawal of doxycycline (Dox) from the medium, PC-12 cells were differentiated with nerve growth factor (NGF, R&D Systems 1156-NG/CF).

2.2.3. Cell Co-culture and Activation
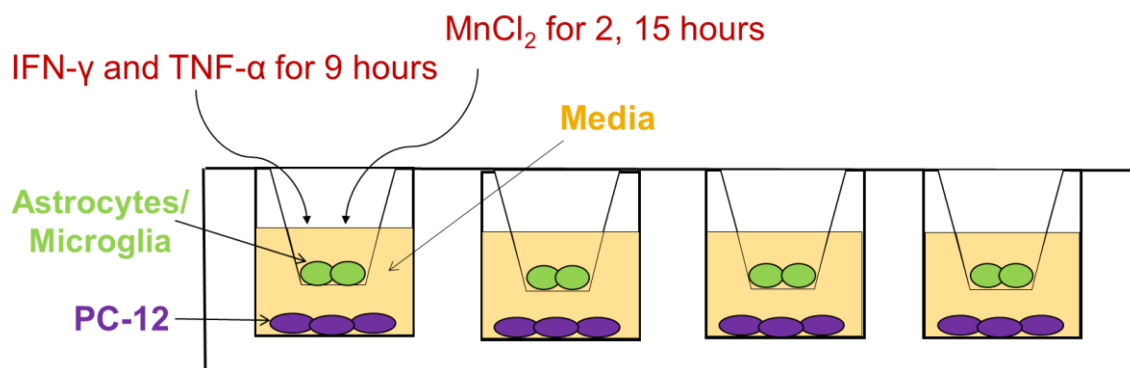
Figure 2.1. PC-12 cells (differentiated to neurons) were co-cultured with primary astrocytes or microglia respectively at the cell ratio of 1:1 (10^5 cells).

Primary cultured mouse astrocytes and microglia were prepared from *NOD-scid IL2R$_g^{null}$ (NSG)* newborn pups as described in [34,35]. Differentiated PC-12 cells were de-attached and seeded in multi-well plates. Primary astrocytes and microglia were placed on inserts and co-cultured with PC-12 cells respectively at the cell ratio of 1:1 (10^5 cells, Fig. 2.1). The co-cultured cells were then treated with a combination of cytokines including interferon gamma (IFN-γ) and tumor necrosis factor alpha (TNF-α) at the following concentrations: 25 (IFN-γ) and 2.5 (TNF-α), 50 and 5.0, or 100 and 10.0 ng/ml to induce glial activation. After nine hours of treatment, MnCl$_2$ solution was administered in the medium at concentrations of 80, 160 and 320 µM. An untreated cell group was used for control measurements. Cells were washed and resuspended at 2 and 15 hours after MnCl$_2$ treatment. Inductively coupled plasma mass spectrometry (ICP/MS) was used to measure the Mn^{2+} concentration. Experiments were performed with triplicate samples.

2.2.4. Mouse Model of Acute Neuroinflammation

All animal procedures performed in this study were approved by the University of Nebraska Medical Center Institutional Animal Care and Use Committee. LPS was intracranially (i.c.) injected to induce focal inflammation in male wild-type *C57BL/6* mice (n = 13, 6-8 weeks old). Using a stereotactic injection device, 10 μg (LPS) in 2 μl PBS was administrated into the left hemispheric caudoputamen (coordinates from bregma: 3.0 mm lateral, 0.5 mm anterior, and −3.5 mm ventral). The LPS solution was delivered with a 27 g needle at the flow rate of 0.2 μl per minute. A sham-operated control group (n = 11) was injected with 2 μl PBS through the i.c. route with the same parameters as the LPS group.

2.2.5. MEMRI

$MnCl_2$ (50 mM) was administrated i.p. with the dose of 60 mg/kg consecutively four times at 24 hour intervals before MRI. Another group of mice (n = 10) with i.c. LPS injection was added to study the effect of LPS alone on MRI signal enhancement. This group was administrated with saline through the i.p. route with the volume of 6 ml/kg at the same times as the $MnCl_2$ injection. The LPS mice injected with $MnCl_2$ are designated as LPS + $MnCl_2$ hereafter, and the LPS mice injected with saline are designated as LPS + saline. The sham-operated mice with i.c. PBS injection are designated as PBS + $MnCl_2$. One day after LPS or PBS injection, six LPS + $MnCl_2$ mice, five LPS + saline mice and five PBS + $MnCl_2$ mice were scanned using MRI. The remaining mice were scanned seven days after LPS or PBS injection. After MRI, the mice were euthanized and brains were removed for histology.

MRI was performed 24 hours after the last $MnCl_2$ injection on a 7T/21 cm horizontal bore scanner (Bruker, Billerica, MA) operating ParaVision 5.1 with a volume coil for RF transmission and a 4-channel phased-array coil for signal reception. Mice were scanned using T_1 mapping (fast spin echo with variable TR from 0.4 s to 10 s, 12 slices, slice thickness = 0.5 mm, in-plane resolution = 0.1x0.1 mm^2) and T_1-wt MRI (gradient recalled echo, TR = 20 ms, flip angle = 20°, 3D isotropic resolution = 0.1 x 0.1 x 0.1 mm^3).

To reduce the influence of the inhomogeneous signal reception by the surface coil, N3 field inhomogeneity correction [36] was first performed on each image using MIPAV (CIT, NIH). The brain was then manually aligned to the LONI atlas (LONI, UCLA) in Analyze (AnalyzeDirect, KS). The alignment is necessary for accurate quantification of signal enhancement due to manganese uptake.

MRI signal enhancement was measured on a slice-by-slice basis in the axial direction. On each slice, the injection site was first identified. The mean value and standard deviation (SD) of the signal intensity about the corresponding location of the needle hole on the contralateral hemisphere was measured (in a larger ROI), then the intensity threshold was defined as the mean value plus 2 SDs. This threshold was applied on the ipsilateral hemisphere as the lower boundary to identify enhanced area about the needle hole. The enhanced volume was the summation of the enhanced areas multiplied by the slice thickness. The total enhanced volume was then normalized to the needle depth. The signal enhancement ratio was calculated by dividing the mean signal intensity in the enhanced volume by mean intensity on the contralateral side.

2.2.6. Immunohistology

Mice were euthanized immediately after MRI. Brains were collected and fixed in 4% paraformaldehyde overnight and embedded in paraffin. The paraffin blocks were cut into 5 μm thick sections. These brain tissue sections were then labeled with rabbit polyclonal antibodies for glial fibrillary acidic protein (GFAP) (1:1000, Dako, Carpinteria, CA). Microglia were stained with rabbit polyclonal antibodies for ionized calcium binding adaptor molecule 1 (Iba-1) (1:500; Wako Chemicals, Richmond, VA). The polymer-based HRP-conjugated anti-mouse and anti-rabbit Dako EnVision systems were used as secondary detection reagents and 3,3'-diaminbenzidine (DAB, Dako) used as a chromogen. All paraffin-embedded sections were counterstained with Mayer's hematoxylin. Images were captured with a 10x objective using Nuance EX multispectral imaging system fixed to a Nikon Eclipse E800 (Nikon Instruments, Melville, NY), and image analysis software (Caliper Life sciences, Inc., a Perkin Elmer Company, Hopkinton, MA) was used for quantification of GFAP and Iba-1 expression in the region of interest (in and around the injection line) as reflected by intensity/μm^2. Area-weighted average intensity was calculated for GFAP and Iba-1 expression by dividing the total signal intensity, for each partitioned area, by area (μm^2).

For immunofluorescence labeling, brain sections about the injection line were treated with the paired combination of primary antibodies mouse anti-synaptophysin (SYN) (1:1000, EMD Millipore), and rabbit anti-microtubule-associated protein 2 (MAP2) (1:750, EMD Millipore). Primary antibodies were labeled with secondary anti-mouse and anti-rabbit antibodies conjugated to the fluorescent probes Alexa Fluor 488 and Alexa Fluor 594, and nuclei were labeled with DAPI (4,6-diamidino-2-

phenylindole). Slides were coverslipped with ProLong Gold anti-fade reagent (Invitrogen, Carlsbad, CA). Then slides were stored at −20°C after drying for 24 hours at room temperature. Images were captured at wavelengths encompassing the emission spectra of the probes, with a 10X objective by Nuance EX multispectral imaging system fixed to a Nikon Eclipse E800 (Nikon Instruments, Melville, NY), and image analysis software (Caliper Life sciences, Inc., a Perkin Elmer Company, Hopkinton, MA) used for quantification. For SYN and MAP2 expression, area-weighted average fluorescence intensity was calculated in the region of interest (in and around the injection line) by dividing the total signal intensity, for each partitioned area, by area (μm^2) as intensity/μm^2.

2.2.7. Statistical Analysis

T-test was used to compare the cell manganese concentrations in the *in vitro* study. Correlation between manganese uptake by PC-12/glial cells and cytokine level were performed using Pearson's correlation coefficient calculation. In the *in vivo* MEMRI study, t-test was used to compare all the variables in between LPS and PBS injected groups, whereas Pearson's correlation coefficient was used to test for correlations between signal enhancement and glial reactivity.

2.3. Results

2.3.1. Mn^{2+} Uptake by PC-12 Cells

The manganese concentration in PC-12 cells co-cultured with astrocytes and microglia was shown in Fig. 2.2.a and 2.2.b, respectively. Mn^{2+} concentration in PC-12 cells was plotted against cytokine level (IFN-γ/TNF-α, ng/ml) at 2 and 15 hours of $MnCl_2$

incubation time (left and right plots, respectively). In this figure, several properties of the baseline manganese uptake by PC-12 cells (when IFN-γ/TNF-α = 0/0) are manifest. First of all, the measurements at $MnCl_2$ concentration = 0 shown in Fig. 2.2 by dash-dot lines demonstrated that PC-12 cells endogenous manganese was low, suggesting the manganese in PC-12 must be taken from the extrinsic source – the $MnCl_2$ solution. Secondly, the manganese uptake by PC-12 cells depends on the availability of the extrinsic manganese (i.e., the concentration of $MnCl_2$ solution). It can be seen that the PC-12 manganese concentration is positively correlated with $MnCl_2$ concentration in all the plots in Fig. 2.2 (Pearson's correlation, $r \geq 0.900$, $p < 0.05$). The incubation time of $MnCl_2$ apparently plays a role in PC-12 manganese uptake as well. The manganese concentration in PC-12 cells at 15 hours was much higher than at 2 hours, evidenced by comparing the left and right columns in Fig. 2.2 ($p < 0.05$ at $MnCl_2$ = 160 and 320 μM). These observations were in agreement with previous findings [3].

The role of glial reaction on PC-12 manganese uptake involves a number of factors including the glial cell type, and the level and time of glial reaction. Fig. 2.2.a illustrates that the change in PC-12 manganese uptake resulted from astrocytic activation. At short inflammatory cytokine treatment time (2 hours), PC-12 manganese uptake was almost linearly increased with cytokine levels at 160 μM (Pearson's correlation, $r = 0.990$, $p < 0.01$) and 320 μM (Pearson's correlation, $r = 0.998$, $p < 0.01$). Prolonged treatment (15 hours) seemed to suppress the manganese uptake by PC-12 cells with cytokine levels at 160 and 320 μM $MnCl_2$. However the negative correlation between the manganese concentration and cytokine level was not significant ($p = 0.064$ at 160 μM, $p = 0.052$ at 320 μM).

On the other hand, microglial reaction had no significant impact on PC-12 manganese uptake. At the high $MnCl_2$ concentration (320 µM) and short treatment time (2 hours), it showed the trend of negative impact (Pearson's correlation, r = -0.935, p = 0.065). The PC-12 manganese uptake remained constant at all other $MnCl_2$ concentrations at both 2 and 15 hours.

It was interesting to see that at 15 hours Mn^{2+} uptake by PC-12 cells co-cultured with astrocytes at baseline (IFN-γ/TNF-α = 0/0) was twice the concentration of Mn^{2+} as PC-12 cells co-cultured with microglia. This result could be due to increase in Mn^{2+} efflux from astrocytes in response to high extracellular Mn^{2+} [37], which could cause increase in extracellular Mn^{2+} concentration, and thus lead to more Mn^{2+} uptake by PC-12 cells.

2.3.2. Manganese Uptake by Glial Cells

No significant exogenous manganese uptake by glial cells was observed in this study at any extracellular $MnCl_2$ concentration, glial activation level, or times of exposure (data not shown). The ICP/MS measurements showed that the intrinsic manganese content in astrocytes and microglia was 50-70 ppb, which is about 30-50 times higher than that of PC-12 cells at baseline (measured at 0 µM $MnCl_2$). The intrinsic manganese concentrations of glial cells measured in this work are in agreement with previous studies [38,39]. The high intrinsic Mn^{2+} concentration in glial cells indicates that Mn^{2+} is an important element for the function of glial cells.

2.3.3. MRI Signal Enhancement and Enhanced Volume Measurements

At Day 1 after LPS/PBS injections, signal enhancement was found only in 2 mice in each group. Signal enhancement at Day 1 was negligible as compared to Day 7, and was not significantly different between the LPS + $MnCl_2$ and PBS + $MnCl_2$ groups (Data not shown). At Day 7 after LPS injection, T_1-wt images of the LPS + $MnCl_2$ group showed strong signal enhancement around the injection line compared to both the surrounding tissue and the corresponding region in the contralateral hemisphere. The T_1-wt image of a Day 7 LPS + $MnCl_2$ mouse was shown in Fig. 2.3.a in three orthogonal planes: coronal (upper left), sagittal (upper right) and axial (bottom left). The areas around the injection line were encased by red boxes and shown in magnified windows in Fig. 2.3.a. The signal enhancement in this area was robust. The T_1-wt image of a PBS + $MnCl_2$ mouse was shown in Fig. 2.3.b. The PBS injected mice showed minimal enhancement compared to the LPS injected mice. The enhancement ratios calculated in the PBS + $MnCl_2$ and LPS + $MnCl_2$ groups are shown in Fig. 2.3.c. Statistical analysis showed significantly higher signal enhancement ratio in the LPS + $MnCl_2$ group as compared to the PBS + $MnCl_2$ group, $p < 0.01$. Similarly as shown in Fig. 2.3.d, enhanced tissue volumes (after normalization by injection depths) were significantly larger in the LPS + $MnCl_2$ group than in the PBS + $MnCl_2$ group, $p < 0.001$. There was no obvious signal enhancement in the mice injected with only LPS but not $MnCl_2$ (the LPS + saline group) as shown in Fig. 2.3.e.

2.3.4. Immunohistology

At Day 1 after LPS/PBS injection, no reactive astrocytes were found, and only microglia detected by Iba-1 were observed in LPS injected mice around the injection line. A brain

slice of a LPS + MnCl$_2$ mouse at Day 1 is shown in Fig. 2.4.a. The Iba-1 staining on a region around the injection line (red box) is shown in a magnified (20X) window. As described in the preceding paragraph, no significant MEMRI signal enhancement was observed in these mice (data not shown). Both astrocytic and microglial reactivity were detected at Day 7 in LPS injected mice. The top row in Fig. 2.4.b shows a brain slice of a LPS + MnCl$_2$ mouse at Day 7. The GFAP and Iba-1 staining on a region around the injection line are shown in magnified (20x) windows. It can be seen that a large number of activated astrocytes were detected by GFAP, and activated microglia by Iba-1, in this region. A brain slice of a PBS + MnCl$_2$ mouse is shown in the 2nd row in Fig. 2.4.b. The areas stained by GFAP and Iba-1 in the region about the injection line (red box) were much smaller compared to the LPS + MnCl$_2$ mouse. In quantitative analysis, at Day 7, the astrocytic reactivity represented by GFAP expression ($p < 0.01$) and microglial reactivity by Iba-1 expression ($p < 0.05$) were significantly higher in the LPS + MnCl$_2$ group than in the PBS + MnCl$_2$ group (Fig. 2.4.c). Immunofluorescence labeling for neuronal markers (SYN and MAP2) showed no significant difference in neuronal loss between LPS + MnCl$_2$ and PBS + MnCl$_2$ groups around the injection lines (data not shown).

Fig. 2.5.a shows that the correlation between astrocyte and microglial reactivity is significant (Pearson's correlation coefficient, $r = 0.62$, $p < 0.05$) in the LPS + MnCl$_2$ group at Day 7. More interesting is that, at Day 7 in the LPS + MnCl$_2$ group, there was a significant correlation between astrocytic reactivity and enhanced tissue volume calculated from MEMRI data (Pearson's correlation coefficient, $r = 0.66$, $p < 0.05$) as

shown in Fig. 2.5.b. No correlation was found between microglial reactivity and enhanced tissue volume.

(a)

(b)
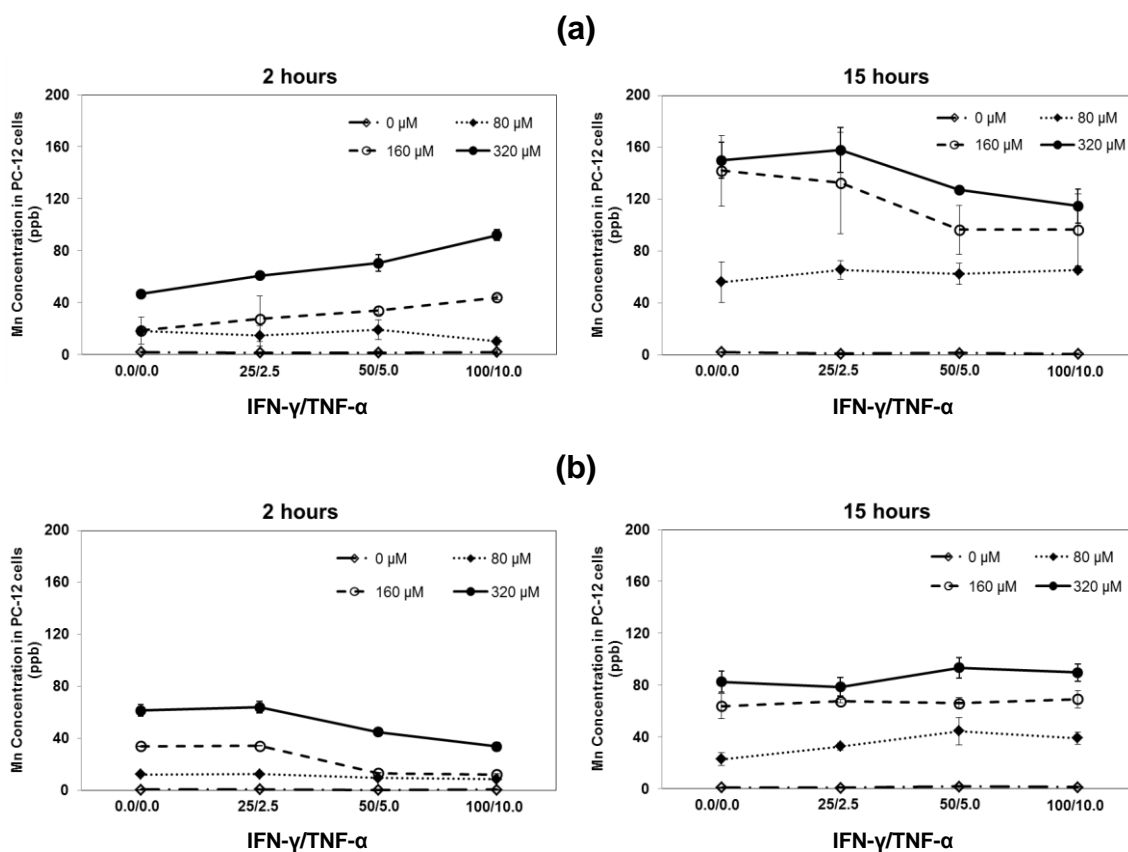
Figure 2.2. Mn^{2+} concentration in PC-12 cells co-cultured with astrocytes plotted against cytokine treatment level (IFN-γ/TNF-α, ng/ml) at 2 hours (Left) and 15 hours (Right) of $MnCl_2$ incubation. **(b)** Mn^{2+} concentration in PC-12 cells co-cultured with microglia plotted against cytokine treatment level (IFN-γ/TNF-α, ng/ml) at 2 hours and 15 hours of $MnCl_2$ incubation.

(a)

Coronal   Sagittal   Axial

(b)

Coronal   Sagittal   Axial

(c)

(d)

(e)
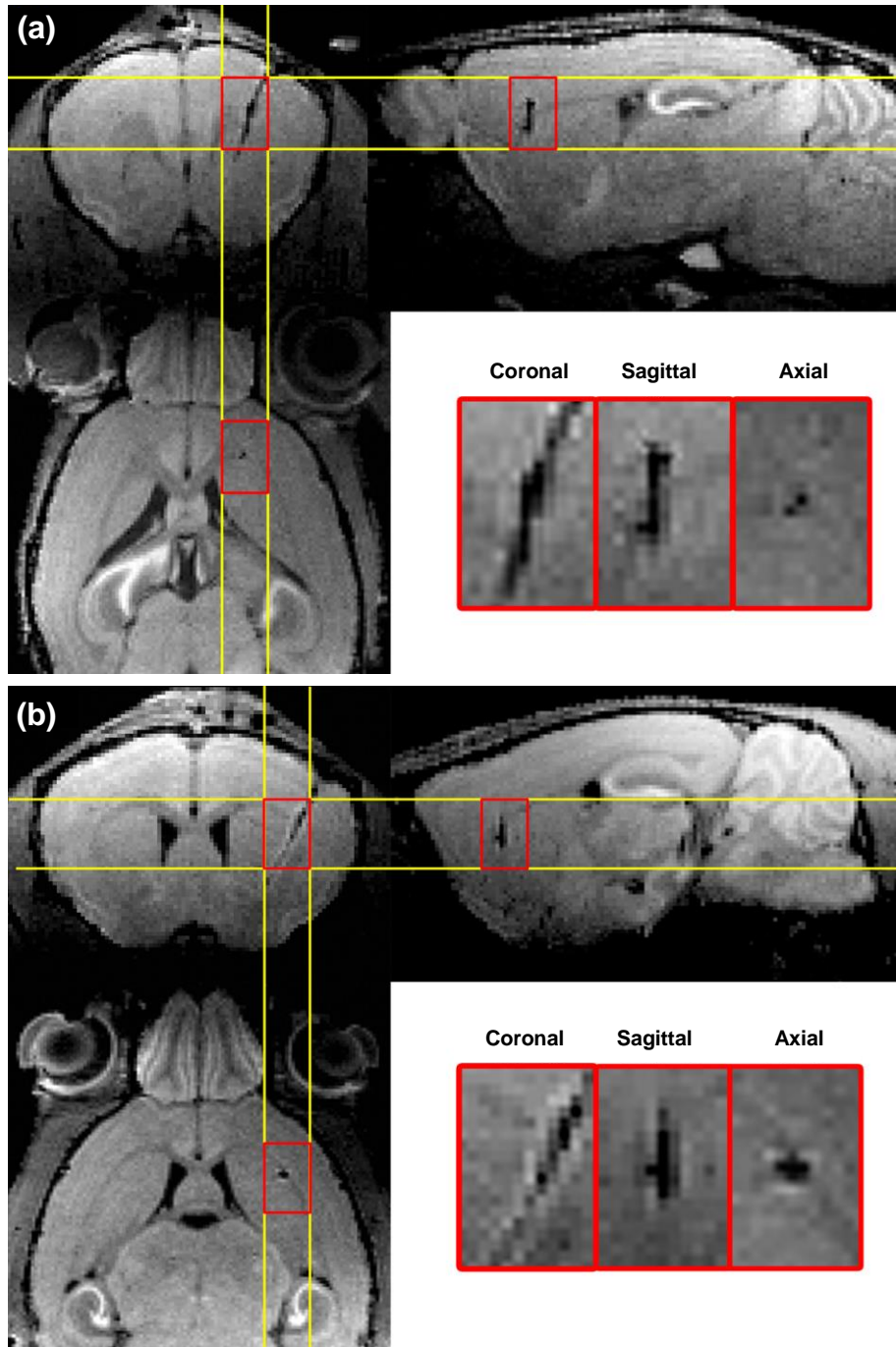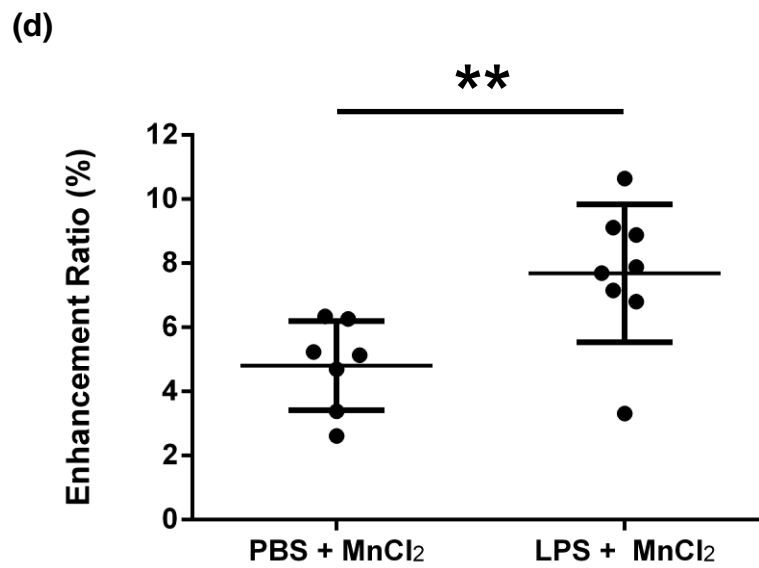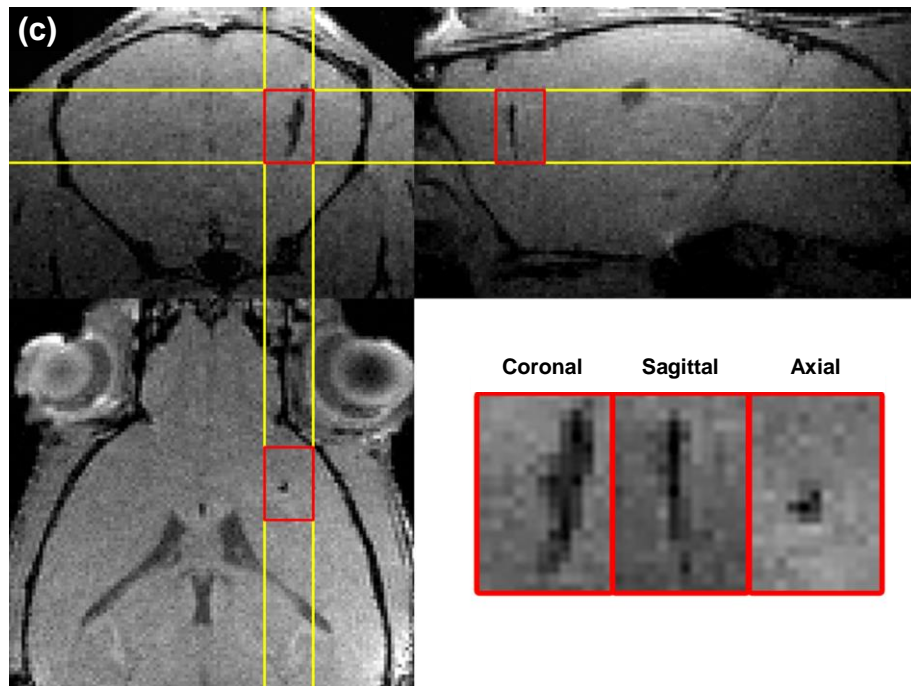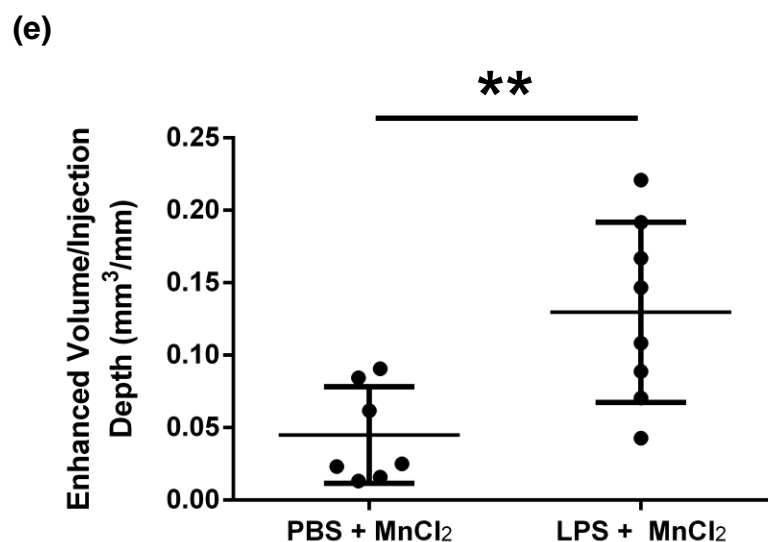
Figure. 2.3. T_1-wt images and enhancement quantification. **(a)** T1-wt image of a PBS + MnCl$_2$ mouse. The image was shown in sagittal, coronal and axial directions (counter-clockwise starting from upper right). Areas around the injection line were encased by red boxes and shown in magnified windows. **(b)** T1-wt image of a LPS + MnCl$_2$ mouse. **(c)** T1-wt image of a LPS only (no MnCl$_2$ injection) mouse. No obvious signal enhancement was observed in the mice injected with only LPS but not MnCl$_2$. **(d)** Enhancement measurements. The LPS + MnCl$_2$ group showed significantly higher signal enhancement than the PBS + MnCl$_2$ group (p<0.01). **(e)** Enhanced volume. Enhanced volumes (normalized by dividing it by respective Injection depths). The LPS + MnCl$_2$ group showed significantly larger enhanced volumes (p<0.01).

(a)

Iba-1

LPS + MnCl$_2$

(b)

GFAP   Iba-1

PBS + MnCl$_2$

LPS + MnCl$_2$

(c)
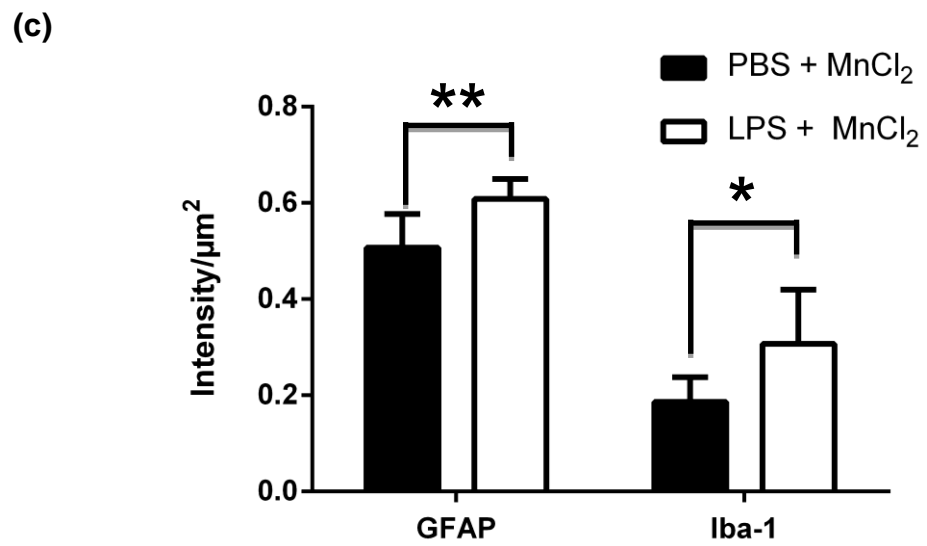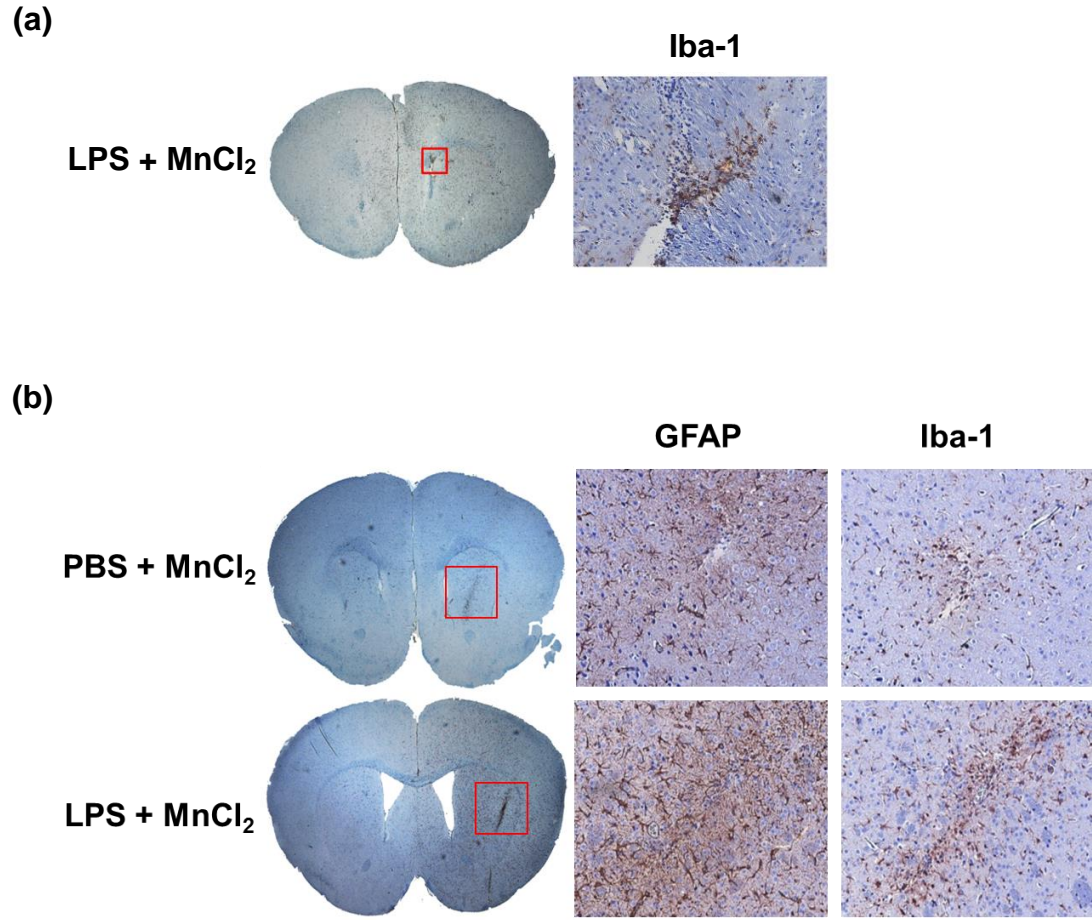
Figure. 2.4. Immunohistology. **(a)** A brain section of a LPS + $MnCl_2$ mouse at Day 1 after LPS injection. The reactive microglia by Iba-1 in the regions encased in red boxes about the injection line are shown at 20x. **(b)** A brain section of a LPS + $MnCl_2$ mouse (top row) and of a PBS + $MnCl_2$ mouse (2nd row). The reactive astrocytes by GFAP and microglia by Iba-1 in the regions encased in red boxes around the injection line are shown at 20x. **(c)** Glial reactivity quantification. Astrocytic and microglial reactivity represented by GFAP and IBa-1 expressions (Intensity/μm^2) were significantly higher in the LPS + $MnCl_2$ group compared to the PBS + $MnCl_2$ group ($p < 0.01$ and $p < 0.05$, respectively)

(a)

(b)
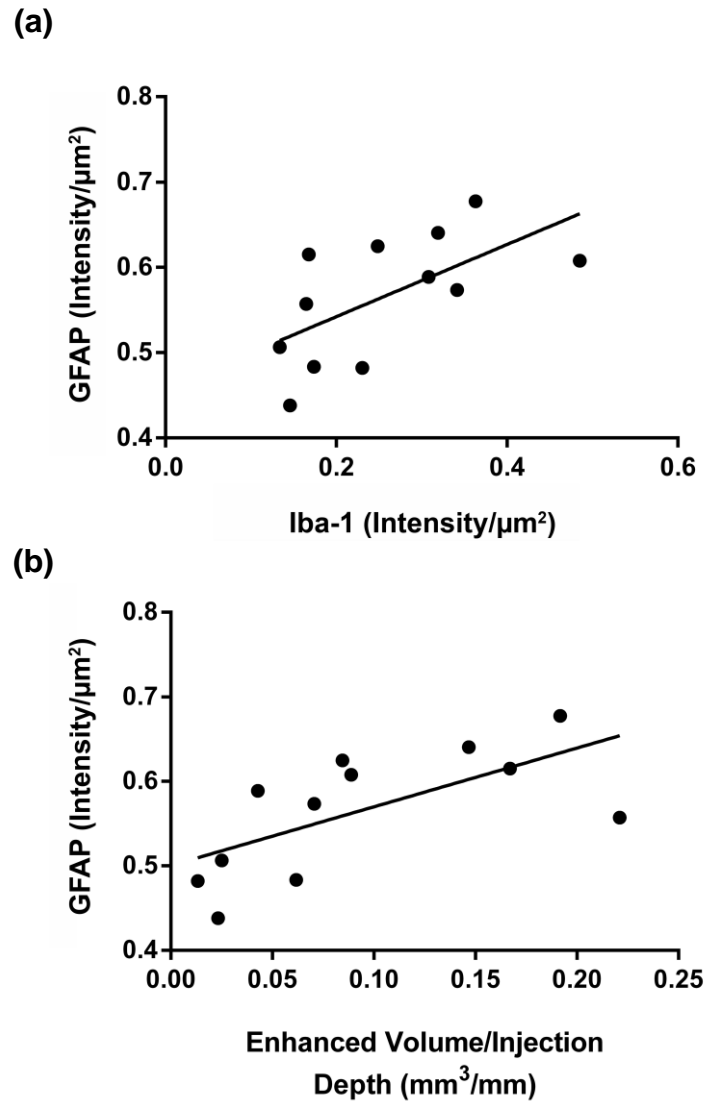
Figure. 2.5. Correlation comparisons. **(a)** Correlation between astrocytic and microglial reactivity ($r = 0.62$, $p < 0.05$). **(b)** Correlation between astrocytic reactivity and enhanced volume ($r = 0.66$, $p < 0.05$)

2.4. Discussion

Intrinsic manganese content in neurons is low compared to glial cells, and neuronal manganese uptake is partly dependent on the availability of extrinsic manganese. Here we investigate the effect of glial reaction on glial and neuronal manganese uptake. The results suggest that inflammatory cytokine induced astrocytic activation [40] stimulates Mn^{2+} uptake of neurons, and that this uptake is proportional to the level of activation. On the other hand, microglial reaction has no direct effect in stimulating neuronal Mn^{2+} uptake, and intensive microglial reaction may even suppress uptake.

The intrinsic manganese content in astrocytes and microglia is much higher than in PC-12 cells as shown in this study and others [38,39]. The high intrinsic Mn^{2+} concentration in glial cells indicates that Mn^{2+} is an important element for the function of these cells. Studies have found that activity of several enzymes in the central nervous system is Mn^{2+} dependent, such as superoxide dismutase, ATPase, and glutamine synthase [37]. No significant exogenous Mn^{2+} uptake by glial cells was observed in this study at any extracellular $MnCl_2$ concentration or glial activation level or time.

The *in vivo* imaging study was designed to reveal the effects of microglial and astrocytic reactions on MEMRI signal enhancement. The imaging times of Day 1 and Day 7 were chosen because, after one day of LPS injection, microglial reaction is well defined, and astrocytic reaction generally takes place after three-four days, and becomes well established around seven days.

The *in vivo* study has clearly demonstrated the co-localization and strong correlation between reactive astrocytes and MEMRI signal enhancement. By incorporating the *in vitro* finding that reactive astrocytes stimulate neuronal manganese

uptake rather than absorb manganese themselves, we are confident to conclude that the MEMRI signal enhancement resulted from the elevated manganese uptake in neurons stimulated by astrocytic reaction.

In GFAP stained brain slices, we also found activated astrocytes in regions remote from the injection line in the LPS + Mn^{2+} mice. However the number of the activated astrocytes in these regions was small. The neuronal Mn^{2+} uptake caused by these astrocytes was not detected in MRI due to the limited sensitivity.

Several groups have studied the relationship between MEMRI signal enhancement and glial reaction in a range of animal models of human disease, including but not limited to, cathepsin D deficiency [26], epilepsy [8], ischemia [14,22,27]and prenatal X-ray exposure [9]. However, results have been varied. Some studies showed elevated MEMRI signal enhancement co-localized with activated microglia [26] or both activated microglia and astrocytes [14,22,27]. However the study of prenatal X-ray exposure [9] found negative correlation between brain tissue longitudinal relaxivity (R_1) and reactive astrocytes. Because R_1 determines MEMRI signal intensity, this study suggested that astrocytic reaction suppressed signal enhancement. Another study of epilepsy [8] found no correlation between MEMRI signal change and astrocytic reaction. The inconsistent results from these studies could be due to the variety of disease models used. In these diseases, a variety of pathobiological events occur in addition to glial reaction, such as cell swelling and necrosis [14,22,27], apoptosis [26], and hippocampal mossy fiber spouting [8]. These events can impair neurons that could either stimulate or suppress neuronal Mn^{2+} uptake, causing inconsistent MEMRI signal enhancement. One particular study [24] using rats, found strong positive correlation between MEMRI signal

enhancement and astrocytic reaction in a stroke model, and proposed that the signal enhancement is caused by Mn^{2+} accumulation in reactive astrocytes through voltage-gated Ca^{2+} channels. However, this study did not investigate the neuronal reaction to glial activation, and thus cannot exclude the contribution of elevated Mn^{2+} uptake by reactive neurons to signal enhancement.

Astrocytes react rapidly to various neurodegenerative insults. Reactive astrocytes protect neurons by secluding the injury site from the rest of the CNS area, and secreting multiple neurotrophic factors to aid neuronal survival. However, the astrocytic processes have been implicated in the pathogenesis of a variety of neurodegenerative diseases, including but not limited to, Alzheimer's disease, Parkinson's disease, HIV-associated neurocognitive disorders, acute traumatic brain injury, and inflammatory demyelinating diseases. It is believed that rapid and severe astrocytic reaction initiates or augments inflammatory response by secreting various pro-inflammatory molecules leading to neuronal death and brain injury [40].

Monitoring glial-neuronal interactions dynamically using noninvasive imaging technologies is a unique and powerful method, which can be used to understand the pathobiology of neurodegenerative diseases, provide diagnosis and prognosis, and aid in the development of therapeutic methods. MRI is a noninvasive imaging technology providing high spatial resolution, excellent soft tissue contrast and real-time measurements. Because Mn^{2+} crosses the brain-blood barrier and enters neurons through voltage-gated calcium channels [41], MEMRI has proven to be a powerful tool to study neuronal viability, activation and impairment. The results in this study show the potential to use MEMRI monitoring of glial-neuronal interactions in normal and abnormal

conditions. Our immunohistological results showed no significant neuronal death caused by LPS injection at the times when MEMRI was performed. In the future we plan to extend the study to later stages at which neuronal death induced by glial reaction occurs. We expect to see decreased MEMRI signal enhancement due to the neuronal death as shown in several previous studies [10,11,13]. Therefore a longitudinal MEMRI study showing neuronal excitation by astrocytic reaction and neuronal death later provides valuable information of the progression of pathobiology.

In conclusion, we demonstrated that astrocytic reaction induces elevated neuronal Mn^{2+} uptake that results in MEMRI signal enhancement. This study demonstrates that MEMRI can be used not only to monitor neuronal vitality and activity but also to monitor astrocyte-neuronal interactions in animal model systems of neurodegenerative diseases.

2.5. References

1. Dobson A. W., Erikson K. M. and Aschner M., (2004) Manganese neurotoxicity. Ann. N. Y. Acad. Sci. 1012, 115-128.

2. Reaney S. H., Kwik-Uribe C. L. and Smith D. R., (2002) Manganese oxidation state and its implications for toxicity. Chem. Res. Toxicol. 15, 1119-1126.

3. Silva A. C., Lee J. H., Aoki I. and Koretsky A. P., (2004) Manganese-enhanced magnetic resonance imaging (MEMRI): methodological and practical considerations. NMR Biomed. 17, 532-543.

4. Koretsky A. P. and Silva A. C., (2004) Manganese-enhanced magnetic resonance imaging (MEMRI). NMR Biomed. 17, 527-531.

5. Pautler R. G., (2006) Biological applications of manganese-enhanced magnetic resonance imaging. Methods Mol. Med. 124, 365-386.

6. Silva A. C. and Bock N. A., (2008) Manganese-enhanced MRI: an exceptional tool in translational neuroimaging. Schizophr. Bull. 34, 595-604.

7. Van der Linden A., Van Camp N., Ramos-Cabrer P. and Hoehn M., (2007) Current status of functional MRI on small animals: application to physiology, pathophysiology, and cognition. NMR Biomed. 20, 522-545.

8. Immonen R. J., Kharatishvili I., Sierra A., Einula C., Pitkanen A. and Grohn O. H., (2008) Manganese enhanced MRI detects mossy fiber sprouting rather than

neurodegeneration, gliosis or seizure-activity in the epileptic rat hippocampus. Neuroimage. 40, 1718-1730.

9. Saito S., Aoki I., Sawada K. and Suhara T., (2012) Quantitative assessment of central nervous system disorder induced by prenatal X-ray exposure using diffusion and manganese-enhanced MRI. NMR Biomed. 25, 75-83.

10. Bertrand A., Khan U., Hoang D. M., Novikov D. S., Krishnamurthy P., Rajamohamed Sait H. B., Little B. W., Sigurdsson E. M. and Wadghiri Y. Z., (2013) Non-invasive, in vivo monitoring of neuronal transport impairment in a mouse model of tauopathy using MEMRI. Neuroimage. 64, 693-702.

11. Perez P. D., Hall G., Kimura T., Ren Y., Bailey R. M., Lewis J., Febo M. and Sahara N., (2013) In vivo functional brain mapping in a conditional mouse model of human tauopathy (tauP301L) reveals reduced neural activity in memory formation structures. Mol. Neurodegener. 8, 9-1326-8-9.

12. Drobyshevsky A., Yu L., Yang Y., Khalid S., Luo K., Jiang R., Ji H., Derrick M., Kay L., Silverman R. B. and Tan S., (2012) Antenatal insults modify newborn olfactory function by nitric oxide produced from neuronal nitric oxide synthase. Exp. Neurol. 237, 427-434.

13. Haenold R., Herrmann K. H., Schmidt S., Reichenbach J. R., Schmidt K. F., Lowel S., Witte O. W., Weih F. and Kretz A., (2012) Magnetic resonance imaging of the mouse visual pathway for in vivo studies of degeneration and regeneration in the CNS. Neuroimage. 59, 363-376.

14. Morken T. S., Wideroe M., Vogt C., Lydersen S., Havnes M., Skranes J., Goa P. E. and Brubakk A. M., (2013) Longitudinal diffusion tensor and manganese-enhanced MRI detect delayed cerebral gray and white matter injury after hypoxia-ischemia and hyperoxia. Pediatr. Res. 73, 171-179.

15. Wideroe M., Havnes M. B., Morken T. S., Skranes J., Goa P. E. and Brubakk A. M., (2012) Doxycycline treatment in a neonatal rat model of hypoxia-ischemia reduces cerebral tissue and white matter injury: a longitudinal magnetic resonance imaging study. Eur. J. Neurosci. 36, 2006-2016.

16. Bouilleret V., Cardamone L., Liu C., Koe A. S., Fang K., Williams J. P., Myers D. E., O'Brien T. J. and Jones N. C., (2011) Confounding neurodegenerative effects of manganese for in vivo MR imaging in rat models of brain insults. J. Magn. Reson. Imaging. 34, 774-784.

17. Chan K. C., Cheng J. S., Fan S., Zhou I. Y. and Wu E. X., (2011) In vivo manganese-enhanced MRI and diffusion tensor imaging of developing and impaired visual brains. Conf. Proc. IEEE Eng. Med. Biol. Soc. 2011, 7005-7008.

18. Kim J., Choi I. Y., Michaelis M. L. and Lee P., (2011) Quantitative in vivo measurement of early axonal transport deficits in a triple transgenic mouse model of Alzheimer's disease using manganese-enhanced MRI. Neuroimage. 56, 1286-1292.

19. Smith K. D., Paylor R. and Pautler R. G., (2011) R-flurbiprofen improves axonal transport in the Tg2576 mouse model of Alzheimer's disease as determined by MEMRI. Magn. Reson. Med. 65, 1423-1429.

20. Soria G., Aguilar E., Tudela R., Mullol J., Planas A. M. and Marin C., (2011) In vivo magnetic resonance imaging characterization of bilateral structural changes in experimental Parkinson's disease: a T2 relaxometry study combined with longitudinal diffusion tensor imaging and manganese-enhanced magnetic resonance imaging in the 6-hydroxydopamine rat model. Eur. J. Neurosci. 33, 1551-1560.

21. Tang H. L., Sun H. P., Wu X., Sha H. Y., Feng X. Y. and Zhu J. H., (2011) Detection of neural stem cells function in rats with traumatic brain injury by manganese-enhanced magnetic resonance imaging. Chin. Med. J. (Engl). 124, 1848-1853.

22. Wideroe M., Brekken C., Kavelaars A., Pedersen T. B., Goa P. E., Heijnen C., Skranes J. and Brubakk A. M., (2011) Longitudinal manganese-enhanced magnetic resonance imaging of delayed brain damage after hypoxic-ischemic injury in the neonatal rat. Neonatology. 100, 363-372.

23. Inoue Y., Aoki I., Mori Y., Kawai Y., Ebisu T., Osaka Y., Houri T., Mineura K., Higuchi T. and Tanaka C., (2010) Detection of necrotic neural response in super-acute cerebral ischemia using activity-induced manganese-enhanced (AIM) MRI. NMR Biomed. 23, 304-312.

24. Kawai Y., Aoki I., Umeda M., Higuchi T., Kershaw J., Higuchi M., Silva A. C. and Tanaka C., (2010) In vivo visualization of reactive gliosis using manganese-enhanced magnetic resonance imaging. Neuroimage. 49, 3122-3131.

25. van Meer M. P., van der Marel K., Otte W. M., Berkelbach van der Sprenkel J. W. and Dijkhuizen R. M., (2010) Correspondence between altered functional and structural

connectivity in the contralesional sensorimotor cortex after unilateral stroke in rats: a combined resting-state functional MRI and manganese-enhanced MRI study. J. Cereb. Blood Flow Metab. 30, 1707-1711.

26. Haapanen A., Ramadan U. A., Autti T., Joensuu R. and Tyynela J., (2007) In vivo MRI reveals the dynamics of pathological changes in the brains of cathepsin D-deficient mice and correlates changes in manganese-enhanced MRI with microglial activation. Magn. Reson. Imaging. 25, 1024-1031.

27. Wideroe M., Olsen O., Pedersen T. B., Goa P. E., Kavelaars A., Heijnen C., Skranes J., Brubakk A. M. and Brekken C., (2009) Manganese-enhanced magnetic resonance imaging of hypoxic-ischemic brain injury in the neonatal rat. Neuroimage. 45, 880-890.

28. Greene L. A. and Tischler A. S., (1976) Establishment of a noradrenergic clonal line of rat adrenal pheochromocytoma cells which respond to nerve growth factor. Proc. Natl. Acad. Sci. U. S. A. 73, 2424-2428.

29. Vignali G., Niclas J., Sprocati M. T., Vale R. D., Sirtori C. and Navone F., (1996) Differential expression of ubiquitous and neuronal kinesin heavy chains during differentiation of human neuroblastoma and PC12 cells. Eur. J. Neurosci. 8, 536-544.

30. Singh N. S., Paul R. K., Torjman M. C. and Wainer I. W., (2013) Gabapentin and (S)-pregabalin decrease intracellular D-serine concentrations in PC-12 cells. Neurosci. Lett. 535, 90-94.

31. Zhang X. H., Ma Z. G., Rowlands D. K., Gou Y. L., Fok K. L., Wong H. Y., Yu M. K., Tsang L. L., Mu L., Chen L., Yung W. H., Chung Y. W., Zhang B. L., Zhao H. and Chan H. C., (2012) Flavonoid Myricetin Modulates GABA(A) Receptor Activity through Activation of Ca(2+) Channels and CaMK-II Pathway. Evid Based. Complement. Alternat Med. 2012, 758097.

32. Kwik-Uribe C. L., Reaney S., Zhu Z. and Smith D., (2003) Alterations in cellular IRP-dependent iron regulation by in vitro manganese exposure in undifferentiated PC12 cells. Brain Res. 973, 1-15.

33. Zheng W. and Zhao Q., (2001) Iron overload following manganese exposure in cultured neuronal, but not neuroglial cells. Brain Res. 897, 175-179.

34. Yamamoto M., Kiyota T., Horiba M., Buescher J. L., Walsh S. M., Gendelman H. E. and Ikezu T., (2007) Interferon-gamma and tumor necrosis factor-alpha regulate amyloid-beta plaque deposition and beta-secretase expression in Swedish mutant APP transgenic mice. Am. J. Pathol. 170, 680-692.

35. Kiyota T., Yamamoto M., Xiong H., Lambert M. P., Klein W. L., Gendelman H. E., Ransohoff R. M. and Ikezu T., (2009) CCL2 accelerates microglia-mediated Abeta oligomer formation and progression of neurocognitive dysfunction. PLoS One. 4, e6197.

36. Sled J. G., Zijdenbos A. P. and Evans A. C., (1998) A nonparametric method for automatic correction of intensity nonuniformity in MRI data. IEEE Trans. Med. Imaging. 17, 87-97.

37. Wedler F. C., Ley B. W. and Grippo A. A., (1989) Manganese(II) dynamics and distribution in glial cells cultured from chick cerebral cortex. Neurochem. Res. 14, 1129-1135.

38. Takeda A., (2003) Manganese action in brain function. Brain Res. Brain Res. Rev. 41, 79-87.

39. Tholey G., Bloch S., Ledig M., Mandel P. and Wedler F., (1987) Chick brain glutamine synthetase and Mn2+-Mg2+ interactions. Neurochem. Res. 12, 1041-1047.

40. Yenari, M. A. and Giffard, R. G. (2006) Glia And Inflammation In Neurodegenrative Disese, Nova Science Publisher, Inc., New York,.

41. Inoue T., Majid T. and Pautler R. G., (2011) Manganese enhanced MRI (MEMRI): neurophysiological applications. Rev. Neurosci. 22, 675-694.

CHAPTER - 3

Manganese-Enhanced Magnetic Resonance Imaging (MEMRI)

Detects Brain Pathology in Animal Models of

Neurodegenerative Diseases

3.1. Introduction

HIV-1-associated neurocognitive disorders (HAND) is a clinical disorder that reflects the cognitive, behavioral and motor dysfunctions associated with progressive viral infection [1]. HAND reflects a spectrum of clinical abnormalities that include asymptomatic neurocognitive impairment (ANI), mild neurocognitive disorder (MND) and HIV-associated dementia (HAD) [2]. Although antiretroviral therapy (ART) has significantly decreased the HAD incidence and prevalence, ANI and MND are seen in half of infected patients [3] and as such continues to be a significant quality of life complication of HIV/AIDS [4,5]. Despite advances in the understanding HIV neuropathobiology, disease diagnosis is made by exclusion of co-morbid conditions such as drug abuse, neurodegenerative and psychiatric disorders, opportunistic infections and malignancies [6]. Moreover, levels of viral replication and cognitive impairment are not always linked nor do they provide clear relationships between neuropathology and cognitive function [4]. It is possible that diagnostic clarity could be provided through imaging biomarkers.

In attempts to detail HIV-associated neuropathology, our laboratories pioneered the development of murine models of virus-associated brain disease [7]. Specifically, we show that humanized mice reconstituted with CD34+ human hematopoietic stem cells reflect the consequences of viral infection and consequent immune deterioration in its human host [8-11]. In this model, human progenitor cells are transplanted into genetically modified immunodeficient NOD/scid-IL-2Rγc^{null} (NSG) mice [12]. Such mice support persistent HIV-1 infection leading to behavioral and motor impairments paralleling

neuronal and glial responses [13]. Our recent works demonstrated that brain imaging such as proton magnetic resonance spectroscopy (^{1}H MRS) and diffusion tensor imaging (DTI) can uncover the neuropathological consequences of chronic HIV-1 infection in these mice [8,13].

A significant advantage for manganese-enhanced magnetic resonance imaging (MEMRI) over other magnetic resonance imaging (MRI) modalities rests in the ability to directly map voltage-gated calcium channel activity through manganese ions (Mn^{2+}) neuronal accumulation. As Mn^{2+} is a calcium (Ca^{2+}) analogue, it can enter neurons by voltage-gated Ca^{2+} channels[14] and can be moved anterograde by axonal transport and microtubule assembly [15,16]. Mn^{2+} is an excellent T_1 shortening contrast agent affording relatively high spatial resolution and signal-to-noise ratio within reasonable scanning time [17,18]. Administration of Mn^{2+} generates enhanced signal intensity on T_1-wt images. The signal enhancement is associated with neuronal activities. MEMRI can assess neuronal well-being for anatomical, integrative, functional and axonal transport activities of nerve cells and their connections [14,19]. Herein, we demonstrate that MEMRI facilitates precise noninvasive high spatial resolution (100 μm^3 isotropic) determinations of brain regions of HIV-1 incited neuroinflammation and neuronal injury in NOD/scid-IL-2Rγc^{null} humanized mice. Correlations between immunocytochemical measures of brain disease and MEMRI signal enhancement are operative.

3.2. Materials and Methods

3.2.1. Murine neuroAIDS model

NOD/scid-IL-2Rγc$^{\text{null}}$ (NSG) mice were bred under specific-pathogen-free conditions in accordance with the ethical guidelines at the University of Nebraska Medical center (UNMC), Omaha, Nebraska. Human cord blood obtained with parental written informed consent from healthy full-term newborns (Department of Gynecology and Obstetrics, UNMC) was utilized for CD34+ cells isolation using immune-magnetic beads according to the manufacturer's instructions (CD34+ selection kit; Miltenyi Biotec Inc., Auburn, CA). Numbers and purity of human CD34+ cells were evaluated by fluorescence-activated cell sorting (FACS). Cells were either frozen or immediately transplanted into newborn mice at 10^5/mouse intrahepatically (i.h.) in 20 μl phosphate-buffered saline (PBS) using a 30-gauge needle. Newborn mice received human cells from single donors. On the day of birth, newborn mice were irradiated at 1 Gy using a C9 cobalt 60 source (Picker Corporation, Cleveland, OH). Starting from 22 weeks after reconstitution, HIV-1 virus was intraperitoneally (i.p.) injected at 10^4 TCID$_{50}$ into mice. Humanized mice without infection served as controls. Number of human cells and the level of engraftment were analyzed by flow cytometry. In the study, all protocols related to animal experiments were approved by the Institutional Animal Care and Use Committee (IACUC), UNMC University and met the requirements of the UNMC University ethical guidelines, which are set forth by the National Institutes of Health.

3.2.2. Viral load

The automated COBAS Amplicor System V1.5 (Roche Molecular Diagnostics, Basel, Switzerland) was used to measure the peripheral level of viral RNA copies/ml. Mouse

plasma (20 µl) was used to dilute with 480 µl of sterile normal human plasma for the assay. The baseline detection of assay after dilution is 1250 viral RNA copies/ml.

3.2.3. Flow cytometry

Peripheral blood leukocytes, spleen and bone marrow cell suspensions were examined for anti-human-CD45, CD3, CD4 and CD8 markers. Flow cytometry on peripheral blood leukocytes was done every other week from the point of infection. At the end of study, flow cytometry was done for spleen and bone marrow as well. Mouse peripheral blood samples were collected from submandibular vein (cheek bleed) by using lancets (MEDIpoint, Inc., Mineola, NY) in EDTA coated tubes. Antibodies and isotype controls (BD Phar-Mingen, San Diego, CA) were used to stain cells. Staining was analyzed by using FACSDiva (BD Immunocytometry Systems, Mountain View, CA). Percentages of total gated lymphocytes were expressed as results.

3.2.4. Immunohistology

At 16 weeks, mice were euthanized immediately after imaging and brains were collected. Brain tissues were fixed in 4% paraformaldehyde overnight and embedded in paraffin. Five µm thick brain tissue sections were labeled with mouse monoclonal antibodies for HLA-DQ/DP/DR (1:100, Dako, Carpinteria, CA), HIV-1 p24 (1:10, Dako), c-Fos (1:50, Santa Cruz Biotechnology, Santa Cruz, CA), and rabbit polyclonal antibodies for glial fibrillary acidic protein (GFAP) (1:1000, Dako), ionized calcium binding adaptor molecule -1 (Iba-1) (1:500; Wako Chemicals, Richmond, VA), Caspase3 (1:10, EMD Millipore, Billerica, MA). The polymer-based HRP-conjugated anti-mouse and anti-

rabbit Dako EnVision systems were used as secondary detection reagents, and 3,3'-diaminbenzidine (DAB, Dako) was used as a chromogen. All paraffin-embedded sections were counterstained with Mayer's hematoxylin. Deletion of primary antibodies served as controls. Images were captured with a 100×, 40× and 20× objectives using Nuance EX multispectral imaging system fixed to a Nikon Eclipse E800 (Nikon Instruments, Melville, NY).

For immunofluorescence labeling, brain sections were treated with the paired combination of primary antibodies mouse anti-synaptophysin (SYN) (1:1000, EMD Millipore), and rabbit anti-microtubule-associated protein 2 (MAP2) (1:500, EMD Millipore), mouse anti-neurofilament (NFs) (1:200, Dako) and rabbit anti-GFAP (1:1000, Dako); additionally, brain sections were treated alone with rabbit anti-Iba-1(1:500). Primary antibodies were labeled with secondary anti-mouse and anti-rabbit antibodies conjugated to the fluorescent probes Alexa Fluor 488 and Alexa Fluor 594, and nuclei were labeled with DAPI (4,6-diamidino-2-phenylindole). Slides were cover-slipped with ProLong Gold anti-fade reagent (Invitrogen, Carlsbad, CA). Slides were stored at −20 °C after drying for 24 hours at room temperature. Images were captured at wavelengths encompassing the emission spectra of the probes, with a 40× objective by Nuance EX multispectral imaging system fixed to a Nikon Eclipse E800 and image analysis software (Caliper Life sciences, Inc., a Perkin Elmer Company, Hopkinton, MA) was used for quantification of SYN, MAP2, NF and GFAP expression. Area-weighted average fluorescence intensity was calculated in the region of interest (ROI) by dividing the total signal intensity, for each partitioned area, by area (μm^2) as intensity/μm^2. Images were also captured with LSM 710 microscope using a 40X oil lens (Carl Zeiss Microscopy,

LLC, NY, USA). Expression of cFos was scored (out of 10) by two investigators using 20× objective in blinded manner. Findings were compared to animals that were not manipulated (score 0). Student's t-tests were performed to compare immunohistological results of the HIV-1 infected animals with controls.

3.2.5. MEMRI

$MnCl_2 \cdot 4H_2O$ (Sigma-Aldrich, St Louis, MO) was added to 0.9% w/v NaCl (Hospira, Lake forest, IL) to make 50 mM $MnCl_2$ solution. $MnCl_2$ solution was administrated i.p. with the dose of 60 mg/kg consecutively four times at 24 hour intervals before MRI. After the injection, the mouse was observed daily to detect the side effects of $MnCl_2$.

MRI data were acquired 24 hours after the last $MnCl_2$ administration on Bruker Bioscan 7 Tesla/21 cm small animal scanner (Bruker, Billerica, MA) operating Paravision 5.1 with a 72 mm volume resonator and a 4-channel phased array coil. Mice were anesthetized by inhalation of isoflurane in 100% oxygen and maintained 40-80 breaths/minute. Mice were scanned using T_1 mapping sequence (fast spin echo with variable repetition time (TR) from 0.4 s to 10 s, 12 slices, slice thickness = 0.5 mm, in-plane resolution = 0.1×0.1 mm^2) and T_1-wt MRI (FLASH, TR = 20 ms, flip angle = 20°, 3D isotropic resolution = $0.1 \times 0.1 \times 0.1$ mm^3). After MRI, the mice were euthanized and tissues were removed for immunohistological study. The same scan was also performed before the $MnCl_2$ administration, and the acquired image was used as baseline data for the calculation of signal enhancement.

3.2.6. MRI data pre-processing

To reduce the influence of the inhomogeneous signal reception on the T_1-wt images by the phased array surface coil, N3 field inhomogeneity correction [20] was first performed on each image using MIPAV (CIT, NIH). The brain volumes in the T_1-wt images were extracted using an in-house Matlab program [21] based on the level sets method. The brain images were then registered to a MEMRI-based NSG mouse brain atlas developed in our laboratories using affine transformation first, and then nonlinear transformation (DiffeoMap, John Hopkins University, Baltimore, MD).

To calculate Mn^{2+} induced T_1-wt signal enhancement, the MRI system variations between the baselines and post $MnCl_2$ injection scans need to be minimized. This is achieved by calibrating the baseline and post Mn^{2+} injection T_1-wt images using T_1 values. A detailed description of the MEMRI enhancement calculation and T_1-wt image calibration are described in the MEMRI signal enhancement and tissue manganese concentration part of the methods and material section of this chapter. The T_1 maps were first generated using an in-house Interactive Data Language (IDL) version 8.2 (Exelis Visual Information Solutions, Boulder, Colorado) program from the data acquired by T_1 mapping sequence. ROIs were then placed on relatively uniform tissue regions including frontal cortex and caudate on T_1 maps and T_1-wt images. The baseline and post Mn^{2+} injection longitudinal relaxivity ($R_{1bl}{}^{ROI}$ and $R_{1Mn}{}^{ROI}$) and T_1-wt signal intensity ($S_{bl}{}^{ROI}$ and $S_{Mn}{}^{ROI}$) in the ROIs were measured. The calibration factor was calculated as $C = (S_{Mn}{}^{ROI}/S_{bl}{}^{ROI}) \times (R1_{bl}{}^{ROI}/R1_{Mn}{}^{ROI})$. The baseline T_1-wt image (S_{bl}) was then calibrated using the calibration factor $C : S_{bl}{}^{C} = S_{bl} \times C$.

3.2.7. MEMRI signal enhancement and tissue manganese concentration

In this study, MEMRI enhancement is defined as $(S_{Mn} - S_{bl})/S_{Mn}$, where S_{bl} and S_{Mn} are the baseline (bl) and manganese enhanced (Mn) signal, respectively. The spoiled FLASH (Fast Low Angle SHot) sequence was used to acquire T_1-wt images in this study. The signal generated using FLASH can be expressed as:

$$S = M_0 \frac{\sin\alpha\left(1-e^{-TR/T_1}\right)}{1-\cos\alpha\, e^{-TR/T_1}} e^{-TE/T_2^*} \qquad (1),$$

where M_0 is the spin density, TR and TE are repetition and echo time, respectively. α is the flip angle. Therefore, the baseline and manganese enhanced signal are

$$S_{bl} = M_0 \frac{\sin\alpha\left(1-e^{-TR/T_{1bl}}\right)}{1-\cos\alpha\, e^{-TR/T_{1bl}}} e^{-TE/T_{2bl}^*} \qquad (2),$$

and

$$S_{Mn} = M_0 \frac{\sin\alpha\left(1-e^{-TR/T_{1Mn}}\right)}{1-\cos\alpha\, e^{-TR/T_{1Mn}}} e^{-TE/T_{2Mn}^*} \qquad (3).$$

The ratio of the manganese enhanced and baseline signals is

$$\frac{S_{Mn}}{S_{bl}} = \frac{(1-e^{-TR/T_{1Mn}})\cdot e^{-TE/T_{2Mn}^*}\cdot\left(1-\cos\alpha\, e^{-TR/T_{1bl}}\right)}{(1-e^{-TR/T_{1bl}})\cdot e^{-TE/T_{2bl}^*}\cdot\left(1-\cos\alpha\, e^{-TR/T_{1Mn}}\right)} \qquad (4).$$

T_2 reduction caused by manganese administration is much less pronounced than T_1 reduction. A previous study showed that in rat cortex, the T_2 reduction is about 10% at 24 hours after $MnCl_2$ injection, while T_1 reduces approximately 30% (Chuang KH et al., Magnetic Resonance in Medicine, 2009, doi: 10.1002/mrm.21962, PMID:19353652). TE is also relatively short as well (=3 ms) in this study. Therefore Eqn (5) can be simplified as

$$\frac{S_{Mn}}{S_{bl}} = \frac{(1-e^{-TR/T_{1Mn}})\cdot\left(1-\cos\alpha\, e^{-TR/T_{1bl}}\right)}{(1-e^{-TR/T_{1bl}})\cdot\left(1-\cos\alpha\, e^{-TR/T_{1Mn}}\right)} \qquad (5)$$

Recall the Taylor expansion:

$$e^x = 1 + x + \frac{x^2}{2!} + \frac{x^3}{3!} + \dots \qquad (6).$$

Replace x with $(-TR/T_1)$ in Eqn (6):

$$e^{-TR/T_1} = 1 + (-TR/T_1) + \frac{(-TR/T_1)^2}{2!} + \cdots, \qquad (7),$$

and since TR (= 20 ms) / T_1 (> 800 ms in most regions after manganese administration) is small, the second and higher order terms in Eqn (7) can be ignored, that is, $e^{-TR/T_1} \approx 1 + (-TR/T_1)$. Applying this equation in Eqn (5) and after skipping several steps, Eqn (5) can be further simplified:

$$\frac{S_{Mn}}{S_{bl}} = \frac{(TR/T_{1Mn}) \cdot (1 - \cos\alpha + \cos\alpha(TR/T_{1bl}))}{(TR/T_{1bl}) \cdot (1 - \cos\alpha + \cos\alpha(TR/T_{1Mn}))} \qquad (8).$$

The third terms in both numerator and denominator are at the second order, and thus can be dropped similarly to in Eqn (7):

$$\frac{S_{Mn}}{S_{bl}} = \frac{T_{1bl}(1 - \cos\alpha)}{T_{1Mn}(1 - \cos\alpha)} = \frac{R_{1Mn}}{R_{1bl}} \qquad (9),$$

where R_1 is the relaxitivity, and $R_1 = 1/T_1$. Eqn (9) means that the ratio of the signals acquired before and after manganese administration is equal to the ratio of relaxivities. As $R_{1Mn} = R_{1bl} + r_1*[Mn]$, where r_1 is the molar relaxivity (s^{-1} mM^{-1}) of manganese, and [Mn] is the manganese concentration in mM, Eqn (9) can be rewritten as

$$\frac{S_{Mn}}{S_{bl}} = \frac{R_{1bl} + r_1[Mn]}{R_{1bl}} = 1 + \frac{r_1[Mn]}{R_{1bl}} \qquad (10).$$

Replacing 1 with S_{bl}/S_{bl} and subtracting one from each side:

$$\frac{S_{Mn} - S_{bl}}{S_{bl}} = \frac{r_1[Mn]}{R_{1bl}} \qquad (11).$$

From Eqn (11), we can see the tissue manganese concentration [Mn] is proportional to the normalized signal change induced by manganese administration (i.e., the signal enhancement).

MRI scanner system calibration:

System settings such as RF coil, analogue-to-digital converter, and environment temperature can change in the post-manganese administration imaging session from the pre-administration session. The variation can be minimized by calibrating the system using relaxation times measured before and after manganese administration. If we assume that the effect of the system variation is a constant C (calibration factor) and set system parameter of the post-manganese session as 1, then the acquired baseline signal is $S_{acq} = CS_{bl}$. From Eqn (9),

$$C = \frac{S_{acq}}{S_{Mn}} \cdot \frac{T_{1bl}}{T_{1Mn}} \qquad (12).$$

T_{1bl} and T_{1Mn} were measured using a fast spin echo sequence with variable TR in this study. Using C from Eqn (12), S_{bl} can be calculated: $S_{bl} = Sacq / C$.

3.2.8. MEMRI enhancement analysis

The Mn^{2+} induced T_1-wt signal enhancement was calculated by: $(S_{Mn} - S_{bl}{}^C) / S_{bl}{}^C$. A pixel-by-pixel comparison was first performed between the HIV-1 infected mice and the control group using Student's t-test, followed by a brain region specific analysis. Using the MEMRI-based brain atlas, the T_1-wt signal enhancement on 41 brain regions/sub-regions was calculated. The student's t-test was performed to exam the significance of enhancement change in each HIV-1 infected brain region compared to the control group.

The association between MRI signal changes, plasma viral load, T-cells and immunohistological results in HIV mice was examined using Pearson product-moment correlation. The association between enhancement and quantified GFAP, Iba-1, MAP2, NF and SYN staining was studied on the CA1, CA3 and DG brain regions. Time course of infection that included measures of the plasma viral load at the time of animal sacrifice

(16 WPI), its rate of change (slope) over time, and change in maximum and end time viral levels were measured. These parameters tested over time were correlated with MRI signal enhancements. The T-cell parameters that were measured over time included blood, spleen and bone marrow CD4 and CD8 positive T cell numbers.

3.2.9. Brain structure volumetric analysis

In the MRI data pre-processing, the brain images were registered to the MEMRI-based brain atlas. The 41 brain regions were identified on each brain image. The brain images were transferred back to their original spaces employing the inverse of the transformation matrices calculated for registration. The volumes of the regions were calculated in the original spaces. Student's t-tests were performed to compare the volumes of the HIV-1 infected animals with controls.

3.2.10. Detection of Mn^{2+} toxicity

Animals were observed daily after each i.p. $MnCl_2$ injection and 24 hours after the injection. If tremor or convulsion (the signs of manganese overdose) persisted longer than 3 minutes or lethargy observed at 24 hours, mice were euthanized.

3.3. Results

3.3.1. HIV-1 Infection of humanized mice

Humanized mice (n = 8) were infected with the HIV-1$_{ADA}$ at 22 weeks of age (Fig. 3.1.a). Viral and immune parameters were assessed then compared against controls (uninfected humanized mice, n = 7). Flow cytometry was performed at 2, 4, 7, 10, 13 and 16 weeks

post infection (WPI) to determine reconstitution of peripheral human immune cells (CD45, CD3, CD4, CD8). The temporal changes of CD4+ and CD8+ T cells in infected humanized mice are shown in Fig. 3.1.b. The steady CD4+ T cells decline and concomitant increases in CD8+ T cells were readily seen in HIV-1 infected mice. Control uninfected animals showed no changes in T cell numbers throughout the study period (Fig. 3.1.b). Plasma viral RNA copies/ml (viral load, VL) measures were performed at 2, 7, 16 WPI (Fig. 3.1.c). These VL values peaked at the 2nd week after HIV-1 infection and were sustained throughout the experimental observation period.

3.3.2. Leukocyte brain infiltration

Brain infiltration of human cells including those HIV-1 infected were assessed by immunohistochemical assays. At 16 WPI, brain sections at 5 µm thickness were stained for human HLA-DR and HIV-1p24. Human HLA-DR+ cells infiltrated the brains of infected and control mice were seen in the meninges and perivascular spaces (Fig. 3.1.d). Few HIV-1p24+ human cells were observed in these regions of infected mice (Fig. 3.1.e). Glial responses were assessed by glial fibrillary acidic protein (GFAP, astrocyte) and ionized calcium binding adaptor molecule-1 (Iba-1, microglia) staining. Cortical areas with hypertrophic astrocytes and morphological features of activated microglia were readily observed (Fig. 3.1.f). Such activated glial morphologies were not seen in control animals.

3.3.3. MEMRI

To track neuropathology induced by continuous HIV-1 infection, MEMRI was performed at 16 WPI (Fig. 3.1.a). The averaged MEMRI image of the control mice is shown on coronal brain slices as an anatomical reference in the left column of Figure 3.2.a. Positions of the coronal slices are depicted using a sagittal slice (top of the left column). Standard tissue signal enhancement induced by Mn^{2+} was readily seen within the olfactory bulb, cerebral cortex, hippocampus, and cerebellum [19]. The color-coded average enhancement maps of the control and HIV-1 infected mouse brains are illustrated in the second and third columns of Figure 3.2.a, respectively. The enhancement represented the signal change induced by Mn^{2+} normalized to the MRI signal of pre-Mn^{2+} administration. MEMRI enhancement changes were observed throughout the brain in HIV-1 infected animals compared to controls (Fig. 3.2.a). Statistically significant increases in the MEMRI enhancement are shown by pixels with $p < 0.05$ (the first column in Fig. 3.2.b). These p values are color-coded and overlaid on the averaged MEMRI slices. Using the MEMRI-based mouse brain atlas, 41 brain regions/sub-regions were identified for each humanized mouse. A list of regions on the brain atlas can be found in chapter 4 (Table 4.1). The MEMRI enhancement was compared between each brain region of control and HIV-1 infected mouse. The regions with p values less than 0.05 from such comparisons are shown in the second column in Figure 3.2.b and illustrated with identical color-coding as in the first column. The brain regions with significantly increased signal enhancement ($p < 0.05$) are also included within Table 3.1. Three-dimensional images of brain regions with significant enhancement increase are illustrated in Figure 3.2.c. The brain regions showing trends of enhancement increase are listed in Table 3.2. Morphological and volumetric changes were assessed in virus-

infected animals by the MEMRI mouse brain atlas. Whole brain and regional volumes in the HIV-1 infected mice were comparable to control animals (data not shown). The toxicity of Mn^{2+} was considered. Mice were observed daily after i.p. $MnCl_2$ injections. This included chemical injection linked tremor and lethargy, the clinical signs of Mn^{2+} overdose. No Mn^{2+} induced toxic signs and symptoms were observed during the study.

3.3.4. Immunohistology

Immunohistochemistry was subsequently performed on CA1, CA3 and the dentate gyrus (DG) regions of the hippocampus at study termination, 16 WPI (Fig. 3.1.a). Brain sections were stained for GFAP, Iba-1, cFos (neuronal activation), synaptophysin (SYN, synaptic vesicle protein), and neurofilament (NF, neuronal cytoskeleton protein). Fluorescence intensity for these antigens was expressed as intensity/μm^2. Activated morphologies were observed as defined by increased cell body size and process formations for both astrocytes and microglia in virus-infected animals (Fig. 3.3.a and 3.3.b). The presence of activated astrocytes and microglia are known to be linked to virus-induced inflammation [22,23]. Neuronal activation (cFos expression) was substantially higher in brain regions with gliosis and specifically in the hippocampus; indicating increased neuronal excitation during inflammation (Fig. 3.3.c, Fig. 3.5). Irregularly shaped and decreased SYN expression was seen in the CA3 region of infected animals and reflected synaptic injury (Fig. 3.3.d). Reduction in NF fibers was also observed at CA3 region in infected animals (Fig. 3.3.e). NF and SYN expression demonstrates neuronal injury after glial inflammation. Co-localized MEMRI enhancement in infected animals was compared to controls and confirmed the sensitivity

of the MEMRI in reflecting glial and neuronal histochemical and morphological changes (Fig. 3.3.f).

Quantitative immunohistochemistry was used to compare neuropathology between control and HIV-1 infected mice and its association with MEMRI regional enhancements. In CA1 region, GFAP and Iba-1 expression were significantly higher in infected animals than controls (GFAP, $p = 0.041$; Iba-1, $p = 0.018$); whereas, SYN and NF expression were not different amongst the groups (Fig. 3.4.a). Gliosis with no evidence of neuronal injury in CA1 paralleled significant MEMRI signal enhancement increase in infected animals compared to controls ($p = 0.047$) (Fig. 3.4.a). In the CA3 region, GFAP expression was higher ($p = 0.038$), and SYN and NF expression lower (SYN, $p = 0.027$; NF, $p = 0.005$); whereas, Iba-1 signals were not changed by viral infection (Fig 3.4.b). With a combination of astrocyte responses and neuronal injury, MEMRI signal remained similar between infected and control animals (Fig. 3.4.b). GFAP expression was higher (GFAP, $p = 0.042$) and Iba-1 increased but not significantly (Iba-1, $p = 0.083$) in the DG region of infected animals; whereas SYN and NF signals were not changed (Fig. 3.4.c). MEMRI enhancement in this region was increased in infected animals ($p = 0.045$) (Fig. 3.4.c). The quantitative analyses taken together, demonstrate that activated glia and neurons (increased cFos staining) during inflammation induced the increase in MEMRI signal in the CA1 and DG brain regions. However, the enhancement increase was offset by neuronal injury (reduced SYN and NF) in the CA3 brain region. Microtubule associated protein (MAP2) staining was not changed in the infected animals. Evidence for neuronal apoptosis determined by anti-caspase3 staining was not observed in infected mice (data not shown).

We next investigated if glial activation and MEMRI signal enhancements were correlated one with the other. In the CA1 and DG, correlations between GFAP expression and MEMRI signal increase were seen (CA1, r = 0.86, p = 0.007; DG, r = 0.92, p = 0.001). Linkages between gliosis and MEMRI enhancement demonstrated that Mn^{2+} uptake and accumulation increases in neurons affected by inflammation. This was associated with astrocyte responses and the MEMRI signals [24]. Next we measured relationships between the degree of brain injuries and VL in blood. The average brain MEMRI enhancement alteration was linked, in measure, to the peripheral VL difference of at 16 weeks and maximum values (defined as viral load dynamics; r = 0.714, p = 0.071). This result suggested that the greater the viral load drop during the course of infection, the smaller the MEMRI enhancement change. MEMRI enhancement was not affected by numbers of CD4+ and CD8+ T cells (data not shown).
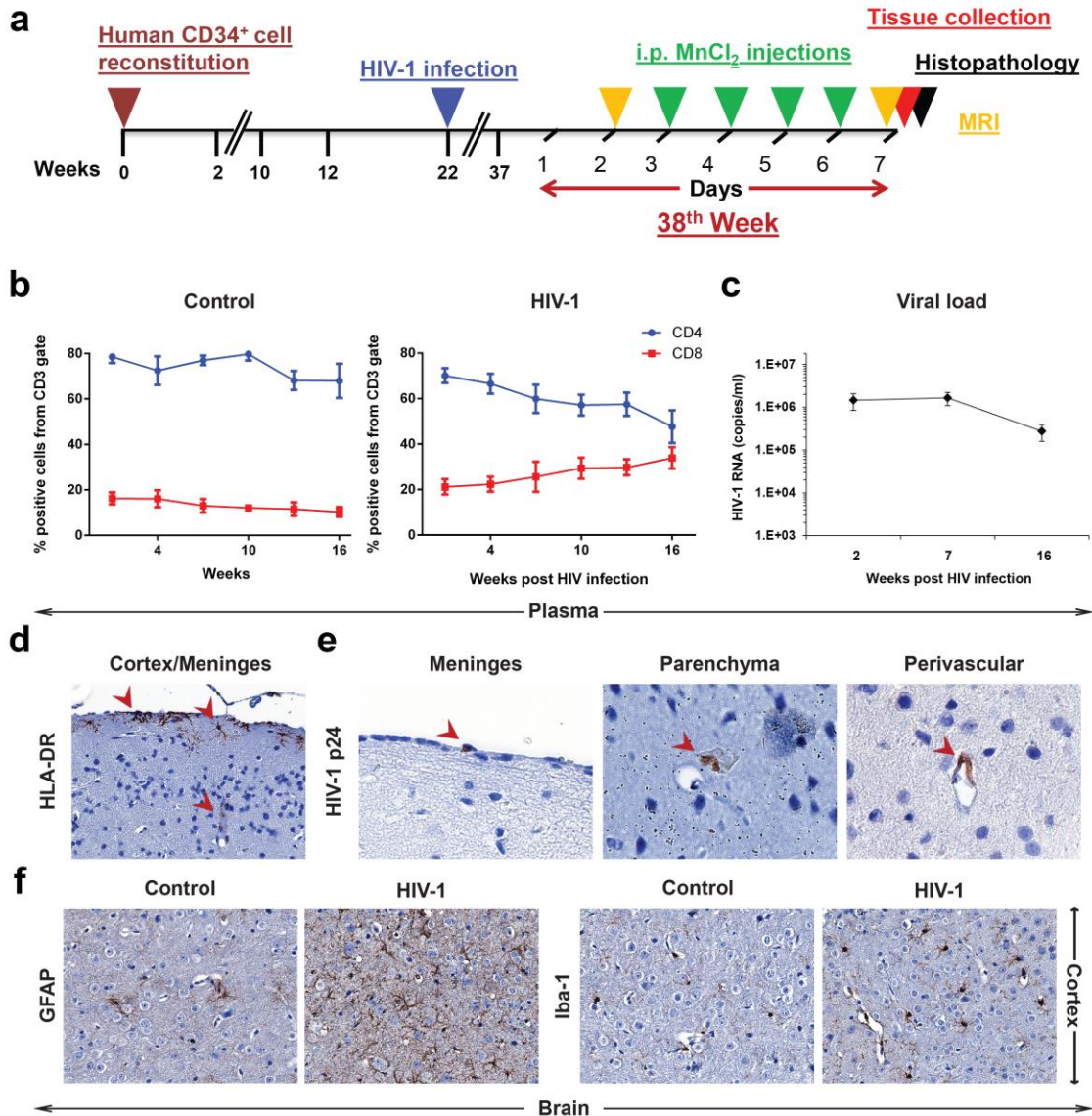
Figure 3.1. (a) The time course of human CD34+ cell reconstitution, HIV-1 infection, MRI, $MnCl_2$ injections and histopathology. **(b)** Results from flow cytometric analyses of human CD4+ and CD8+ cells in peripheral blood of control mice (left) and infected mice (right). **(c)** Average HIV-1 RNAs (copies/ml) in peripheral blood of infected mice (n = 8). **(d and e)** Infiltration of human activated cells detected by HLA-DR (indicated by arrows, left, 20×) and HIV-1+ cells (detected by p24 antigen) in meninges, parenchyma

and perivascular spaces (positive cells indicated by arrows, right, 100×) into the brain of infected mice at 16 WPI. **(f)** Brain sections of control and infected mice stained by GFAP for astrocyte (left, 40×) and by Iba-1 for microglial (right, 40×). Activated glial cell morphologies were seen in infected animals. Data are expressed as mean ± SEM in (B) and (C)

(a)
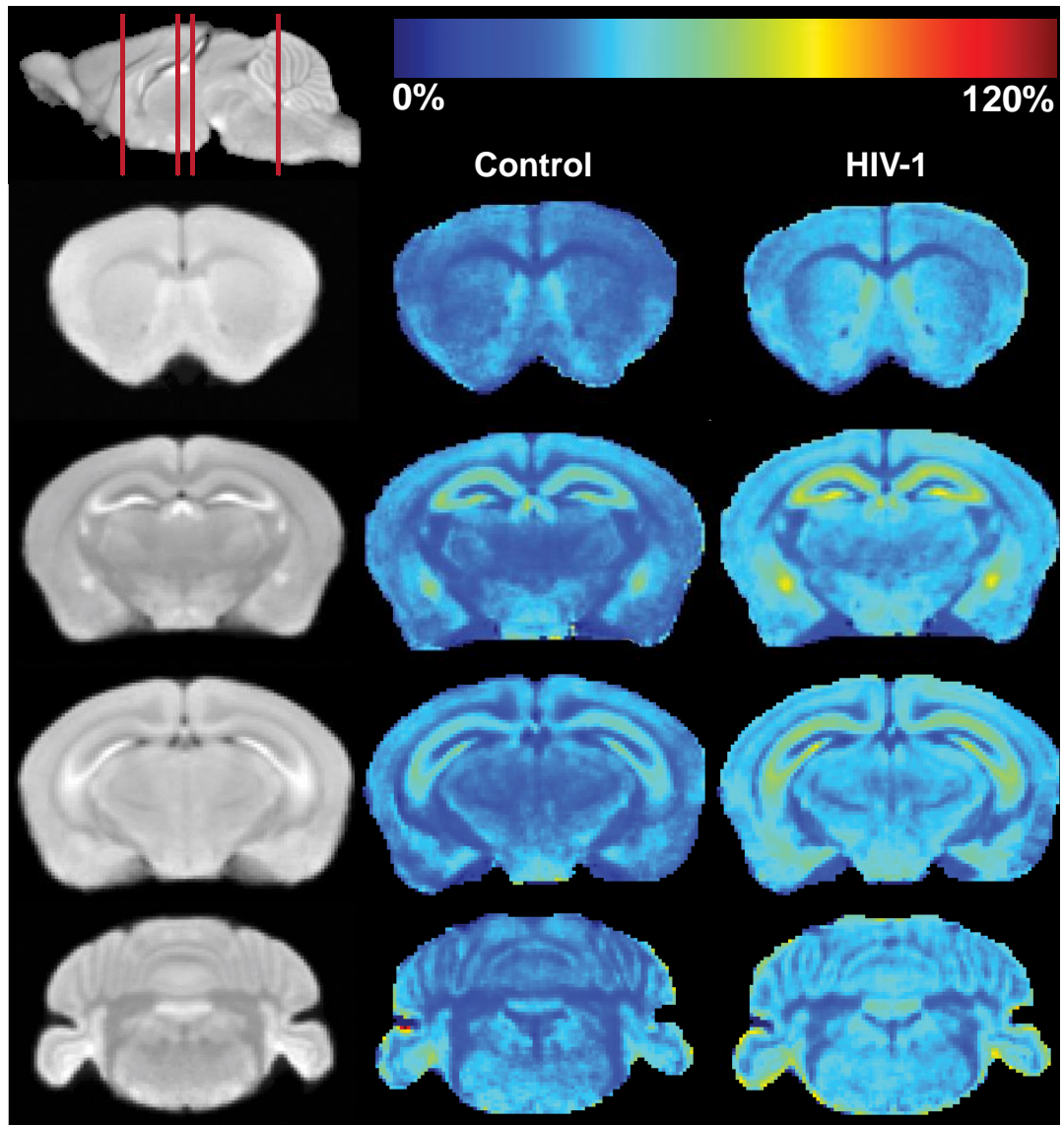
(b)
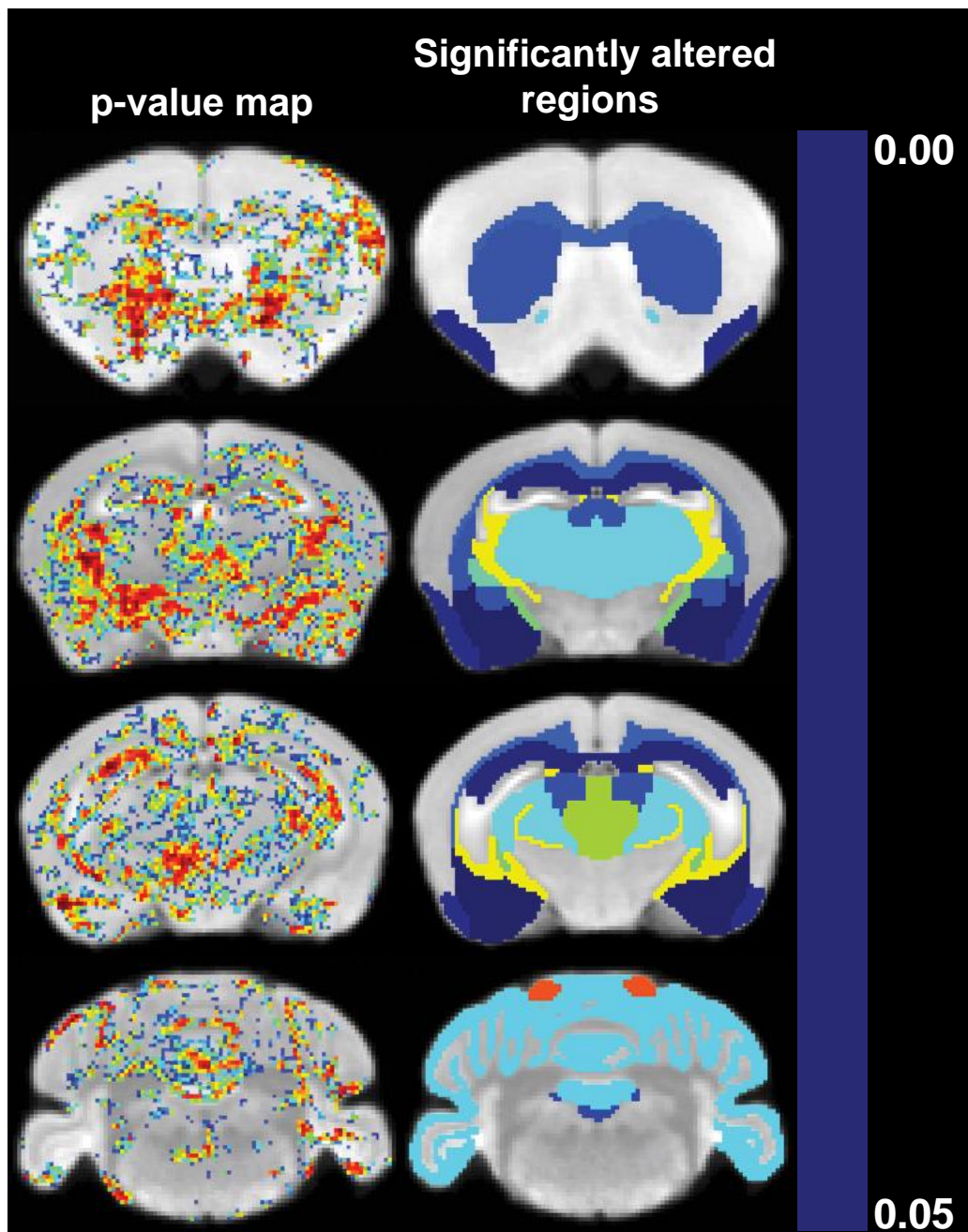
(c)
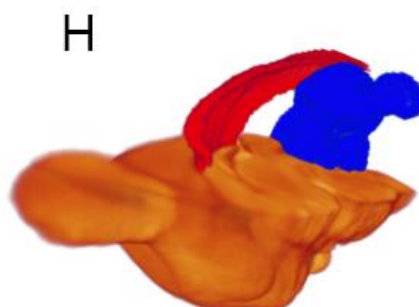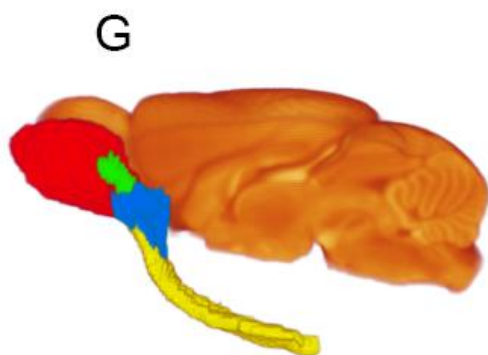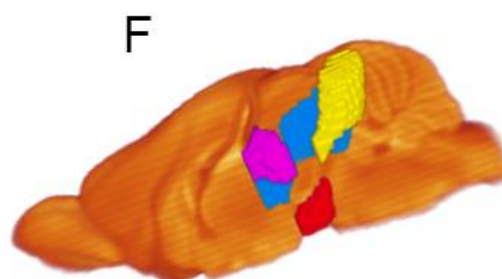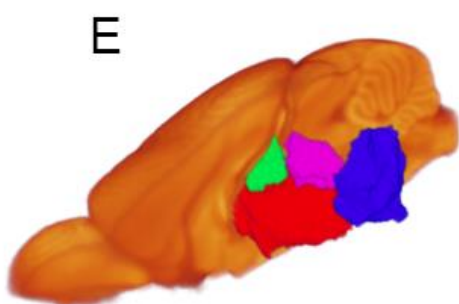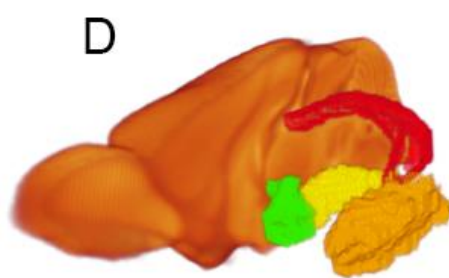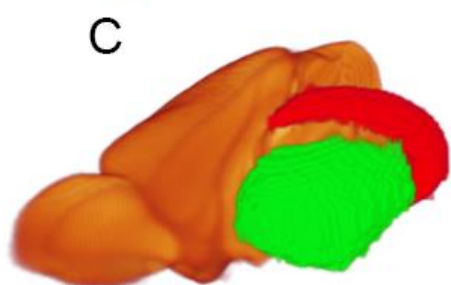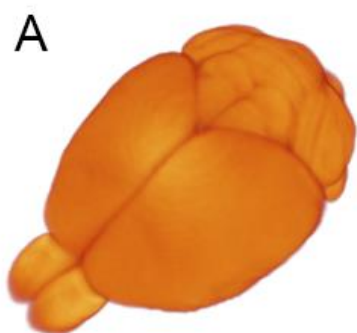
Figure 3.2. Comparison of MEMRI enhancement between HIV-1 infected animals and controls. **(a)** MEMRI enhancement maps. The first column (from left) shows coronal slices of the averaged MEMRI of control mice as an anatomical reference. The sagittal slice (upper left) shows respective coronal positions (red lines). The second column shows the average enhancement in control mice on the coronal slices. The third column represents the average enhancement of HIV-1 infected mice. The color bar for the enhancement maps is at the top of the figure. Dark blue color (0%) means no change in enhancement from Mn^{2+} compared to pre-injection signal intensity. Dark red color represents 120% signal increase compared to pre-injection. Increase in MEMRI enhancement can be seen throughout the brain of infected animals than controls. **(b)** Statistical comparison of MEMRI enhancement between control and HIV-1 infected animals. The left column shows the pixels with significant enhancement difference ($p <$ 0.05) overlaid onto the averaged brain image. The color bar of p values is at the right. Dark blue color represents $p = 0.05$ and dark red color represents the value of 0.00. The right column shows significantly altered brain regions of infected mice using the same color scale. **(c)** Brain regions with significant enhancement changes demonstrated in 3-D. **(1)** Averaged brain image. **(2)** Right hemisphere of the averaged brain. Internal brain regions can be seen on the middle of sagittal section. **(1 and 2)** are to provide anatomical references for the demonstration of regions with significant enhancement changes. **(3)** Sub-cortical regions including CA1_CA3_SUB (red) and CP (green). **(4)** Sub-cortical regions including DG-mo (red), AMY (orange), PALc (green), and GP (yellow). **(5)** Brain stem regions including TH (red), EPI (green), SN (blue) and PRT (purple). **(6)** PAG (blue), IC (yellow), SN (red) and PRT (purple). **(7)** Olfactory regions including

MOB (red), AOB (green), AON (blue) and PIR (yellow). **(8)** cc (red) and CBXmo (blue).

The full names of the brain regions are included in Table 3.1.

Table 3.1. Brain regions that showed significant signal enhancement ($p < 0.05$)

	Brain regions	p
Sub-cortical region	CA1_CA2_SUB	0.047
	DG-mo	0.046
	CP	0.039
	AMY	0.048
	GP	0.028
	PALc	0.047
Brain stem region	TH	0.03
	EPI	0.043
	P	0.044
	PAG	0.022
	IC	0.01
	SN	0.041
	RMB	0.033
	PRT	0.043
Olfactory region	MOBgl	0.021
	AOB	0.012
	PIR	0.046
	AON	0.036
Cerebellar region	CBXmo	0.031
Fiber tracts	cc	0.037

CA1_CA2_SUB: Field CA1 + Field CA2 + Subiculum of Hippocampus Formation, DG-mo: Dentate gyrus_molecular layer, CP: Caudoputamen, AMY: Amygdala, GP: Globus pallidus, PALc: Pallidum caudal region, TH: Thalamus, EPI: Epithalamus, P: Pons, PAG: Periaqueductal gray, IC: Inferior colliculus, SN: Substantia nigra, RMB: Rest of midbrain , PRT: Pretectal region, MOBgl: Main olfactory bulb glomerular layer, AOB: Accessory olfactory bulb, PIR: Olfactory piriform area, AON: Anterior olfactory nucleus, CBXmo: Cerebellar cortex molecular layer, cc: corpus callosum, ($p < 0.05$) (p: t test p value)

Table 3.2. Brain regions that showed trend of signal enhancement increase

$(0.05 <= p < 0.01)$

	Brain regions	p
Isocortex	Isocortex	0.06
Sub-cortical region	STRv	0.065
	LSX	0.053
	MS	0.055
	DG-(po+sg)	0.071
Brain stem region	HY	0.074
	MY	0.051
Cerebellar region	CBXgr	0.053
	CBwm	0.07
	FN	0.071

Isocortex, STRv: Striatum ventral region, LSX: Lateral septal complex, MS: Medial septal nucleus, DG-(po+sg): Dentate gyrus_(polymorph layer + granular layer), HY: Hypothalamus, MY: Medulla, CBXgr: Cerebellar granular layer, CBwm: Cerebellar white matter, FN: Fastigial nucleus
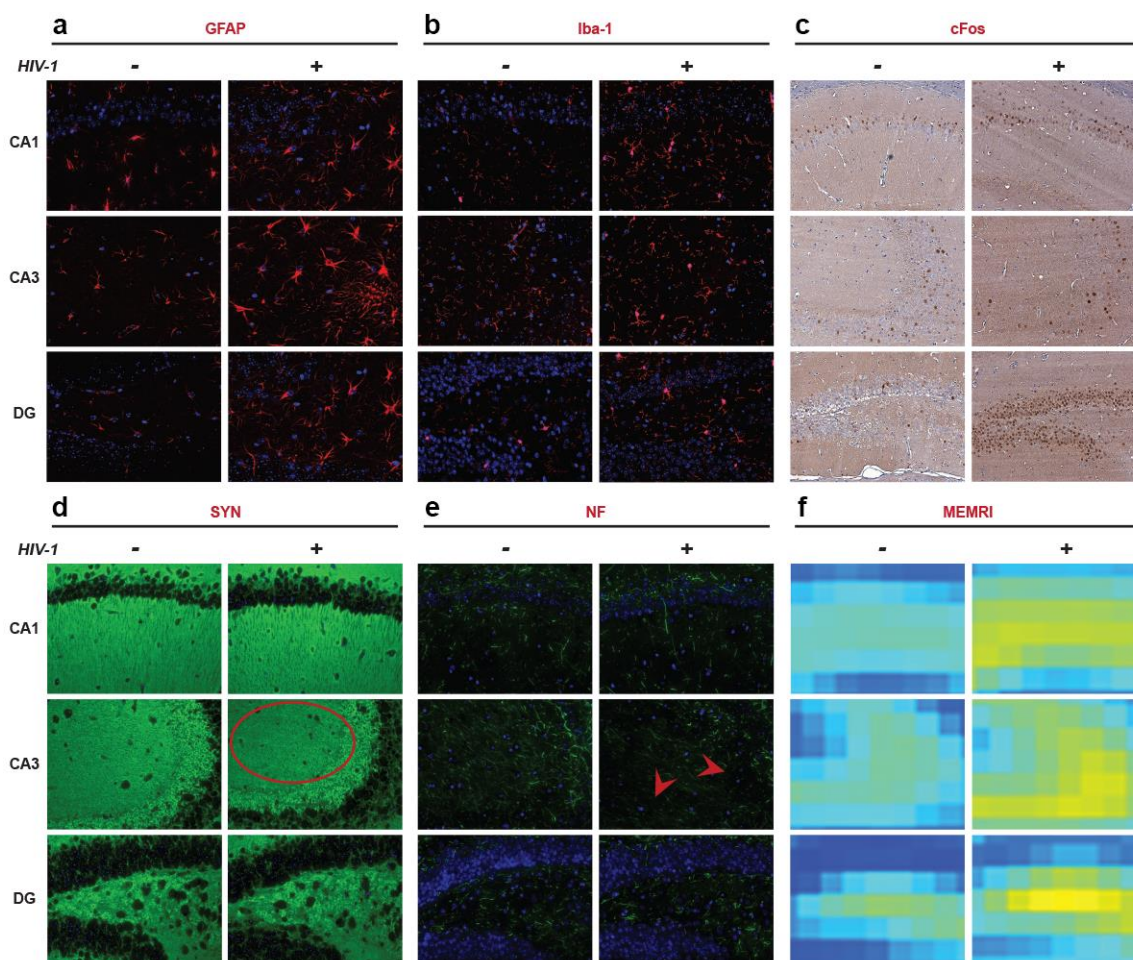
Figure 3.3. Immunohistology of the hippocampus sub-regions including CA1, CA3 and DG (40×). Representative brain sections of control and HIV-1 infected mice stained for GFAP (astrocyte), Iba-1 (microglia), cFos (neuronal activation), SYN (synaptic vesicle protein), NF (neuronal cytoskeleton protein) and co-localized MEMRI slices are presented. **(a, b and c)** Increase in GFAP, Iba-1 and cFos expression was observed in infected animals compared to controls in all three regions of hippocampus. (**d and e**) In CA3 region, SYN and NF expression was decreased (indicated by an oval and arrows, respectively) of infected animals compare to controls, but not in CA1 or DG. (**f**) Altered in MEMRI enhancement in co-localized brain slices was observed in infected animals
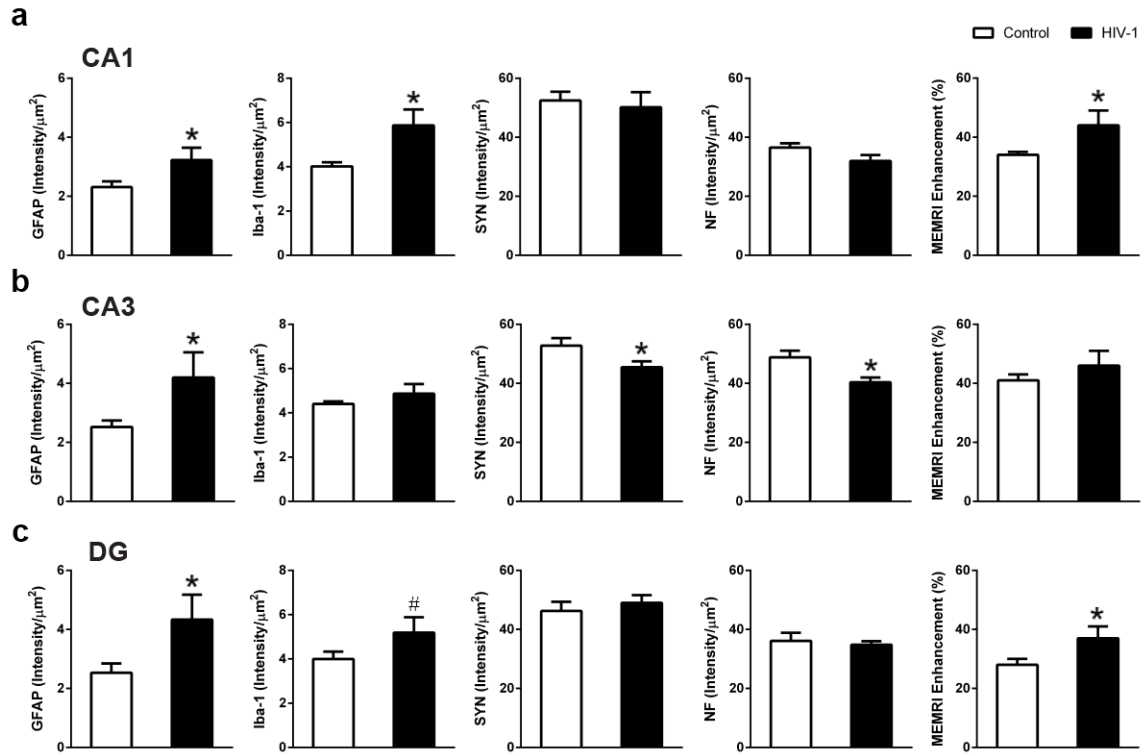
Figure 3.4. Association of immunohistology with MEMRI. **(a)** Quantitative analysis showed significant increase in GFAP, Iba-1, and MEMRI enhancement on CA1 region of HIV-1 infected animals compared to controls. **(b)** CA3 region showed significantly increased GFAP, significantly decreased SYN as well as NF, and no change in MEMRI signal in infected animals compared to controls. **(c)** DG region showed significantly increased GFAP, a trend of increased Iba-1, and significantly increased MEMRI enhancement in infected animals compared to controls. Data are expressed as mean $\pm$ SEM. (*: $p < 0.05$, #: $p < 0.1$)
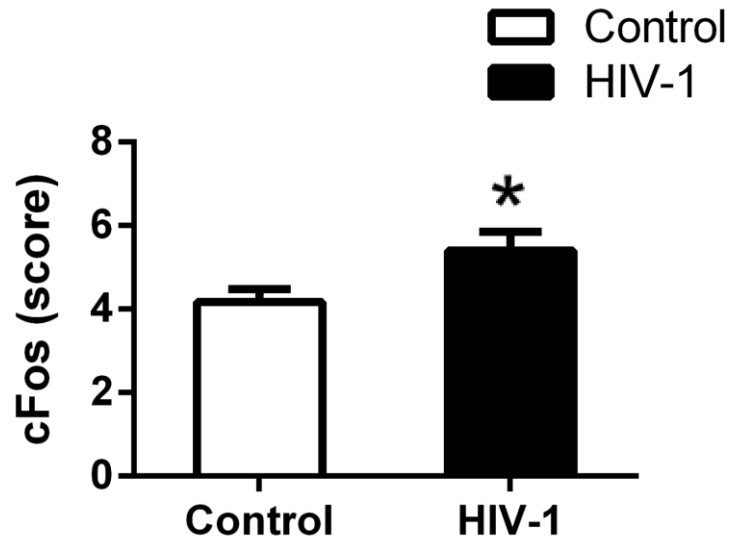
Figure 3.5. cFos expression at hippocampus region. HIV-1 infection caused significant increase in cFos expression compared to control. Data are expressed as mean $\pm$ SEM. (*: $p < 0.05$)

A. Reconstitution

HSC
HPC
Monoblast
Myeloblast
Pro-B cell
B cell
Neutrophil
Monocyte
Dendritic cell
Bone marrow
Humanized mouse

B. Humanized Mouse Brain

Astrocyte
Microglia
Neuron
Human macrophage
Human monocyte
Blood brain barrier

C. HIV-1 ( ) Infected Humanized Mouse Brain

Microglia
Astrocyte

Pro-inflammtory- cytokines, chemokines
HIV-1 proteins (gp120, Tat, Vpr)
iNOS
Quinolic acid
Arachidonic acid
Glutamate

Activated microglia
Injured neuron
Activated astrocyte
Activated Neuron

D. HIV-1 induced neuropathology, Mn^{2+} ( ) accumulation and associated MEMRI signal enhancement

Blood
Choroid plexus
CSF
Ependyma
Activated microglia
Activated astrocyte
Injured neuron
Neuron
Activated neuron

Figure 3.6. The mechanism of MEMRI in the detection of neuropathology in HIV-1 infected humanized mice. **(a)** Human immune system reconstitution (humanization) in NSG mouse. Human CD34+ stem cells (HSC) isolated from umbilical cord blood were injected intrahepatically into one day old irradiated pups. The injected HSC reach mouse lymphoid organs including bone marrow and develop into broad range of cell lineages. A mature human immune system develops in the NOD/scid-IL-2Rγc^{null} (NSG) mice. **(b)** Humanized mouse brain. Human cells (macrophages, yellow color) are majorly observed at meninges and perivascular spaces in humanized mouse brain. Mouse cells (resting glia and neurons) are showed in green colors. **(c)** HIV-1 infected humanized mouse brain. Infected human macrophages carry HIV-1 (green) into the brain and release pro-inflammatory cytokines, chemokines viral proteins, that leads to activated glia (red) followed by neuronal excitation (blue) and injury (gray). **(d)** HIV-1 induced neuropathology, Mn^{2+} accumulation and associated MEMRI signal enhancement. Mn^{2+} (blue and pink circle) enters brain through choroid plexus. Being Ca^{2+} analog, it enters neurons through voltage gated Ca^{2+} channels. Mn^{2+} is transported anterogradely by microtubule assembly. Once Mn^{2+} is released, it is taken up by post-synaptic neurons. Mn^{2+} accumulation increases in activated neurons during inflammation resulting in MEMRI signal enhancement increase (stronger purple outer glow compared to control). Whereas, Mn^{2+} uptake and transportation are reduced in injured neurons and thus MEMRI signal is suppressed

3.4. Discussion

Humanized mouse model (NSG/CD34+) of HIV/AIDS can, in part, mirror human HIV-1 associated neuropathology [8,9,13] and was used successfully to test ART efficacy [25]. Peripheral VL and human CD4+ T-cell decline are hallmarks of HIV-1 infection in humans which are reflected in these humanized mice. Moreover, a metabolic encephalopathy caused by viral infection resulting in micro- and astro- gliosis, myelin pallor, excitotoxicity and neuronal injury is also seen in both humans and infected mice [8,9,13,22]. Such spectrums of pathologies make the humanized mice a relevant model for study. In the present study, altered MEMRI brain signal is seen in HIV-1 infected mice that serve to assess the complexities of neuropathology that underlie HAND's clinical manifestations. Although, MEMRI was used previously to study a range of neurodegenerative disease models [26-29], this is the first report of its use to study effect of HIV-1 on humanized mice brain function and anatomy with improved analytical method.

MEMRI enhancement for HIV-1 infection is linked to reactive astrocytes and activated neurons. The cellular basis of the enhancement change was investigated in a previous study and interpreted as elevated neuronal Mn^{2+} uptake and accumulation stimulated by astrocyte activation [24]. The associations between MEMRI signal with reactive astrocytes and neuronal responses was previously observed [24,29,30]. We previously showed that activated glia do not accumulate excessive Mn^{2+} but stimulate neuronal Mn^{2+} uptake [24]. Thus, MEMRI can be used to monitor virus-associated neuronal excitotoxicity that occurs as a consequence of neuroinflammation. In the CA3 region, both inflammation and neuronal injury (synaptic and axonal injury) were

operative in the infected animals. This is consistent with the fact that neuronal damage caused by HIV-1 infection begins with synaptic damage, compromised dendrite arbor, then neuronal death occurs as a consequence of persistent infection and immune deterioration [31]. Interestingly, in CA3 region, we did not observe MEMRI signal increase as in CA1 and DG. Indeed, damaged neurons likely influence reduction in neuronal Mn^{2+} accumulation. The voxel size of MEMRI was 100 μm^3, which contains a large number of cells. The MEMRI enhancement of each voxel resulted from the combining effects of activated and injured neurons. Simply, the MEMRI signal enhancement induced by activated neurons was likely offset by signal decrease in injured cells. Increasing spatial resolution can partially solve the problem as excited and injured neurons may be differentiated. Additionally, performing MEMRI and immunohistological analysis at multiple time points after the infection may also establish accurate associations between signal enhancements and neuronal injury.

The cellular mechanisms underlying MEMRI enhancement is summarized in Figure 3.6. Humanized mice permanently carry human blood cells, and these populate brain primarily at meninges and perivascular spaces. After HIV-1 infection, infected human monocyte-macrophages carry HIV-1 into the brain and release pro-inflammatory cytokines, chemokines, viral proteins. This leads to activation of murine glia followed by neuronal excitotoxicity and injury, which in turn reflects the brain injuries seen as a consequence of chronic HIV-1 infection. Systemically administrated Mn^{2+} enters the brain through choroid plexus. As a Ca^{2+} analog, it enters neurons through voltage gated Ca^{2+} channels and is transported anterogradely by microtubule assembly. Once Mn^{2+} is released, it is taken up by post-synaptic neurons. Reactive astrocytes that arise as a

consequence of HIV-1 induced neuroinflammation first cause elevated neuronal Mn^{2+} uptake resulting in increased MEMRI signal enhancement. Neuroinflammation then results in neuronal injury with consequently suppressed MEMRI signal.

In our parallel works, behavioral tests were used to show memory loss and cognitive dysfunction in these infected mice [13]. As the hippocampus plays an important role in memory and cognition, the glial activation and neuronal injury in this brain region detected in this study may contribute to such behavioral abnormalities. Aside from the hippocampus, the brain regions that show MEMRI signal enhancement following HIV-1 infection include sub-regions of the olfactory system, sub-cortical, brain stem and cerebellar regions. These findings suggest that infected mice can suffer motor and autonomic nervous system dysfunction because of cerebellar and brain stem damage. As different parts of the brain have variable vulnerabilities to HIV-1 infection [32,33], the current study provides a unique opportunity for unbiased mapping of region specific neuropathology.

The MEMRI results are supported by the DTI measures in our parallel study [13]. This study showed altered DTI parameters on hippocampal regions in HIV infected humanized mice, and association between the DTI parameters and quantitative histology. In infected human and nonhuman primates, abnormal DTI was found in the frontal and parietal white matter, putamen, and corpus callosum indicating neuroinflammation and axonal/myelin injury [34,35]. In parallel, inflammation metabolic abnormalities were detected by MRS in the basal ganglia, cerebrum, caudate, thalamus, and hippocampus [34-36]. We acknowledge that a direct comparison of the brain imaging findings in humans and nonhuman primates with mice is difficult due to differences in anatomy,

physiology, and neurochemistry. Our results are consistent with these human and non-human primate studies.

It is likely that abnormalities seen in these animals were not primarily a result of active viral replication in nervous system, but largely a consequence of replication in blood and peripheral lymphoid organs. Until now, studies have shown that peripheral blood nadir CD4+ T-cells count and viral DNA are systemic predictors of HIV-1 induced neurocognitive disorders [3,37,38]. However, we did see a trend towards correlation between MEMRI signal enhancement alteration and a plasma viral load measure, which is the difference between the maximum value and at 16 WPI. A parallel study found that viral levels correlated with cortical lactate [13]. The same study also found the correlation or the trend of correlation between cortical and dentate gyrus DTI parameters and viral load. Their study along with ours suggested that peripheral viral load might be associated with the neuropathology reflected by imaging in HIV-1 infected humanized mice. Such a sensitivity of the brain to peripheral events in these animals indicates a dynamic pathogenic process; where HIV-1 infected blood cells enter into the brain and cause disease [39].

We now demonstrate that MEMRI is a sensitive biomarker of HIV-1-induced neuropathology. However, when inflammation and neuronal impairment occur simultaneously, both increase and decrease in MEMRI signal can be observed. In order to improve the specificity of imaging on neuropathology, it is reasonable to combine MEMRI with other imaging modalities. For example, another study showed that the cerebral cortex is a primary region of damage in infected mice as demonstrated by MRS and DTI [13]. Combining MEMRI with MRS and DTI can positively determine

neuroinflammation (increased MEMRI enhancement and increase in myoinositol), and may help to detect neuronal impairment (reduced MEMRI enhancement, loss of N-acetylaspartate and creatine, reduced diffusivity, and fractional anisotropy). This package of imaging modalities will greatly enhance our ability for non-invasive assessment of HIV-1 induced neuropathology. In addition to assessment of neuronal Mn^{2+} uptake, MEMRI can provide precise anatomical details. To this end, we applied a MEMRI-based NSG mouse brain atlas to assess brain morphology to reveal abnormalities associated with HIV-1 infection in an animal study. As we expected, we did not find changes in total brain and sub-structural volumes with altered MEMRI enhancement. This suggests that neuronal death is limited in infected animals. MEMRI successfully provided both insights into neuronal function and the measurements of brain anatomy.

The toxicity of Mn^{2+} was minimized by a carefully designed $MnCl_2$ administration. We have used a fractionated administration scheme first proposed by [40]. In this scheme, $MnCl_2$ solution was injected daily through i.p. with a small dose for certain days (usually 4-8 days), 4 days for our study. Mice were observed daily after the injection and we did not observe any Mn^{2+} induced toxic clinical signs and symptoms. *In toto*, we demonstrate that MEMRI can be developed as a biomarker of virus-associated neuropathology. With a thorough understanding of the relationships between MEMRI and neuropathology, monitoring the efficacy of brain therapeutics can be realized for prevention or reversal of virus-associated brain disease.

3.5. References

1. Robertson K. and Yosief S., (2014) Neurocognitive assessment in the diagnosis of HIV-associated neurocognitive disorders. Semin. Neurol. 34, 21-26.

2. Antinori A., Arendt G., Becker J. T., Brew B. J., Byrd D. A., Cherner M., Clifford D. B., Cinque P., Epstein L. G., Goodkin K., Gisslen M., Grant I., Heaton R. K., Joseph J., Marder K., Marra C. M., McArthur J. C., Nunn M., Price R. W., Pulliam L., Robertson K. R., Sacktor N., Valcour V. and Wojna V. E., (2007) Updated research nosology for HIV-associated neurocognitive disorders. Neurology. 69, 1789-1799.

3. Heaton R. K., Clifford D. B., Franklin D. R.,Jr, Woods S. P., Ake C., Vaida F., Ellis R. J., Letendre S. L., Marcotte T. D., Atkinson J. H., Rivera-Mindt M., Vigil O. R., Taylor M. J., Collier A. C., Marra C. M., Gelman B. B., McArthur J. C., Morgello S., Simpson D. M., McCutchan J. A., Abramson I., Gamst A., Fennema-Notestine C., Jernigan T. L., Wong J., Grant I. and CHARTER Group., (2010) HIV-associated neurocognitive disorders persist in the era of potent antiretroviral therapy: CHARTER Study. Neurology. 75, 2087-2096.

4. Clifford D. B. and Ances B. M., (2013) HIV-associated neurocognitive disorder. Lancet Infect. Dis. 13, 976-986.

5. McArthur J. C., Steiner J., Sacktor N. and Nath A., (2010) Human immunodeficiency virus-associated neurocognitive disorders: Mind the gap. Ann. Neurol. 67, 699-714.

6. Gill A. J. and Kolson D. L., (2014) Chronic Inflammation and the Role for Cofactors (Hepatitis C, Drug Abuse, Antiretroviral Drug Toxicity, Aging) in HAND Persistence. Curr. HIV/AIDS Rep.

7. Gorantla S., Poluektova L. and Gendelman H. E., (2012) Rodent models for HIV-associated neurocognitive disorders. Trends Neurosci. 35, 197-208.

8. Dash P. K., Gorantla S., Gendelman H. E., Knibbe J., Casale G. P., Makarov E., Epstein A. A., Gelbard H. A., Boska M. D. and Poluektova L. Y., (2011) Loss of neuronal integrity during progressive HIV-1 infection of humanized mice. J. Neurosci. 31, 3148-3157.

9. Gorantla S., Makarov E., Finke-Dwyer J., Castanedo A., Holguin A., Gebhart C. L., Gendelman H. E. and Poluektova L., (2010) Links between progressive HIV-1 infection of humanized mice and viral neuropathogenesis. Am. J. Pathol. 177, 2938-2949.

10. Gorantla S., Makarov E., Finke-Dwyer J., Gebhart C. L., Domm W., Dewhurst S., Gendelman H. E. and Poluektova L. Y., (2010) CD8+ cell depletion accelerates HIV-1 immunopathology in humanized mice. J. Immunol. 184, 7082-7091.

11. Gorantla S., Sneller H., Walters L., Sharp J. G., Pirruccello S. J., West J. T., Wood C., Dewhurst S., Gendelman H. E. and Poluektova L., (2007) Human immunodeficiency virus type 1 pathobiology studied in humanized BALB/c-Rag2-/-gammac-/- mice. J. Virol. 81, 2700-2712.

12. Gorantla S., Gendelman H. E. and Poluektova L. Y., (2012) Can humanized mice reflect the complex pathobiology of HIV-associated neurocognitive disorders?. J. Neuroimmune Pharmacol. 7, 352-362.

13. Boska M. D., Dash P. K., Knibbe J., Epstein A. A., Akhter S. P., Fields N., High R., Makarov E., Bonasera S., Gelbard H. A., Poluektova L. Y., Gendelman H. E. and Gorantla S., (2014) Associations between brain microstructures, metabolites, and cognitive deficits during chronic HIV-1 infection of humanized mice. Mol. Neurodegener. 9, 58.

14. Inoue T., Majid T. and Pautler R. G., (2011) Manganese enhanced MRI (MEMRI): neurophysiological applications. Rev. Neurosci. 22, 675-694.

15. Pautler R. G. and Koretsky A. P., (2002) Tracing odor-induced activation in the olfactory bulbs of mice using manganese-enhanced magnetic resonance imaging. Neuroimage. 16, 441-448.

16. Henriksson J., Tallkvist J. and Tjalve H., (1999) Transport of manganese via the olfactory pathway in rats: dosage dependency of the uptake and subcellular distribution of the metal in the olfactory epithelium and the brain. Toxicol. Appl. Pharmacol. 156, 119-128.

17. Mendonca-Dias M. H., Gaggelli E. and Lauterbur P. C., (1983) Paramagnetic contrast agents in nuclear magnetic resonance medical imaging. Semin. Nucl. Med. 13, 364-376.

18. Geraldes C. F., Sherry A. D., Brown R. D.,3rd and Koenig S. H., (1986) Magnetic field dependence of solvent proton relaxation rates induced by Gd3+ and Mn2+ complexes of various polyaza macrocyclic ligands: implications for NMR imaging. Magn. Reson. Med. 3, 242-250.

19. Silva A. C. and Bock N. A., (2008) Manganese-enhanced MRI: an exceptional tool in translational neuroimaging. Schizophr. Bull. 34, 595-604.

20. Sled J. G., Zijdenbos A. P. and Evans A. C., (1998) A nonparametric method for automatic correction of intensity nonuniformity in MRI data. IEEE Trans. Med. Imaging. 17, 87-97.

21. Uberti M. G., Boska M. D. and Liu Y., (2009) A semi-automatic image segmentation method for extraction of brain volume from in vivo mouse head magnetic resonance imaging using Constraint Level Sets. J. Neurosci. Methods. 179, 338-344.

22. Gonzalez-Scarano F. and Martin-Garcia J., (2005) The neuropathogenesis of AIDS. Nat. Rev. Immunol. 5, 69-81.

23. Tavazzi E., Morrison D., Sullivan P., Morgello S. and Fischer T., (2014) Brain Inflammation is a Common Feature of HIV-Infected Patients Without HIV Encephalitis or Productive Brain Infection. Curr. HIV. Res.

24. Bade A. N., Zhou B., Epstein A. A., Gorantla S., Poluektova L. Y., Luo J., Gendelman H. E., Boska M. D. and Liu Y., (2013) Improved visualization of neuronal

injury following glial activation by manganese enhanced MRI. J. Neuroimmune Pharmacol. 8, 1027-1036.

25. Dash P. K., Gendelman H. E., Roy U., Balkundi S., Alnouti Y., Mosley R. L., Gelbard H. A., McMillan J., Gorantla S. and Poluektova L. Y., (2012) Long-acting nanoformulated antiretroviral therapy elicits potent antiretroviral and neuroprotective responses in HIV-1-infected humanized mice. AIDS. 26, 2135-2144.

26. Morken T. S., Wideroe M., Vogt C., Lydersen S., Havnes M., Skranes J., Goa P. E. and Brubakk A. M., (2013) Longitudinal diffusion tensor and manganese-enhanced MRI detect delayed cerebral gray and white matter injury after hypoxia-ischemia and hyperoxia. Pediatr. Res. 73, 171-179.

27. Soria G., Aguilar E., Tudela R., Mullol J., Planas A. M. and Marin C., (2011) In vivo magnetic resonance imaging characterization of bilateral structural changes in experimental Parkinson's disease: a T2 relaxometry study combined with longitudinal diffusion tensor imaging and manganese-enhanced magnetic resonance imaging in the 6-hydroxydopamine rat model. Eur. J. Neurosci. 33, 1551-1560.

28. Smith K. D., Paylor R. and Pautler R. G., (2011) R-flurbiprofen improves axonal transport in the Tg2576 mouse model of Alzheimer's disease as determined by MEMRI. Magn. Reson. Med. 65, 1423-1429.

29. Hsu Y. H., Lee W. T. and Chang C., (2007) Multiparametric MRI evaluation of kainic acid-induced neuronal activation in rat hippocampus. Brain. 130, 3124-3134.

30. Aoki I., Naruse S. and Tanaka C., (2004) Manganese-enhanced magnetic resonance imaging (MEMRI) of brain activity and applications to early detection of brain ischemia. NMR Biomed. 17, 569-580.

31. Ellis R., Langford D. and Masliah E., (2007) HIV and antiretroviral therapy in the brain: neuronal injury and repair. Nat. Rev. Neurosci. 8, 33-44.

32. Moore D. J., Masliah E., Rippeth J. D., Gonzalez R., Carey C. L., Cherner M., Ellis R. J., Achim C. L., Marcotte T. D., Heaton R. K., Grant I. and HNRC Group., (2006) Cortical and subcortical neurodegeneration is associated with HIV neurocognitive impairment. AIDS. 20, 879-887.

33. Yiannoutsos C. T., Ernst T., Chang L., Lee P. L., Richards T., Marra C. M., Meyerhoff D. J., Jarvik J. G., Kolson D., Schifitto G., Ellis R. J., Swindells S., Simpson D. M., Miller E. N., Gonzalez R. G. and Navia B. A., (2004) Regional patterns of brain metabolites in AIDS dementia complex. Neuroimage. 23, 928-935.

34. Masters M. C. and Ances B. M., (2014) Role of neuroimaging in HIV-associated neurocognitive disorders. Semin. Neurol. 34, 89-102.

35. Holt J. L., Kraft-Terry S. D. and Chang L., (2012) Neuroimaging studies of the aging HIV-1-infected brain. J. Neurovirol. 18, 291-302.

36. Ratai E. M., Pilkenton S. J., Greco J. B., Lentz M. R., Bombardier J. P., Turk K. W., He J., Joo C. G., Lee V., Westmoreland S., Halpern E., Lackner A. A. and Gonzalez R. G., (2009) In vivo proton magnetic resonance spectroscopy reveals region specific

metabolic responses to SIV infection in the macaque brain. BMC Neurosci. 10, 63-2202-10-63.

37. Munoz-Moreno J. A., Fumaz C. R., Ferrer M. J., Prats A., Negredo E., Garolera M., Perez-Alvarez N., Molto J., Gomez G. and Clotet B., (2008) Nadir CD4 cell count predicts neurocognitive impairment in HIV-infected patients. AIDS Res. Hum. Retroviruses. 24, 1301-1307.

38. Kallianpur K. J., Shikuma C., Kirk G. R., Shiramizu B., Valcour V., Chow D., Souza S., Nakamoto B. and Sailasuta N., (2013) Peripheral blood HIV DNA is associated with atrophy of cerebellar and subcortical gray matter. Neurology. 80, 1792-1799.

39. Burdo T. H., Lackner A. and Williams K. C., (2013) Monocyte/macrophages and their role in HIV neuropathogenesis. Immunol. Rev. 254, 102-113.

40. Grunecker B., Kaltwasser S. F., Peterse Y., Samann P. G., Schmidt M. V., Wotjak C. T. and Czisch M., (2010) Fractionated manganese injections: effects on MRI contrast enhancement and physiological measures in C57BL/6 mice. NMR Biomed. 23, 913-921.

CHAPTER - 4

Generation of a Manganese-Enhanced Magnetic Resonance Imaging (MEMRI)-based NOD/scid-IL-2Rγ_c^{null} Mouse Brain Atlas

4.1. Introduction

Advancements in genetic engineering enabled wide spread use of transgenic mice for biomedical research. These mice are extensively used in studies of cell, tissue and organism growth, differentiation and disease. Immune deficiency induced by affecting the integrity of the adaptive immune system in NOD/scid-IL-2Rγ_c^{null} (NSG) mice permitted the efficient and sustained engraftment of human immunocytes in mice [1,2]. As a result, these mice are used for studies of a broad range of human diseases covering the disciplines of oncology, hematology, infectious disease and regenerative medicine. In particular, our laboratories and others have pursued investigation of human immunodeficiency virus type one (HIV-1) pathobiology including the studies of viral reservoirs and direct tissue injuries including the lung and the central nervous system (CNS) [3-5].

Apropos to studies of end organ diseases associated with HIV-1 infection, magnetic resonance imaging (MRI) has provided critical insights into the mechanisms of virus-induced damage as well as repair following antiretroviral therapy (ART). We posit that such investigations can be substantively improved if specific mouse atlases are generated. Such an atlas could permit broad longitudinal investigation of brain morphology under conditions that mimic aspects of human neurologic disease. Specifically, brain parcellation can automate analyses of structure-wise MRI based metrics (e.g., T_1 and T_2 relaxation times, diffusion tensor imaging (DTI) measures, metabolites concentrations, pharmacokinetics and pharmacodynamics (PK and PD), and

drug biodistribution of magnetically labeled cells and nanomaterials). These works would serve to complement and extend analyses of morphological aberrations seen during progressive infection. Such measures could also be harnessed as biomarkers of disease as well as to determine drug efficacy.

Mouse brain atlases were developed by others [6-13]. Such works were heralded through the need to integrate gene expression with neuroanatomical data and now available as an online public resource [14]. Indeed, recent studies have focused on generating developmental and functional brain atlases [11]. The realization of multi-dimensional (multi-modality and/or multi-parametric) data is notable [10,15].

Acquisition of high resolution data with high signal-to-noise ratios (SNR) involves long MRI scanning times that are difficult in a live mouse. To overcome such difficulties, most researchers have performed *ex vivo* imaging on brain-in-skull or fixed brains and created mouse brain atlases. However, tissue deformations that are common and are linked to the type and duration of brain preparation and fixation methods may affect the atlases generated. Thus, *in vivo* MRI data based atlases can help improving accuracy of brain atlases constructed and can be used for longitudinal analyses of individual mice. *In vivo* atlases on C57BL/6J mouse brain were generated before by others [16,17]. We wished to take this idea a step further in sensitivity through the use of manganese enhanced MRI (MEMRI). Administration of $MnCl_2$ shortens T_1 relaxation times in most brain structures, improving signal to noise per unit time and providing excellent contrast between many brain substructures including hippocampus, olfactory bulbs, cerebellum, and cerebral cortical layers as noticed in the present study and previous studies [18,19]. This allows T_1-weighted brain MRI at high field strength to be

used to acquire high resolution *in vivo* images while providing enhanced contrast for brain structure identifications. As high-resolution 3D MRI show significant neuroanatomical differences between mouse strains [20], generation of a brain atlas on the same genetic background as used for a disease model serves to enhance accuracy of brain tissue segmentation on MRI. To these ends, the current study developed a 3D *in vivo* MEMRI atlas of NSG mouse.

4.2. Materials and methods

4.2.1. Experimental animals

Nineteen NSG mice (male, weight = 28.5 ± 2.4 grams, age ~ 1 year) from a University of Nebraska Medical Center (UNMC) breeding colony were used in study. Animals were maintained in sterile microisolator cages under pathogen-free conditions in accordance with ethical for care of laboratory animals at UNMC set forth by the National Institutes of Health. All procedures were approved by the University's Institutional Animal Care and Use Committee. Seven human CD34$^+$ hematopoietic stem cells (HSC) reconstituted (humanized) NSG mice (male, weight = 22.1 ± 5.3 grams, age ~ 1 year) were scanned using MEMRI to study brain morphology. Additional 6 NSG mice (male, weight = 30.6 ± 2.9 grams, age ~ 1.5 years) were included in the study for whole brain T_2-weighted MRI data acquisition without $MnCl_2$ administration.

4.2.2. Human CD34+ HSC reconstitution (humanization) of NSG mice

CD34-NSG mice were generated as described in [5]. Human CD34$^+$ HSC were obtained from cord blood (Department of Gynecology and Obstetrics, UNMC) and enriched to

high purity by magnetic bead selection (Miltenyi Biotech Inc., Auburn, CA). The purity of $CD34^+$ cells was >90% by flow cytometry. Cells were transplanted into newborn mice irradiated at 1Gy using a C9 cobalt 60 source (Picker Corporation). $CD34^+$ cells were injected intrahepatically at 10^5 cells/mouse in 20 µl of PBS using a 30 gauge needle. The levels of engraftment and number of human cells in peripheral blood were analyzed by flow cytometry (Dash et al., 2011).

4.2.3. MnCl$_2$ administration

$MnCl_2.4H_2O$ (Sigma-Aldrich, St Louis, MO) was added to saline (0.9% w/v of NaCl solution) to make 120 mM $MnCl_2$ solution. $MnCl_2$ was administered at a dose of 125 mg/kg bodyweight using intravenous (i.v.) injections through the tail vein. $MnCl_2$ was injected using a syringe pump (Harvard Apparatus, MA) at the rate of 125 µL/hour. The dosing scheme was designed based on our experience in MEMRI and several previous studies [19,21-24]. Mice were placed on an electrically heated tail vein injection platform (Braintree Scientific, MA), and were anesthetized by inhalation of isoflurane in 100% oxygen. Breathing rate, cardiac rate and blood oxygen saturation were continuously monitored. Anesthesia level was varied from 0.3% to 1.5% isoflurane to maintain the breathing rate between 40-100 breaths per minute. Immediately after the injection, the mouse was placed on a heating pad in the cage, and its behavior was observed up to four hours to detect the side effects of $MnCl_2$. The animal was then returned to the animal facility and scanned 24 hours later.

4.2.4. MRI data acquisition

MRI of the 19 NSG mice used for atlas generation were scanned 24 hours after $MnCl_2$ administration on Bruker Biospec 70/20 (Bruker, Billerica, MA) operating Paravision 4.0 with a custom-built 18 mm birdcage volume coil. The humanized mice that were used to study the effect of humanization on brain volume were scanned using the same MRI scanner operating Paravision 5.1. An 82 mm actively decoupled volume resonator was used for signal transmission and a four-channel phase array coil was used for reception.

Mice were anesthetized by inhalation of isoflurane in 100% oxygen and maintained 40-80 breaths/minute. Three-dimensional T_1-weighted data were acquired using a Rapid Acquisition with Relaxation Enhancement (RARE) sequence with the following parameters: Repetition time (TR) = 400 ms, Effective echo time (TE_{eff}) = 7.2 ms, RARE factor = 4, number of averages = 1, image matrix = $176 \times 128 \times 128$ with 100 μm isotropic pixel size, total scan time = 27 min, anterior-posterior as the readout direction. MRI data were acquired from both normal and humanized mice. Three-dimensional T_2-weighted MRI were obtained from six NSG mice without $MnCl_2$ administration using the same scanning parameters as for 3D T_1-weighted data except: TR/TE_{eff} = 1500/36 ms, RARE factor = 8, number of averages = 1, total scan time = 1h 55m.

4.2.5. Population averaged MRI mouse brain

All MR brain images were manually brain extracted by separating brain from extracranial tissue using Analyze 10.0v software (www.analyzedirect.com). All brains were registered to median size brain in the group using rigid image registration. Population average brain was created by averaging all registered individual brain images. Then all individual brain

images were iteratively (3 times) affine registered to population average brain and average was updated at each iteration [6]. Finally, nonlinear registration of individual brain images to the average was performed using Large Deformation Diffeomorphic Metric Mapping (LDDMM) to align differences. To minimize the interpolation errors, transformation matrices from individual registrations were combined and applied in one step to each original MRI to generate the final average. All the registration procedures were performed using Diffeomap 1.6v as implemented in DTIStudio software (www.mristudio.org). The final step was to sharpen the boundaries between anatomic features (enhanced brain) by applying the Laplacian as:

$$g(x, y) = f(x, y) - \nabla^2 f(x, y)$$

where g(x, y) and f(x, y) represent enhanced and input images respectively, and ∇^2 represents the Laplacian operator.

4.2.6. Structures delineation and labeling

Paxinos atlas (Paxinos and Franklin, 2001) and Allen brain digital atlas [14] (http://mouse.brain-map.org/) were followed as reference for identifying and naming different structures on the averaged MEMRI brain images. Amira® 5.21v VSG software (www.amira.com) was used for generating colored labels of brain structures. A three dimensional view with connected cursor was used for accurate identification of various structures.
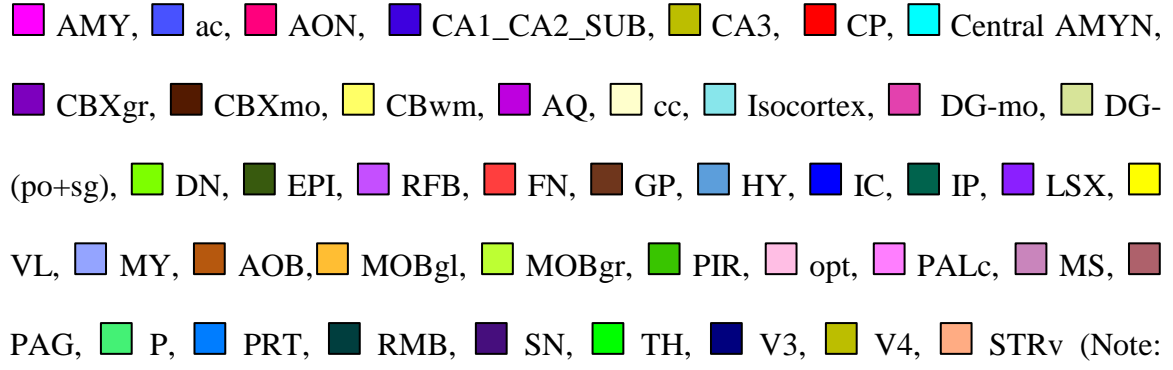
4.3. Results

4.3.1. Brain structures labeling

Representative slices from three orthogonal cross-sections of the population averaged MRI are shown in the first column of Fig. 4.1. The second displays the same slices with Laplacian edge enhancement. Improved contrast between structures is realized. The third column shows the manually labeled structures using Amira software. Significant image contrast seen is due to $MnCl_2$ and allowed the identification and delineation of 41 brain structures from the cerebrum (CH), brain stem (BS), cerebellum (CB), fiber tracts (FB), and ventricular systems (VS). All the identified structures' names are listed in Table 4.1. To the best of our knowledge this is the highest number of structures identified on *in vivo* mouse brain MRI.
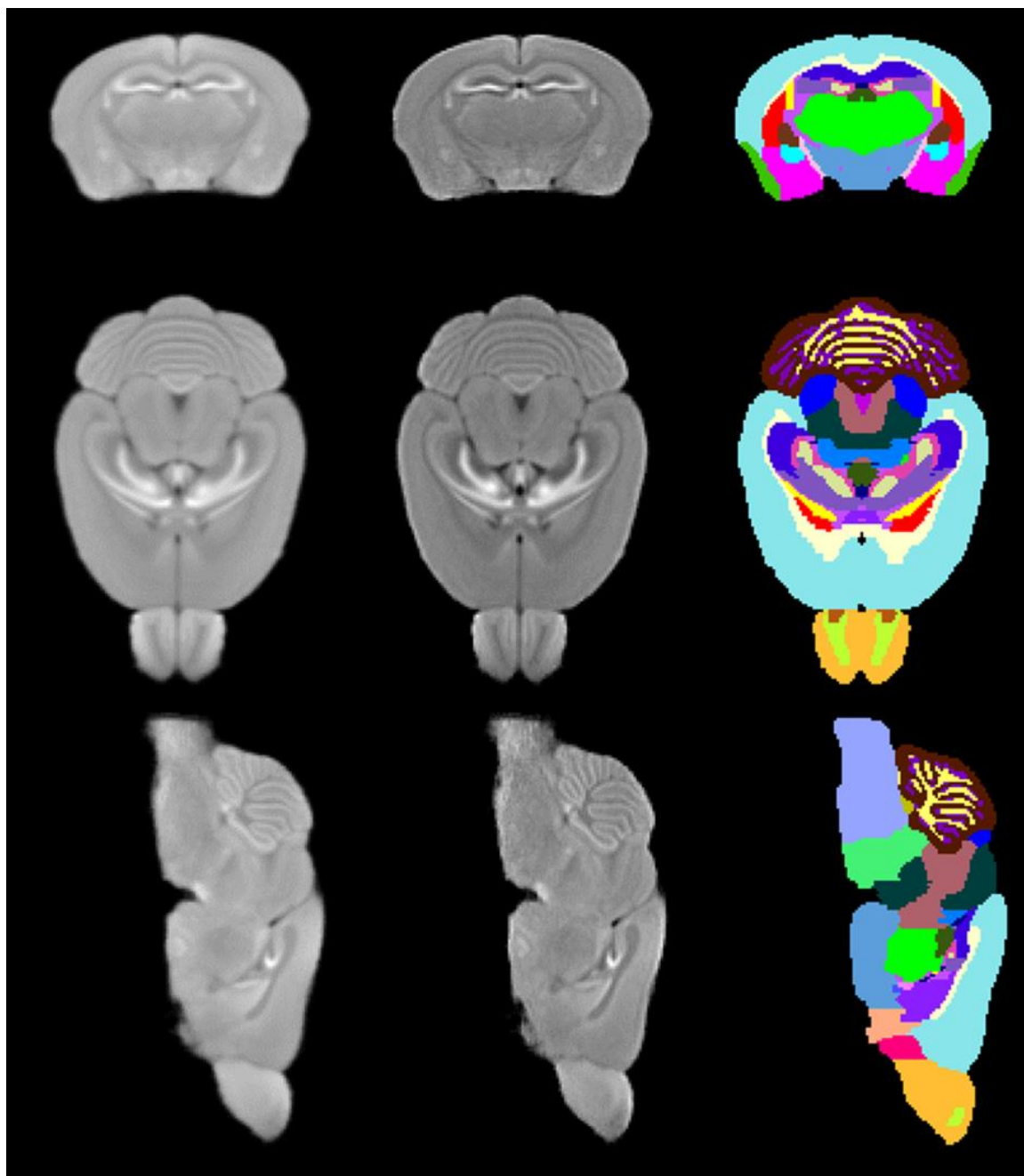
Figure 4.1. Columns: <u>First</u>: Three orthogonal planes of population average MRI. <u>Second</u>: Edge enhancement of images in first column. <u>Third</u>: Identified structures on these planes: ■ AMY, ■ ac, ■ AON, ■ CA1_CA2_SUB, ■ CA3, ■ CP, ■ Central AMYN, ■ CBXgr, ■ CBXmo, ■ CBwm, ■ AQ, ■ cc, ■ Isocortex, ■ DG-mo, ■ DG-(po+sg), ■ DN, ■ EPI, ■ RFB, ■ FN, ■ GP, ■ HY, ■ IC, ■ IP, ■ LSX, ■ VL, ■ MY, ■ AOB, ■ MOBgl, ■ MOBgr, ■ PIR, ■ opt, ■ PALc, ■ MS, ■ PAG, ■ P, ■ PRT, ■ RMB, ■ SN, ■ TH, ■ V3, ■ V4, ■ STRv (Note: Structures ac, AQ, DN, RFB, FN, IP, V3, and V4 are not presented in the third column of the figure)

Table 4.1. List of brain regions labeled on MEMRI brain atlas.

Region		Structure
CH: Cerebrum		
	Isocortex: Isocortex	Isocortex: Isocortex
	OLF: Olfactory areas	MOBgl: Main olfactory bulb, glomerular layer
		MOBgr: Main olfactory bulb, granule layer
		AOB: Accessory olfactory bulb
		AON: Anterior olfactory nucleus
		PIR: Piriform area
	HPF: Hippocampal formation	CA1_CA2_SUB: Field CA1 + Field CA2 + Subiculum
		CA3: field CA3 of hippocampus
		DG-mo: Dentate gyrus_molecular layer
		DG-(po+sg): Dentate gyrus_(polymorph layer + granular layer)
	STR: Striatum	CP: Caudoputamen
		STRv: Striatum ventral region
		LSX: Lateral septal complex
	PAL: Pallidum	PALc: Pallidium, caudal region
		GP: Globus pallidus
		MS: Medial septal nucleus

	AMY: Amygdala	AMY: Amygdala
FB: Fiber tracts		
		cc: corpus callosum
		opt: optic tract
		ac: anterior commissure
		RFB: Rest of fiber tracts
BS: Brain stem		
		TH: Thalamus
		EPI: Epithalamus
		HY: Hypothalamus
		IC: Inferior colliculus
		PAG: Periaqueductal gray
		PRT: Pretectal region
		SN: Substantia nigra
		RMB: Rest of midbrain
		P: Pons
		MY: Medulla
CB: Cerebellum		
		CBXmo: Cerebellar cortex, molecular layer
		CBXgr: Cerebellar cortex, granular layer
		CBwm: Cerebellar white matter
		FN: Fastigial nucleus
		IP: Interpose nucleus
		DN: Dentate nucleus

VS: Ventricular system	
	VL: Lateral ventricles
	V3: Third ventricle
	AQ: Cerebral aqueduct
	V4: Fourth ventricle

4.4. Discussion

We have developed a 3D *in vivo* MEMRI brain atlas for NSG mice containing 41 sub regions. We acknowledge that although this is not the first mouse brain atlas made, it is the sole one constructed by MEMRI for NSG mice analyses. Majority of previous such constructions were made on fixed or post-mortem in situ brains [7,9,10]. However, such prior works may not provide accurate assessment of *in vivo* volumetric and geometrical changes amongst brain regions [16,25]. Indeed, fixation protocols cause alterations in analyses for brain morphology even when MRI data with high resolution and SNR are employed. To this end, the present *in vivo* MEMRI brain atlas allows longitudinal quantitative morphological studies.

There are some advantages of the present approach. *First*, due to $MnCl_2$ ability to selectively reduce local T_1 relaxation times, the MEMRI provided increased contrast to noise ratio. *Second*, boundaries between brain structures are enhanced by Laplace Transform image processing. *Third*, specific molecular and granular layers in the brain regions such as the olfactory bulb and cerebellum were identified (Fig. 4.1.). Through such an approach, 41 structures on averaged *in vivo* MRI were delineated and then labeled. This is a significant improvement from prior 3D *in vivo* MRI atlases that enabled only half of the MEMRI-identified brain structures to be processed [16,17]. The developed atlas is made available to researchers through Neuroimaging Informatics Tools and Resources Clearinghouse (NITRC) website (https://www.nitrc.org/projects/memribrainatlas/).

4.5. Conclusion

An *in vivo* MEMRI-based atlas was generated for brains of NSG mice. Forty-one brain structures were identified to provide a coordinate system for spatial normalization. The atlas provides a database for studies of brain morphology, metabolomics, MR metrics, disease pathobiology, and drug pharmacokinetics in a range of infectious, inflammatory and degenerative disease of the nervous system.

4.6. References

1. Ito M., Hiramatsu H., Kobayashi K., Suzue K., Kawahata M., Hioki K., Ueyama Y., Koyanagi Y., Sugamura K., Tsuji K., Heike T. and Nakahata T., (2002) NOD/SCID/gamma(c)(null) mouse: an excellent recipient mouse model for engraftment of human cells. Blood. 100, 3175-3182.

2. Saito Y., Kametani Y., Hozumi K., Mochida N., Ando K., Ito M., Nomura T., Tokuda Y., Makuuchi H., Tajima T. and Habu S., (2002) The in vivo development of human T cells from CD34(+) cells in the murine thymic environment. Int. Immunol. 14, 1113-1124.

3. Janus C. and Welzl H., (2010) Mouse models of neurodegenerative diseases: criteria and general methodology. Methods Mol. Biol. 602, 323-345.

4. Trancikova A., Ramonet D. and Moore D. J., (2011) Genetic mouse models of neurodegenerative diseases. Prog. Mol. Biol. Transl. Sci. 100, 419-482.

5. Gorantla S., Poluektova L. and Gendelman H. E., (2012) Rodent models for HIV-associated neurocognitive disorders. Trends Neurosci. 35, 197-208.

6. Kovacevic N., Henderson J. T., Chan E., Lifshitz N., Bishop J., Evans A. C., Henkelman R. M. and Chen X. J., (2005) A three-dimensional MRI atlas of the mouse brain with estimates of the average and variability. Cereb. Cortex. 15, 639-645.

7. Ma Y., Hof P. R., Grant S. C., Blackband S. J., Bennett R., Slatest L., McGuigan M. D. and Benveniste H., (2005) A three-dimensional digital atlas database of the adult

C57BL/6J mouse brain by magnetic resonance microscopy. Neuroscience. 135, 1203-1215.

8. Chan E., Kovacevic N., Ho S. K., Henkelman R. M. and Henderson J. T., (2007) Development of a high resolution three-dimensional surgical atlas of the murine head for strains 129S1/SvImJ and C57Bl/6J using magnetic resonance imaging and micro-computed tomography. Neuroscience. 144, 604-615.

9. Dorr A. E., Lerch J. P., Spring S., Kabani N. and Henkelman R. M., (2008) High resolution three-dimensional brain atlas using an average magnetic resonance image of 40 adult C57Bl/6J mice. Neuroimage. 42, 60-69.

10. Aggarwal M., Zhang J., Miller M. I., Sidman R. L. and Mori S., (2009) Magnetic resonance imaging and micro-computed tomography combined atlas of developing and adult mouse brains for stereotaxic surgery. Neuroscience. 162, 1339-1350.

11. Chuang N., Mori S., Yamamoto A., Jiang H., Ye X., Xu X., Richards L. J., Nathans J., Miller M. I., Toga A. W., Sidman R. L. and Zhang J., (2011) An MRI-based atlas and database of the developing mouse brain. Neuroimage. 54, 80-89.

12. Nie J. and Shen D., (2013) Automated segmentation of mouse brain images using multi-atlas multi-ROI deformation and label fusion. Neuroinformatics. 11, 35-45.

13. Sunkin S. M., Ng L., Lau C., Dolbeare T., Gilbert T. L., Thompson C. L., Hawrylycz M. and Dang C., (2013) Allen Brain Atlas: an integrated spatio-temporal portal for exploring the central nervous system. Nucleic Acids Res. 41, D996-D1008.

14. Lein E. S., Hawrylycz M. J., Ao N., Ayres M., Bensinger A., Bernard A., Boe A. F., Boguski M. S., Brockway K. S., Byrnes E. J., Chen L., Chen L., Chen T. M., Chin M. C., Chong J., Crook B. E., Czaplinska A., Dang C. N., Datta S., Dee N. R., Desaki A. L., Desta T., Diep E., Dolbeare T. A., Donelan M. J., Dong H. W., Dougherty J. G., Duncan B. J., Ebbert A. J., Eichele G., Estin L. K., Faber C., Facer B. A., Fields R., Fischer S. R., Fliss T. P., Frensley C., Gates S. N., Glattfelder K. J., Halverson K. R., Hart M. R., Hohmann J. G., Howell M. P., Jeung D. P., Johnson R. A., Karr P. T., Kawal R., Kidney J. M., Knapik R. H., Kuan C. L., Lake J. H., Laramee A. R., Larsen K. D., Lau C., Lemon T. A., Liang A. J., Liu Y., Luong L. T., Michaels J., Morgan J. J., Morgan R. J., Mortrud M. T., Mosqueda N. F., Ng L. L., Ng R., Orta G. J., Overly C. C., Pak T. H., Parry S. E., Pathak S. D., Pearson O. C., Puchalski R. B., Riley Z. L., Rockett H. R., Rowland S. A., Royall J. J., Ruiz M. J., Sarno N. R., Schaffnit K., Shapovalova N. V., Sivisay T., Slaughterbeck C. R., Smith S. C., Smith K. A., Smith B. I., Sodt A. J., Stewart N. N., Stumpf K. R., Sunkin S. M., Sutram M., Tam A., Teemer C. D., Thaller C., Thompson C. L., Varnam L. R., Visel A., Whitlock R. M., Wohnoutka P. E., Wolkey C. K., Wong V. Y., Wood M., Yaylaoglu M. B., Young R. C., Youngstrom B. L., Yuan X. F., Zhang B., Zwingman T. A. and Jones A. R., (2007) Genome-wide atlas of gene expression in the adult mouse brain. Nature. 445, 168-176.

15. MacKenzie-Graham A., Lee E. F., Dinov I. D., Bota M., Shattuck D. W., Ruffins S., Yuan H., Konstantinidis F., Pitiot A., Ding Y., Hu G., Jacobs R. E. and Toga A. W., (2004) A multimodal, multidimensional atlas of the C57BL/6J mouse brain. J. Anat. 204, 93-102.

16. Ma Y., Smith D., Hof P. R., Foerster B., Hamilton S., Blackband S. J., Yu M. and Benveniste H., (2008) In Vivo 3D Digital Atlas Database of the Adult C57BL/6J Mouse Brain by Magnetic Resonance Microscopy. Front. Neuroanat. 2, 1.

17. Bai J., Trinh T. L., Chuang K. H. and Qiu A., (2012) Atlas-based automatic mouse brain image segmentation revisited: model complexity vs. image registration. Magn. Reson. Imaging. 30, 789-798.

18. Aoki I., Wu Y. J., Silva A. C., Lynch R. M. and Koretsky A. P., (2004) In vivo detection of neuroarchitecture in the rodent brain using manganese-enhanced MRI. Neuroimage. 22, 1046-1059.

19. Silva A. C., Lee J. H., Wu C. W., Tucciarone J., Pelled G., Aoki I. and Koretsky A. P., (2008) Detection of cortical laminar architecture using manganese-enhanced MRI. J. Neurosci. Methods. 167, 246-257.

20. Chen X. J., Kovacevic N., Lobaugh N. J., Sled J. G., Henkelman R. M. and Henderson J. T., (2006) Neuroanatomical differences between mouse strains as shown by high-resolution 3D MRI. Neuroimage. 29, 99-105.

21. Koretsky A. P. and Silva A. C., (2004) Manganese-enhanced magnetic resonance imaging (MEMRI). NMR Biomed. 17, 527-531.

22. Silva A. C., Lee J. H., Aoki I. and Koretsky A. P., (2004) Manganese-enhanced magnetic resonance imaging (MEMRI): methodological and practical considerations. NMR Biomed. 17, 532-543.

23. Lee J. H., Silva A. C., Merkle H. and Koretsky A. P., (2005) Manganese-enhanced magnetic resonance imaging of mouse brain after systemic administration of MnCl2: dose-dependent and temporal evolution of T1 contrast. Magn. Reson. Med. 53, 640-648.

24. Kuo Y. T., Herlihy A. H., So P. W. and Bell J. D., (2006) Manganese-enhanced magnetic resonance imaging (MEMRI) without compromise of the blood-brain barrier detects hypothalamic neuronal activity in vivo. NMR Biomed. 19, 1028-1034.

25. Aggarwal M., Zhang J. and Mori S., (2011) Magnetic resonance imaging-based mouse brain atlas and its applications. Methods Mol. Biol. 711, 251-270.

CHAPTER - 5

Potential of N-acetylated-para-aminosalicylic Acid to Accelerate Manganese Enhancement Decline for Long-term MEMRI in Rodent Brain

*: Bade AN and Zhou B. contributed equally to the study

5.1. Introduction

Manganese (Mn^{2+})-enhanced MRI (MEMRI) is a powerful imaging tool to measure rodent neural structure, function and linked pathways [1-3]. It is facilitated by Mn^{2+} entry into neurons that occurs through calcium (Ca^{2+}) channels. Here, Mn^{2+} ions accumulate in neurons and are transported along axons. Such ion trafficking reflects neuronal function and networks [1-5]. Mn^{2+} is an excellent T_1 shortening paramagnetic contrast agent inducing signal enhancement on T_1-weighted (T_1-wt) MRI. The retention of Mn^{2+} in brain is prolonged with a half-life ($t_{1/2}$) of 51 to 74 days [5]. Such ion retention allows studies of brain function performed on non-restrained awake rodents [6-10]. In this context, Mn^{2+} administration, sensory stimulation and/or behavioral tests are performed outside the MRI scanner and prior to imaging tests. Studies have shown that brain activities that took place days before imaging tests could be detected using appropriate Mn^{2+} administration schemes such as implanted osmotic pump infusion [9,10]. The long Mn^{2+} brain retention time also enables the monitoring of Mn^{2+} axonal transportation for studies evaluating neural pathways[11-13]. MEMRI is also proven a valuable tool in neurodegenerative disorder studies using rodents [14-25]. However and despite such advantages, its application is limited in the longitudinal follow-up of neurodegenerative disorders due to the prolonged washout time of Mn^{2+}. During the time span of the studies that can be as long as weeks and even months, repeated Mn^{2+} administration is usually necessary to keep brain Mn^{2+} concentration consistent among imaging sessions. This requires carefully designed dosing if imaging needs to be performed before the residual

Mn^{2+} from preceding administrations is eliminated. Infusion using commercially available osmotic pumps may keep brain Mn^{2+} concentration consistent for up to six weeks (Alzet, Cupertino, CA), which is usually not sufficient in time to evaluate the progression of neurodegenerative disorders in rodents. Moreover, repeated or continuous Mn^{2+} administration can cause secondary toxicities [26]. One solution is to accelerate Mn^{2+} brain elimination after each MEMRI tests and as such limit the effect of residual Mn^{2+} on the MEMRI evaluation. Accelerated Mn^{2+} washouts may also serve to minimize Mn^{2+} toxicity.

With this in mind, we tested whether N-acetylated-para-aminosalicylic acid (AcPAS) could accelerate Mn^{2+} elimination from brain. AcPAS, an N-acetylated metabolite of para-aminosalicylic acid (PAS), was previously used to treat human manganism, a disorder which parallels several of the clinical features of Parkinson's disease [27]. Treatment of Mn^{2+} intoxication is linked to PAS chelation [28,29]. Chelation is the binding of organic compounds and metal ions. The brain distribution, metabolism, and time-concentration relationships of PAS and its major metabolite, AcPAS, were previously investigated [30,31]. The results demonstrated that AcPAS chelates Mn^{2+}. AcPAS has higher brain concentration and possesses a longer $t_{1/2}$ than PAS. Herein we demonstrate that AcPAS can be employed to improve the MEMRI utility by permitting serial brain measurements in health and disease.

5.2. Materials and Methods

5.2.1. Study Design

C57BL/6 mice were used in this study. Mice were housed in the University of Nebraska Medical Center (UNMC) laboratory animal facility according to the American Animal Association and Laboratory Animal Care guidance. All procedures were approved by the Institutional Animal Care and Use Committee at UNMC. The kinetics of AcPAS in brain tissue and plasma was first studied using high-performance liquid chromatography (HPLC) using one group of mice. Another group of mice was first administrated $MnCl_2$ via the intraperitoneal (i.p.) route, followed with PBS (n =3), low dose (n = 3, 100 mg/kg), medium dose (n = 3, 150 mg/kg) and high dose AcPAS (n = 3, 200 mg/kg) three times daily for two weeks. The doses and administration scheme were designed based on the previous PK studies of AcPAS [30,31]. MRI was performed one day after the $MnCl_2$ administration followed by AcPAS/PBS treatment. Two more MRI scans were performed at one and weeks of AcPAS/PBS treatment. After the last MRI, the mice were immediately euthanized for inductively coupled plasma mass spectrometry (ICP/MS) analysis of brain Mn^{2+} concentrations. The timeline of the study design is shown in Fig. 5.1. Three animals were randomly selected from the above 12 AcPAS/PBS-treated mice and were scanned before any drug administration for baseline measurements of MRI and ICP/MS.

5.2.2. AcPAS Synthesis

AcPAS was synthesized by a modified procedure [32]. Briefly, p-aminosalicylic acid (0.33 mol), was dissolved in 100 ml of 2 M hydrochloric acid and stirred with sodium acetate (0.33 mol) in water at 0° C. The reaction mixture was stirred overnight with 50 ml of acetic anhydride at room temperature. The brown precipitate obtained was filtered,

washed, dried and dissolved in 0.1M sodium hydroxide then stirred overnight. The resulting solution was adjusted to pH 2 with HCl. The product was extracted with ethyl acetate (3 × 75 ml) and the extracts were dried over anhydrous sodium sulphate. The solid residue was washed with hexane to produce 52 % yield of pure AcPAS. The identity of AcPAS was confirmed by NMR with > 99 % purity.

5.2.3. High performance liquid chromatography (HPLC)

AcPAS (*200* mg/kg) was administered to mice (n = 9) by i.p. injection. Plasma was collected at 0.5, 1, 2, 6 and 12 hours. Mouse peripheral blood samples (100 μl) were collected from submandibular vein (cheek bleed) by using sterile lancets (MEDIpoint, Inc., Mineola, NY) in EDTA coated tubes. Plasma was separated by centrifugation of blood samples at 1,800 rpm for 8 min at 4°C within 1 h of sample collection and stored at -80°C until analysis. Brain tissues (cortex, thalamus, olfactory bulb) of same group of mice administered with the same dose of AcPAS were collected at 6, 8 and 12 (n = 3 for each time point) hours after administration. AcPAS from plasma and tissues were extracted using acetonitrile. AcPAS was quantified by HPLC according to the method of Sugamori et al. [33]. Briefly, extracted plasma or brain samples were injected in duplicate (20μl) onto a Shimadzu HPLC (Shimadzu Scientific Instruments, Columbia, MD) containing a Synergi 4μ Hydro-RP column (4.6 × 150 mm) (Phenomenex, Torrance, CA) and extruded using an isocratic mobile phase of 7% acetonitrile/1% acetic acid/0.1% triethylamine at a flow rate of 1.6 ml/min. AcPAS were detected at a wavelength of 270 nm and quantitated by peak comparisons to a standard curve (0.05-50 μg/ml).

5.2.4. MnCl₂ and AcPAS treatment

$MnCl_2 \cdot 4H_2O$ (Sigma-Aldrich, St Louis, MO) was added to 0.9% w/v $NaCl_2$ (Hospira, Lake forest, IL) to make 50 mM $MnCl_2$ solution. $MnCl_2$ solution was delivered i.p. at a dose of 60 mg/kg consecutively four times at 24 hour intervals. The fractional administration scheme was designed to minimize Mn^{2+} toxicity [34]. After injection, the mice were observed daily to monitor potential Mn^{2+} toxicities. AcPAS injection started one day after the $MnCl_2$ administration. AcPAS (1 mg) was mixed with 1 μl DMSO in a glass container. More (1 − 2 μl) DMSO was added until the compound was dissolved. Physiological saline (0.9% NaCl) was added to dilute the solution to 20 mg/ml AcPAS. The solution became a suspension with addition of saline. It was then stored at 4 °C. Before each injection, the suspension was thoroughly mixed by shaking. AcPAS was injected i.p. 3 times per day at eight-hour intervals for two weeks. Before each drug injection, the animal was observed for any abnormal changes in behavior, hair coat, facial expression, ambulation and body weight.

5.2.5. MRI

MRI was performed on a Bruker Bioscan 7 Tesla/21 cm MRI (Bruker, Billerica, MA) operating Paravision 5.1 with a 82 mm quadrature volume resonator and a 4-channel phased array receive coil. Mice were anesthetized by inhalation of isoflurane in 100% oxygen and maintained 40-80 breaths/minute. Mice were scanned using T_1 mapping (fast spin echo with variable TR from 0.4 s to 10 s, TE = 7.0 ms, 12 coronal slices, slice thickness = 0.5 mm, in-plane resolution = 0.156×0.156 mm^2, FOV = 20 x 20 mm^2) and three-dimensional T_1W MRI (gradient recalled echo, TR/TE = 20/4.5 ms, flip angle =

20°, *FOV = 19.2* (Left - Right) x 19.2 (Superior - Inferior) x 30.0 (Anterior - Posterior) mm^3, spatial resolution $= 0.1 \times 0.1 \times 0.1$ mm^3).

To reduce the influence of the inhomogeneous signal reception on the T_1W images by the phased array surface coil, N3 field inhomogeneity correction [35] was first performed on each image using MIPAV (CIT, NIH). The brain volumes in the T_1W images were extracted using an in-house Matlab program [36] based on the level sets method. The brain images were then registered to the MRI-based mouse brain atlas downloaded from the Laboratory of Neuro Imaging (LONI) at the University of Southern California using affine transformation first, and then nonlinear transformation (DiffeoMap, John Hopkins University, Baltimore, MD).

To use signal changes in high resolution T_1W MRI to represent Mn^{2+} accumulation, signal differences need to be scaled to absolute changes in T_1 values. This is achieved by calibrating the baseline and post Mn^{2+} injection T_1W images using T_1 values. The T_1 maps were first generated using an in-house Interactive Data Language (IDL) version 8.2 (Exelis Visual Information Solutions, Boulder, Colorado) program from the data acquired by T_1 mapping sequence. Regions of interest (ROI) were then placed on relatively uniform tissue regions including frontal cortex and caudate on T_1 maps and T_1W images. The baseline and post Mn^{2+} injection longitudinal relaxivity and T_1W signal intensity in the ROIs were measured. We assumed that the effect of the system variation is a constant C (calibration factor) and set system parameter of the post-manganese session as 1, then the measured baseline signal (designated as $S_{bl}{}^{C}$) is $S_{bl}{}^{C} = CS_{bl}$, where S_{bl} is the true (calibrated) baseline signal. The calibration factor was calculated as $C = (S_{bl}{}^{C}/S_{Mn}) \times (R_{1Mn}/R_{1bl})$, where R_{1bl} and R_{1Mn} are baseline and post Mn^{2+}

injection longitudinal relaxivities, respectively; S_{Mn} is post Mn^{2+} T_1W signal intensity. The calibration factor was then applied to the baseline T_1W image to calculate the true baseline image: $S_{bl} = S_{bl}{}^C / C$.

The Mn^{2+} induced T_1W signal enhancement was calculated by: $(S_{Mn} - S_{bl}) / S_{bl}$. This equation was derived by ignoring the $T_2{}^*$ effect in the MRI signal generated using a spoiled gradient recalled echo, and replacing the exponential of $(-TR/T_1)$ with the first two terms of its Taylor expansion. These operations were appropriate as a previous study has shown that Mn^{2+} induced T_2 change is small compared to T_1 reduction [37], and $(-TR/T_1)$ is small ($TR = 20$ ms and $T_1 > 800$ ms in most brain regions). Using the LONI brain atlas, enhancement on brain regions/sub-regions was calculated. A region-by-region comparison was performed between AcPAS treated groups and PBS controls using Student's t-test at each time point.

5.2.6. ICP/MS Analyses

Known weights of thawed brain regions (cortex, thalamus, olfactory bulb), collected from the animals were decomposed by wet-ashing in vials with six volumes of concentrated nitric acid followed by microwave (MARS, CEM Corp., Matthews, NC) heating at 200 °C. Total manganese concentrations were determined by ICP-MS (NexION 300Q, PerkinElmer, MA, USA).

5.2.7. Statistical Analysis

Student's t-tests were used for all statistical analyses. The significance level was 0.05.

5.3. Results

5.3.1. AcPAS plasma and brain levels

AcPAS plasma and brain concentrations are shown in Figure 5.2. AcPAS was reduced in concentration at 2 hours from > 400 to < 23 ng/ml in plasma. The reduction reached eight ng/ml at 12 hours. AcPAS increased in the cortex, thalamus and olfactory bulbs with time after six hours. The highest AcPAS tissue concentration was in olfactory bulbs with less drug in the thalamus and cortex (Fig. 5.2).

5.3.2. MRI

Mn^{2+} induced enhancement on T_1W MRI was seen after 24 hours of $MnCl_2$ injection (Fig 5.3.A-a). Mn^{2+} induced signal enhancement on T_1W MR images was seen in the hippocampus, cerebellum and olfactory bulbs (Fig 5.3.A-a) [3,4]. The MR images one week after $MnCl_2$ injection are illustrated in Fig 5.3.A-b with the top panel the PBS and bottom high dose AcPAS treated mice. The signal intensity was decreased at 1 week in both groups. Compared to PBS controls, decreased signal intensities were seen in AcPAS treated mice. This was most notable in the hippocampus and cortex. After 2 weeks of treatment, AcPAS treated mice (Fig 5.3.A-c, top panel) showed greater decreased signal intensity than PBS controls (Fig 5.3.A-c, bottom panel) throughout the multiple brain regions.

5.3.3. Mn^{2+} enhancement

The enhancement maps are shown in Fig 5.3.B, and quantified region-specific enhancement results are listed in Table 1. After 24 hours, Mn^{2+} induced enhancement is

throughout the whole brain (96% enhancement) with the relatively high enhancement on olfactory system (Olf, 97%), lateral olfactory tract (lo, 136%), optic chiasm (ox, 98%), hippocampus (HIP, 97%), hypothalamus (Hy, 98%), interpeduncular nucleus (IP, 97%), and cerebellum (Cb, 96%) regions (Fig 5.3.B-a, 1st column in Table 5.1). The brain region abbreviations follow the conventions in the Paxinos and Franklin mouse brain atlas. Natural enhancement decline was clearly seen in PBS controls after one week from 85-136% to 30-62% (Fig 5.3.B-b top panel, 2nd column in Table 5.1). Mice treated with low (100 mg/kg) and medium (150 mg/kg) doses did not show significant difference compared to PBS controls (data not shown). The enhancement in high dose (200 mg/kg) AcPAS treated mice was lower than in PBS animals (Fig 5.3.B-b). The enhancement difference was significant ($p < 0.05$) on substantia nigra (SN), corpus callosum (cc), thalamus (Th), hippocampus (HIP) and olfactory bulb (Olf) regions (3rd column in Table 5.1).

The enhancement decreased significantly after two weeks in PBS controls to 22-59% (Fig 5.3.B-c top panel, 4th column in Table 5.1). After two-weeks, medium dose (150 mg/kg) AcPAS treated mice showed significantly decreased enhancement compared to PBS controls on fornix (f) and optic chiasm (ox) (5th column in Table 5.1). In high dose (200 mg/kg) AcPAS treated mice, a number of brain regions showed significantly decreased enhancement including the caudate putamen (CPu), basal ganglia (BG) and internal capsule (ic) (6th column in Table 5.1). The whole brain enhancement in high dose (200 mg/kg) AcPAS treated mice was also significantly less than in PBS controls. The brain regions with significantly reduced enhancement in high dose (200 mg/kg) AcPAS treated mice are shown in Fig 5.4.

Manganese concentrations measured by ICP/MS in mouse brains at 24 hours after MnCl$_2$ administration were 183±25.8 parts per billion (ppb) in cortex, 280±29.2 ppb in thalamus, 203±14.8 ppb in hippocampus, and 507±164 ppb in olfactory bulbs. The concentrations were presented as mean±SEM. The concentrations decreased in PBS treated controls after 2 weeks to 61.6±1.45, 71.7±2.96, 57.6±7.61 and 170±21.4 ppb in cortex, thalamus, hippocampus and olfactory bulbs, respectively. The concentrations in high dose AcPAS treated mice at two weeks were 74.3±9.29, 85.3±22.2, 72.8±26.6, and 119±19.4 ppb in cortex, thalamus, hippocampus and olfactory bulbs, respectively. No significant difference was found between saline controls and AcPAS treated mice ($p >$ 0.1, data not shown).

5.4. Discussion

This study investigated the abilities of AcPAS treatment to affect repeated MEMRI measurements of brain structure and function. We demonstrate that, even though AcPAS did not lead to accelerated Mn^{2+} brain elimination, it suppressed significantly Mn^{2+}-induced MRI enhancement after about two weeks treatment when using the high dose (200mg/kg $\times$ 3 daily). Based on these findings, AcPAS has the potential to enable repeated MEMRI measurements and minimize Mn^{2+} toxicity.

AcPAS can be rapidly eliminated from blood within an hour. As soon as six hours after the injection, AcPAS has entered the brain and its concentration increased over the next six hours. This finding is in agreement with a previous PK study of PAS and AcPAS (32). These findings suggested that, to achieve sufficient brain concentrations, AcPAS must be administrated by multiple injections over a day or by continuous infusion.

Therefore the dosing and administration scheme were designed based on these findings and previous PK and PD studies of AcPAS (32). The accelerated Mn^{2+} washout induced by AcPAS is different among brain regions. HIP, TH, CPu are among the regions of fastest washout. This is in the agreement of a previous study showing high AcPAS concentration in these regions [30].

The ICP/MS data suggested that AcPAS failed to speed the elimination of Mn^{2+}. However, MRI results showed faster enhancement decline in AcPAS treated mice compared to PBS controls at high dose. The discordant results can be explained as follows. The chelation of paramagnetic Mn^{2+} by AcPAS limits its interaction with water molecules, and thus causes the decrease in Mn^{2+} induced signal enhancement. On the other hand, the high tissue affinity and long $t_{1/2}$ of AcPAS limit the elimination of chelated Mn^{2+} from brain.

The study showed that an average 17% enhancement remains in brain after 2-week high dose AcPAS treatment. Further experiments are necessary to determine the time to complete elimination of enhancement. Nevertheless, AcPAS provides an option for serial studies with a shorter time interval compared to the inherent Mn^{2+} washout of 17-26 weeks [5]. We did not observe any side-effects of AcPAS in the animals. It is quite possible that higher dose (> 200 mg/kg) AcPAS treatments would eliminate the enhancement more quickly than the highest dose used in this study.

A more comprehensive study is being planned, in which a second MEMRI experiment will be performed after AcPAS treatment to ensure the enhancement efficiency still holds, and Mn^{2+} update and retention by neurons are not affected after the AcPAS treatment. The study will prove the feasibility of using AcPAS for repeated

MEMRI. We do not expect AcPAS treatment causes brain water relaxivity changes, because AcPAS is an organic compound cleared from brain with a half-life of 100-200 minutes [30], and is diamagnetic. To prove the hypothesis, one more group of mice will be added in the planned study that will receive AcPAS treatment and MRI scans but not $MnCl_2$ injection. This group is to detect any effect on brain water relaxivity caused by AcPAS treatment.

PAS [4-amino-2-hydroxybenzoic acid (Paser); CAS number, 65-49-6] has been well known as an antituberculosis drug since the 1950s [38]. Its side effects on humans have been investigated [38]. The toxicity of its tissue metabolite - AcPAS needs to be further studied for use in MEMRI. In this study, no abnormal changes in behavior, hair coat, facial expression, ambulation and body weight were found in the animals. Even though AcPAS does not accelerate the removal of Mn^{2+} from brain, its chelation of Mn^{2+} is believed to minimize Mn^{2+} toxicity. If AcPAS is to be used in neurological disease studies using rodent models, its compatibility with the studies needs to be considered to assure its administration will not advertently affecting key physiological/disease-related parameters. In conclusion, we showed that, while AcPAS does not eliminate Mn^{2+} from brain, it accelerates Mn^{2+} induced enhancement decline in MRI. The results suggested the potential to use AcPAS for serial MEMRI measurements of voltage-gated calcium channel activity and morphology in rodent brains. In future studies, we will follow the animals longer to study the long-term effects of AcPAS on Mn^{2+} elimination and parallel MEMRI test results.
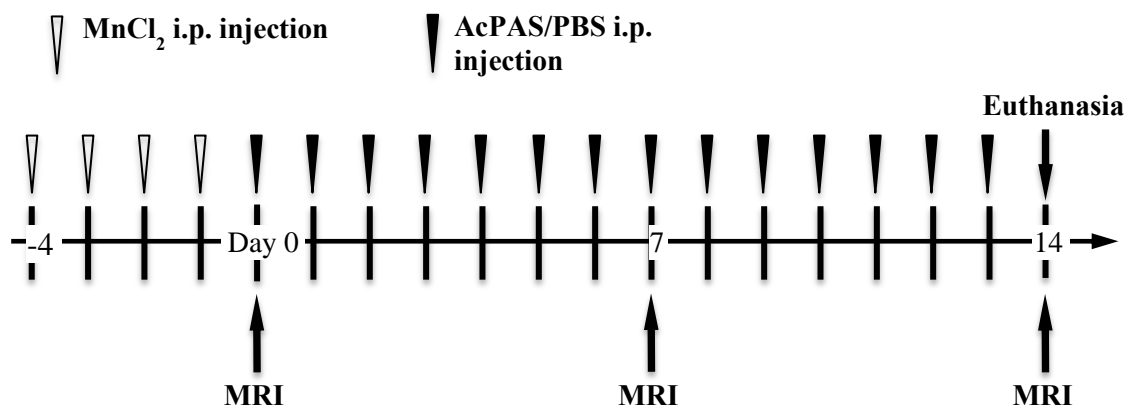
Figure 5.1. Study design. Mice were first administrated with $MnCl_2$, followed with PBS (n =3), low dose (n = 3, 100 mg/kg), medium dose (n = 3, 150 mg/kg) or high dose AcPAS (n = 3, 200 mg/kg) for two weeks. MRI was performed on the mice at one and two weeks after $MnCl_2$ administration. After the second MRI, the mice were immediately euthanized for ICP/MS analysis of brain Mn^{2+} concentrations.
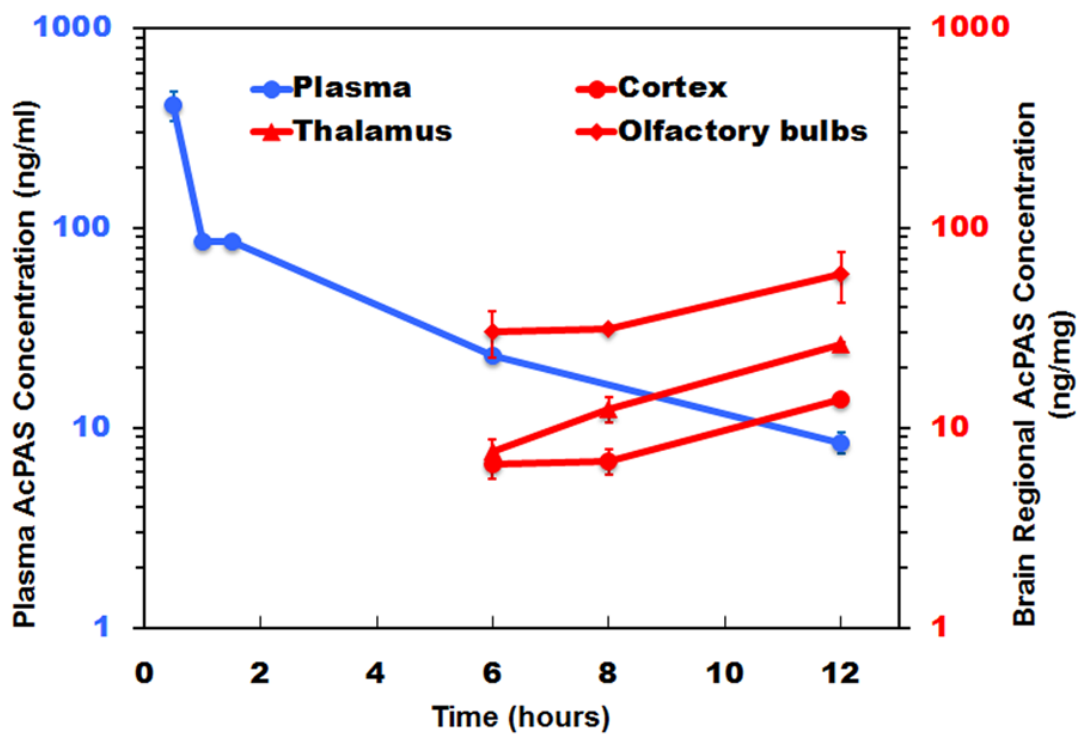
Figure 5.2. AcPAS concentrations measured by HPLC in plasma (blue line) and in the brain regions (red lines). The concentrations in plasma were measured in ng/ml (left vertical axis), and in brain were measured in ng/mg (right vertical axis). The error bar at each time point shows the mean standard error of the measurement.
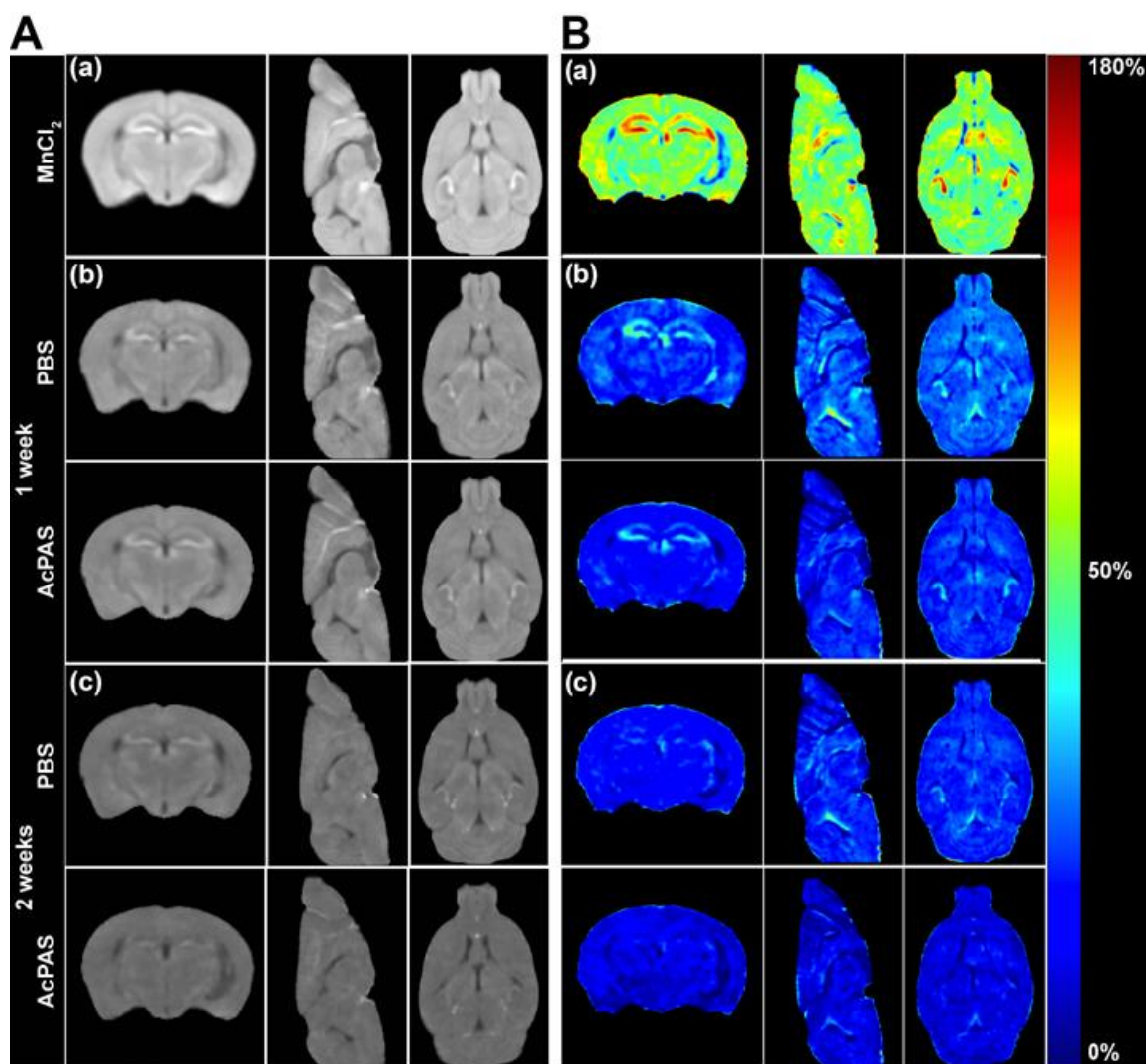
Figure 5.3. (A) MRI data. (a) Averaged MRI of mice (n = 9) at 24 hours after $MnCl_2$ administration. (b) Averaged MRI of PBS controls (n = 3, top panel) and high dose AcPAS treated mice (n = 3, bottom panel) at one week after $MnCl_2$ administration. (c) Averaged MRI of PBS controls (n = 3, top panel) and high dose AcPAS treated mice (n = 3, bottom panel) at two weeks after $MnCl_2$ administration. (B) Manganese enhancement maps corresponding to Figure 3A.
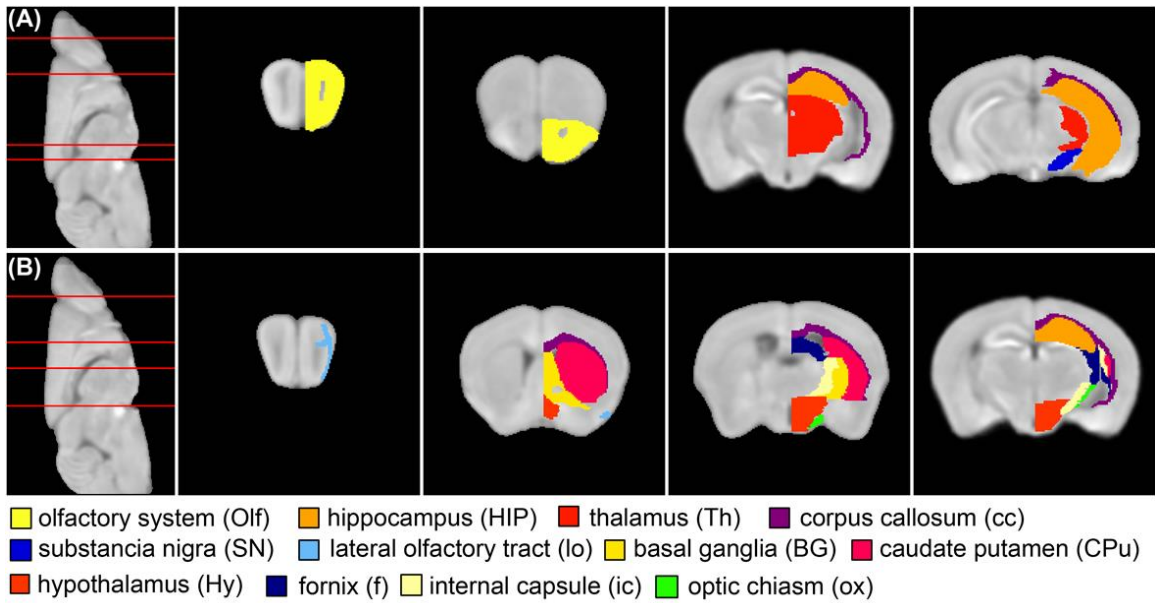
Figure 5.4. Brain regions with significantly less enhancement in mice after one (A) and two (B) weeks high dose AcPAS treatment compared to in PBS controls. The regions are shown in coronal slices, whose locations are indicated using red lines on the sagittal slices in the leftmost column.

Table 5.1. Brain regions with significantly decreased enhancement in mice after 1 and 2 weeks high dose AcPAS treatment compared to in PBS controls.

Enhancement data are presented as percentage and in Mean ± Standard deviation.

*: $p < 0.1$; **: $p < 0.05$

	0 week	1 week		2 weeks		
	All (%)	PBS (%)	High Dose (%)	PBS (%)	Mid Dose (%)	High Dose (%)
f	89±13	35±7	27±7	29±2	21±0**	18±6**
Ox	98±14	37±11	37±7	35±6	23±3**	22±5**
Cb	96±13	39±7	32±7	28±6	21±3	19±4*
SN	91±12	40±4	30±7**	22±8	16±4	12±5*
IP	97±14	50±3	37±11*	31±9	24±2	18±7*
cc	87±12	37±4	27±6**	25±6	17±2*	15±4**
Hy	98±13	41±5	37±5	33±7	23±2*	17±5**
Th	89±13	38±4	28±5**	25±7	20±1	16±5*
CPu	90±12	40±4	30±8*	29±7	20±1*	17±4**
BG	95±13	42±4	33±8*	31±8	21±1	17±6**
HIP	97±13	42±4	33±6**	29±8	20±0	17±5**
lo	136±24	62±20	60±11	59±12	45±2	39±9**
Olf	97±13	45±8	31±8**	28±5	22±1	20±6*
Cx	95±14	40±8	32±6*	29±8	23±0	18±4*
ic	85±16	30±4	24±7	22±6	16±6	13±4**
fr	95±17	38±6	32±4*	27±10	23±5	17±6
Br	**96±16**	**36±9**	**29±7**	**27±6**	**22±2**	**17±5****

5.5. References

1. Koretsky A. P. and Silva A. C., (2004) Manganese-enhanced magnetic resonance imaging (MEMRI). NMR Biomed. 17, 527-531.

2. Pautler R. G., (2006) Biological applications of manganese-enhanced magnetic resonance imaging. Methods Mol. Med. 124, 365-386.

3. Silva A. C. and Bock N. A., (2008) Manganese-enhanced MRI: an exceptional tool in translational neuroimaging. Schizophr. Bull. 34, 595-604.

4. Silva A. C., Lee J. H., Aoki I. and Koretsky A. P., (2004) Manganese-enhanced magnetic resonance imaging (MEMRI): methodological and practical considerations. NMR Biomed. 17, 532-543.

5. Takeda A., (2003) Manganese action in brain function. Brain Res. Brain Res. Rev. 41, 79-87.

6. Bissig D. and Berkowitz B. A., (2009) Manganese-enhanced MRI of layer-specific activity in the visual cortex from awake and free-moving rats. Neuroimage. 44, 627-635.

7. Bissig D. and Berkowitz B. A., (2011) Same-session functional assessment of rat retina and brain with manganese-enhanced MRI. Neuroimage. 58, 749-760.

8. Holt A. G., Bissig D., Mirza N., Rajah G. and Berkowitz B., (2010) Evidence of key tinnitus-related brain regions documented by a unique combination of manganese-enhanced MRI and acoustic startle reflex testing. PLoS One. 5, e14260.

9. Hoch T., Kreitz S., Gaffling S., Pischetsrieder M. and Hess A., (2013) Manganese-enhanced magnetic resonance imaging for mapping of whole brain activity patterns associated with the intake of snack food in ad libitum fed rats. PLoS One. 8, e55354.

10. Eschenko O., Canals S., Simanova I., Beyerlein M., Murayama Y. and Logothetis N. K., (2010) Mapping of functional brain activity in freely behaving rats during voluntary running using manganese-enhanced MRI: implication for longitudinal studies. Neuroimage. 49, 2544-2555.

11. Canals S., Beyerlein M., Keller A. L., Murayama Y. and Logothetis N. K., (2008) Magnetic resonance imaging of cortical connectivity in vivo. Neuroimage. 40, 458-472.

12. Sandvig I., Thuen M., Hoang L., Olsen O., Sardella T. C., Brekken C., Tvedt K. E., Barnett S. C., Haraldseth O., Berry M. and Sandvig A., (2012) In vivo MRI of olfactory ensheathing cell grafts and regenerating axons in transplant mediated repair of the adult rat optic nerve. NMR Biomed. 25, 620-631.

13. Sandvig A., Sandvig I., Berry M., Olsen O., Pedersen T. B., Brekken C. and Thuen M., (2011) Axonal tracing of the normal and regenerating visual pathway of mouse, rat, frog, and fish using manganese-enhanced MRI (MEMRI). J. Magn. Reson. Imaging. 34, 670-675.

14. Bertrand A., Khan U., Hoang D. M., Novikov D. S., Krishnamurthy P., Rajamohamed Sait H. B., Little B. W., Sigurdsson E. M. and Wadghiri Y. Z., (2013) Non-invasive, in vivo monitoring of neuronal transport impairment in a mouse model of tauopathy using MEMRI. Neuroimage. 64, 693-702.

15. Dedeurwaerdere S., Fang K., Chow M., Shen Y. T., Noordman I., van Raay L., Faggian N., Porritt M., Egan G. F. and O'Brien T. J., (2013) Manganese-enhanced MRI reflects seizure outcome in a model for mesial temporal lobe epilepsy. Neuroimage. 68, 30-38.

16. Gallagher J. J., Zhang X., Ziomek G. J., Jacobs R. E. and Bearer E. L., (2012) Deficits in axonal transport in hippocampal-based circuitry and the visual pathway in APP knock-out animals witnessed by manganese enhanced MRI. Neuroimage. 60, 1856-1866.

17. Jouroukhin Y., Ostritsky R., Assaf Y., Pelled G., Giladi E. and Gozes I., (2013) NAP (davunetide) modifies disease progression in a mouse model of severe neurodegeneration: protection against impairments in axonal transport. Neurobiol. Dis. 56, 79-94.

18. Malheiros J. M., Polli R. S., Paiva F. F., Longo B. M., Mello L. E., Silva A. C., Tannus A. and Covolan L., (2012) Manganese-enhanced magnetic resonance imaging detects mossy fiber sprouting in the pilocarpine model of epilepsy. Epilepsia. 53, 1225-1232.

19. Perez P. D., Hall G., Kimura T., Ren Y., Bailey R. M., Lewis J., Febo M. and Sahara N., (2013) In vivo functional brain mapping in a conditional mouse model of human tauopathy (tauP301L) reveals reduced neural activity in memory formation structures. Mol. Neurodegener. 8, 9-1326-8-9.

20. Wideroe M., Havnes M. B., Morken T. S., Skranes J., Goa P. E. and Brubakk A. M., (2012) Doxycycline treatment in a neonatal rat model of hypoxia-ischemia reduces cerebral tissue and white matter injury: a longitudinal magnetic resonance imaging study. Eur. J. Neurosci. 36, 2006-2016.

21. Kawai Y., Aoki I., Umeda M., Higuchi T., Kershaw J., Higuchi M., Silva A. C. and Tanaka C., (2010) In vivo visualization of reactive gliosis using manganese-enhanced magnetic resonance imaging. Neuroimage. 49, 3122-3131.

22. Malheiros J. M., Longo B. M., Tannus A. and Covolan L., (2012) Manganese-enhanced magnetic resonance imaging in the acute phase of the pilocarpine-induced model of epilepsy. Einstein (Sao. Paulo). 10, 247-252.

23. Benveniste H., Ma Y., Dhawan J., Gifford A., Smith S. D., Feinstein I., Du C., Grant S. C. and Hof P. R., (2007) Anatomical and functional phenotyping of mice models of Alzheimer's disease by MR microscopy. Ann. N. Y. Acad. Sci. 1097, 12-29.

24. Faas H., Jackson W. S., Borkowski A. W., Wang X., Ma J., Lindquist S. and Jasanoff A., (2010) Context-dependent perturbation of neural systems in transgenic mice expressing a cytosolic prion protein. Neuroimage. 49, 2607-2617.

25. Pelled G., Bergman H., Ben-Hur T. and Goelman G., (2007) Manganese-enhanced MRI in a rat model of Parkinson's disease. J. Magn. Reson. Imaging. 26, 863-870.

26. Tuschl K., Mills P. B. and Clayton P. T., (2013) Manganese and the brain. Int. Rev. Neurobiol. 110, 277-312.

27. Jiang Y. M., Mo X. A., Du F. Q., Fu X., Zhu X. Y., Gao H. Y., Xie J. L., Liao F. L., Pira E. and Zheng W., (2006) Effective treatment of manganese-induced occupational Parkinsonism with p-aminosalicylic acid: a case of 17-year follow-up study. J. Occup. Environ. Med. 48, 644-649.

28. Nelson M., Huggins T., Licorish R., Carroll M. A. and Catapane E. J., (2010) Effects of p-Aminosalicylic acid on the neurotoxicity of manganese on the dopaminergic innervation of the cilia of the lateral cells of the gill of the bivalve mollusc, Crassostrea virginica. Comp. Biochem. Physiol. C. Toxicol. Pharmacol. 151, 264-270.

29. Zheng W., Jiang Y. M., Zhang Y., Jiang W., Wang X. and Cowan D. M., (2009) Chelation therapy of manganese intoxication with para-aminosalicylic acid (PAS) in Sprague-Dawley rats. Neurotoxicology. 30, 240-248.

30. Hong L., Jiang W., Pan H., Jiang Y., Zeng S. and Zheng W., (2011) Brain regional pharmacokinetics of p-aminosalicylic acid and its N-acetylated metabolite: effectiveness in chelating brain manganese. Drug Metab. Dispos. 39, 1904-1909.

31. Hong L., Jiang W., Zheng W. and Zeng S., (2011) HPLC analysis of para-aminosalicylic acid and its metabolite in plasma, cerebrospinal fluid and brain tissues. J. Pharm. Biomed. Anal. 54, 1101-1109.

32. Cummins C. L., O'Neil W. M., Soo E. C., Lloyd D. K. and Wainer I. W., (1997) Determination of p-aminosalicylic acid and its N-acetylated metabolite in human urine by capillary zone electrophoresis as a measure of in vivo N-acetyltransferase 1 activity. J. Chromatogr. B Biomed. Sci. Appl. 697, 283-288.

33. Sugamori K. S., Wong S., Gaedigk A., Yu V., Abramovici H., Rozmahel R. and Grant D. M., (2003) Generation and functional characterization of arylamine N-acetyltransferase Nat1/Nat2 double-knockout mice. Mol. Pharmacol. 64, 170-179.

34. Grunecker B., Kaltwasser S. F., Peterse Y., Samann P. G., Schmidt M. V., Wotjak C. T. and Czisch M., (2010) Fractionated manganese injections: effects on MRI contrast enhancement and physiological measures in C57BL/6 mice. NMR Biomed. 23, 913-921.

35. Sled J. G., Zijdenbos A. P. and Evans A. C., (1998) A nonparametric method for automatic correction of intensity nonuniformity in MRI data. IEEE Trans. Med. Imaging. 17, 87-97.

36. Uberti M. G., Boska M. D. and Liu Y., (2009) A semi-automatic image segmentation method for extraction of brain volume from in vivo mouse head magnetic resonance imaging using Constraint Level Sets. J. Neurosci. Methods. 179, 338-344.

37. Chuang K. H., Koretsky A. P. and Sotak C. H., (2009) Temporal changes in the T1 and T2 relaxation rates (DeltaR1 and DeltaR2) in the rat brain are consistent with the tissue-clearance rates of elemental manganese. Magn. Reson. Med. 61, 1528-1532.

38. Mitnick C., Bayona J., Palacios E., Shin S., Furin J., Alcantara F., Sanchez E., Sarria M., Becerra M., Fawzi M. C., Kapiga S., Neuberg D., Maguire J. H., Kim J. Y. and Farmer P., (2003) Community-based therapy for multidrug-resistant tuberculosis in Lima, Peru. N. Engl. J. Med. 348, 119-128.

CHAPTER – 6

Summary, Limitations, and Future Directions

Translational animal models of brain disorders remain essential for thorough understanding of the patho-biological mechanisms, as comprehensive research cannot be done in controlled and reproducible manner on humans. Research directed at morphological, pathophysiological mechanisms and functional activities of the CNS can be realized through imaging systems *in vivo*. A significant literature now demonstrates the importance and utility of MRI towards unraveling the complex neural system, healthy or diseased. MRI is a non-invasive and versatile imaging tool. It allows longitudinal, three-dimentional assessment of tissue anatomy, pathophysiology, function and metabolism. Due to these properties MRI has achieved widespread success in experimental neuroscience studies. Yet, there is a room for improvement in MRI specificity and sensitivity, and this can be achieved by using contrast agents, especially Mn^{2+}.

MEMRI opens the great opportunity to study complex paradigms in freely behaving animals. By taking the advantage of chemical and biological properties of Mn^{2+} in living organisms, MEMRI has been successfully applied in the studies of several neurological diseases using animal models, such as stroke, Parkinson's disease, Alzheimer's disease, epilepsy, and other brain disorders to assess detailed information about neuronal activity, morphology and neuronal tracts as well as rate of axonal transport. Mn^{2+} is toxic, however, MEMRI revels new patho-biological information that might be otherwise difficult to gain. Properly planned administration of Mn^{2+} and close monitoring of animals after administration is required to avoid toxicity and pain to animals. Although previous studies highlight the potential of MEMRI for brain imaging, the limitations still exist concerning the use of Mn^{2+} in living animals. The development

of MEMRI applications in neuroscience research are at the beginning level. Therefore, development of methods of MEMRI for experimental studies remains essential for diagnostic findings as well as development of therapeutic strategies.

In the first study (Chapter - 2), we investigated role of glia and neurons in MEMRI signal enhancement during inflammation. Unlike other contrast agents such as gadolinium, iron oxide, and iron platinum Mn^{2+} can provide unique intracellular insights about brain pathophysiology. Nonetheless, a critical question that remained poorly understood was the brain cells that serve as sources for the MEMRI signal enhancement during inflammation. In this study, we investigated MEMRI's abilities to detect glial (astrocyte and microglia) and neuronal activation signals following treatment with known inflammatory inducing agents. The idea was to distinguish between gliosis (glial activation) and neuronal injury for the MEMRI signal and as such use the agent as a marker for neural activity in inflammatory and degenerative disease. This work demonstrated that cytokine-induced glial activation facilitates neuronal uptake of Mn^{2+} *in vitro*. Glial Mn^{2+} content was not associated with glial activation. After *in vitro* conformation, we validated our hypothesis *in vivo*. MEMRI was performed on mice injected with lipopolysaccharide by IC route. MEMRI signal enhancement was associated with increased neuronal activity. In conclusion, results supported the notion that MEMRI reflects neuronal excitotoxicity and impairment that can occur through a range of insults that include neuroinflammation and MEMRI signal enhancement in the CNS is induced by astrocytic activation by stimulating neuronal Mn^{2+} uptake.

In the second study (Chapter - 3), we evaluated the efficacy of MEMRI in diagnosing the brain pathology in an animal model of neurodegenerative disease,

neuroAIDS. Progressive human immunodeficiency viral (HIV) infection commonly leads to a constellation of cognitive, motor and behavioral impairments. These are collectively termed HIV-associated neurocognitive disorders (HAND). While antiretroviral therapy (ART) reduces HAND severity, it does not affect disease prevalence. Despite decades of research there remain no biomarkers for HAND and all potential co-morbid conditions must first be excluded for a diagnosis to be made. To this end, we now report that MEMRI can reflect brain region specific HIV-1-induced neuropathology in chronically virus-infected NOD/scid-IL-2Rγc^{null} humanized mice. MEMRI diagnostics mirrors the abilities of Mn^{2+} to enter and accumulate in affected neurons during disease. T$_1$ relaxivity and its weighted signal intensity are proportional to Mn^{2+} activities in neurons. In 16-week virus-infected humanized mice, altered MEMRI signal enhancement was easily observed in affected brain regions. These included, but were not limited to, the hippocampus, amygdala, thalamus, globus pallidus, caudoputamen, substantia nigra and cerebellum. MEMRI signal was coordinated with levels of HIV-1 infection, neuroinflammation (astro- and micro- gliosis), and neuronal injury. MEMRI accurately demonstrates the complexities of HIV-1 associated neuropathology in rodents that reflects, in measure, the clinical manifestations of neuroAIDS as it is seen in a human host.

In the third study (Chapter − 4), our successful collaboration with Dr. Sajja BR (Associate Professor, Department of Radiology, UNMC, Omaha, NE) led to generation of a MEMRI-based NOD/scid-IL-2R$_{\gamma c}$^{null} (NSG) mouse brain atlas. Strain specific mouse brain MRI atlases provide coordinate space linked anatomical registration. This allows longitudinal quantitative analyses of neuroanatomical volumes and imaging metrics for

assessing the role played by aging and disease to the central nervous system. As NSG mice allow human cell transplantation to study human disease, these animals are used to assess brain morphology. MEMRI improves contrasts amongst brain components and as such can greatly help identifying a broad number of structures on MRI. To this end, NSG adult mouse brains were imaged *in vivo* on a 7.0 Tesla MR scanner at an isotropic resolution of 100 μm. A population averaged brain of 19 mice was generated using an iterative alignment algorithm. MEMRI provided sufficient contrast permitting 41 brain structures to be manually labeled. The developed atlas is made available to researchers through Neuroimaging Informatics Tools and Resources Clearinghouse (NITRC) website (https://www.nitrc.org/projects/memribrainatlas/).

In the fourth study (Chapter – 5), we evaluated the efficacy of N-acetylated-para-aminosalicylic acid (AcPAS) to accelerate Mn^{2+} elimination from rodent brain. The brain retention of Mn^{2+} is relatively long with a half-life ($t_{1/2}$) of 51 to 74 days causing a slow decline of MRI signal enhancement following Mn^{2+} administration. Such slow decline limits using repeated MEMRI to follow the central nervous system longitudinally in weeks or months. This is because residual Mn^{2+} from proceeding administrations can confound the interpretation of imaging results. To the best of our knowledge, no method exists to accelerate the decline of the Mn^{2+} induced MRI enhancement for repeated MEMRI tests. We investigated whether AcPAS, a chelator of Mn^{2+}, could affect the decline of Mn^{2+} induced MRI enhancement in brain thus enabling repeated MEMRI, and as a consequence broadens the utility of MEMRI tests. Two-week treatment with AcPAS (200 mg/kg/dose $\times$ 3 daily) accelerated the decline of Mn^{2+} induced enhancement in MRI. (In the whole brain on average the enhancement declined 83% in AcPAS treated

mice, while in PBS controls the decline was 73%. We posit that AcPAS could enhance MEMRI utility for evaluating brain biology in small animals. Further study needed for detailed understanding.

In general, major disadvantage of MEMRI is the toxicity associated with Mn^{2+}, which restricted its clinical transformation. As obtained MEMRI contrast is directly related to accumulation of Mn^{2+} in excitable cells in activity dependent manner, MEMRI has been successfully used to study neuronal activation. However, difference in Mn^{2+} influx and efflux rates (long half-life in brain) or long clearance time allowed to produce only static activation maps and do not allow to inform about temporal or rapid changes in neuronal activity (Silva et al. 2012). Also, it remains to be investigated whether MEMRI detects neuronal deactivation (Silva et al. 2012). We have demonstrated that MEMRI visualizes reactive astrogliosis (increase in signal intensity) and neuronal loss (decrease in signal intensity; ongoing study in the lab, data not shown in this thesis). But limitation is that one of the dominating cellular mechanisms offsets other mechanism to determine the MEMRI results. MEMRI is still not sensitive enough to detect gliosis and neuronal loss at the same time. Also, threshold level of cellular activity for generating MEMRI signal is not studied yet.

In all the studies of this thesis, we have measured and compared T_1 signal intensities on three-dimensional (3D) high-resolution ($<=$ 100 μm pixel size) T_1-wt images for healthy and diseased animals. T_1 values were also measured using multi-slice MRI with lower in-plane resolution. MRI scanner system variation was then estimated using the T_1 values and T_1-wt signal. The acquired T_1-wt images were then calibrated. Detailed process of the image calibration is described in chapter - 3 of this thesis. We are

now developing a fast T_1 mapping sequence to directly measure brain T_1 values by a 3D high-resolution fashion. This method will provide more accurate results on brain Mn^{2+} uptake and accumulation.

There are extensive possibilities for future applications of MEMRI in translational neuroscience research. The possibility of longitudinal studies enable the measurement of functional changes in CNS after pharmacological interventions as well as therapeutic treatment. Integration of MEMRI with multiple imaging modalities will overcome the limitations of previous single parametric approach and therefore, will establish a comprehensive study to understand neurobiological mechanisms underlying normal and abnormal functions.